The North Atlantic climatic events recorded in Cretaceous Naskapi Member cores, Scotian Basin

By

Isabel Chavez Gutierrez

A Thesis Submitted to

Saint Mary's University, Halifax Nova Scotia

In Partial Fulfillment of the Requirements for a

Bachelor of Science Honours Degree in Geology

May 2015, Halifax, Nova Scotia

Certification

I certify that this thesis was submitted by Isabel Chavez in fulfillment of the honours degree requirement for the Bachelor of Science Honours degree in Geology at Saint Mary's University, Halifax, Nova Scotia. This Thesis represents the original work carried out by Ms. Chavez under my supervision.

_____

Dr. Georgia Pe-Piper

Professor of Geology

The North Atlantic climatic events recorded in Naskapi Member cores, Scotian Basin

By Isabel Chavez Gutierrez

Abstract

The Cretaceous was a time when global temperatures and rainfall patterns were controlled by plate tectonic changes and intense volcanic activity. High temperatures, high weathering rates and unusual ocean circulation characterized this time period, resulting in preservation of organic carbon in sediment and the formation of black shale sequences. The Mid Cretaceous Aptian had two major positive carbon isotope excursions followed by negative carbon excursions that were recorded in marine and terrestrial organic matter. The changes from arid to humid conditions have been recognised in the Tethyan stratigraphy and similar facies elsewhere, including the Scotian Basin.

This study investigates the value added by portable X-Ray Fluorescence Spectroscopy (pXRF) and colour spectrophotometry analyses in interpreting paleoclimatic and paleoceanographic changes preserved in shales from the early Aptian Naskapi Member of the Scotian Basin. The relationship of element ratios K/Ti, Th/Ti, V/Ti, Mn/Ti, Zr/Ti, K/Th and total organic carbon (TOC) measured on both in-situ core and powdered samples from core, rubble and cuttings was plotted to indicate the input of weathered material, redox conditions, dilution of shale, aridity/humidity conditions and the amount of organic carbon preserved in the shales. Colour measurements were also plotted to determine variations controlling sedimentation and environmental change.

The analytical approach used identified environmental changes in shales from the Scotian Basin that have also been identified in the Tethyan Basin. The distribution of ammonites after flooding events in the Naskapi Member places the Selli Event in the Early Aptian, TOC concentration peaks correlate to episodes of humid conditions, high sea level events (facies 3) and the occurrence of other oceanic anoxic events as in western Europe.

The use of powdered sample for both the pXRF and colour spectrophotometry analyses seemed to be more reliable and show better representation of the environmental conditions compared to the in-situ core samples.

Acknowledgements

I would like to thank Dr. Georgia Pe-Piper for believing in me and offering me this project, which has been an amazing learning experience. Dr. Pe-Piper's constant guidance and support throughout this past year has been very helpful and essential for the completion of this project. She is an inspiration for women, a great role model, and an amazing and caring advisor.

Also, I would like to give thanks to Dr. David Piper for his time, patience, advice and feedback. I am very grateful to both of you, Dr. Pe-Piper and Dr. Piper, for your valuable teaching and guidance throughout this learning experience. Thanks to Dr. Andrew MacRae for his valuable knowledge, advice and feedback for the project.

I would like to thank the amazing ladies from the Bedford Institute of Oceanography, Lori Campbell and Jenna Higgins. They welcomed me into their labs and provided me with valuable help and guidance to prepare and analyze the samples.

Thanks to the Canada-Nova Scotia Offshore Petroleum Board and Ms. Nancy White for allowing and helping with the sampling of the core, rubble and cuttings needed for this project.

I would like to thank Dr. Yuanyuan Zhang. She has always helped me with endless questions about geology, computers' and life.

Last but not least, I would like to thank my family, whom without I would not had the opportunity to study in Canada. Their constant and loving support has always helped me and cheered me up through the hardest and best times.

Table of Contents

List of Figures

List of Tables

Appendices

List of abbreviations

CIE – Commission de I' Eclairage

CORBs- Cretaceous oceanic red beds

EEC – Episodes of environmental change

ICPMS- Inductively coupled plasma mass spectrometry

LOM – Laminated organic-rich muds

MFS- Maximum flooding surface

OAE – Oceanic anoxic event

OETRA – Offshore Energy Technical Research Association

PFA – Play Fairway Analysis

pXRF- portable X-ray fluorescence spectrometer

TOC- Total organic carbon

Chapter 1: Introduction

In the Early Cretaceous, climatic fluctuations were experienced and induced by the rifting of the supercontinent Pangaea. This is a period in Earth history when abundant rift basins formed, ocean floor spreading and marine and terrestrial volcanic activity increased (Föllmi, 2012). The fluctuations between arid and humid conditions allowed the preservation of laminated organic-rich muds (LOM), interpreted as episodes of environmental change (EEC) in Tethys and its continuation in the central North Atlantic Ocean. The Selli Episode was a short, warm, humid climatic phase that developed in the early Aptian and affected biogeochemical-weathering rates, oceanic circulation, and carbon cycling, resulting in the deposition of carbon-rich mud.

In western Europe, there is evidence of arid conditions in the Tithonian-Berriasian (Allen, 1998; Nunn & Price, 2010) and in the Barremian (Ruffell et al., 2002; Föllmi, 2012), and evidence of humid conditions dominating in the Aptian (Ruffell and Worden, 2000). Ruffell and Batten (1990) suggested, in a study of clays mineral and palynomorphs, that the Barremian was a predominantly arid period while the Aptian was humid. Weissert (1989) suggested that humid conditions with a positive $\delta^{13}C$ excursion occurred in the Aptian due to increased sea-level, weathering and volcanism. The Scotian Basin, which is the equivalent in paleolatitude and paleolongitude of the Western European Basin in the Early Cretaceous, seems to show similar paleoclimatic events such as the Selli Event in the Aptian Naskapi Member (MacRae, 2011; Gould et al., 2014).

The Early Cretaceous climatic variations in the Scotian Basin has been previously studied by Gould et al. (2014) and Zhang et al. (2014) using spectral gamma log data and bulk-sediment geochemical data, respectively from offshore wells. In this study, a new

approach to determining the paleoclimate conditions in the Scotian Basin and the Naskapi Member is used, by studying the variations in geochemistry of shales at high resolution. The approach used is based on a combination of X-Ray Fluorescence (XRF), spectrophotometric and organic carbon data from conventional core and cuttings samples from different wells (Panuke B-90, Cohasset A-52, Hesper I-52, North Banquereau I-13 and Sable Island C-67) in the basin. In situ XRF is used to measure elements of interest such as K, Th, Zr, Ti, Fe, Mn that may be related to the rate of weathering, reducing conditions, organic matter and the significance of paleoproductivity. The spectrophotometer is used to measure the sediment colour on core and core powder samples to reflect the chemical composition of sediments and determine a proxy for carbonate, hematite and organic carbon using specific frequencies and reflectivities. Colour variations may indicate the external factors that control sedimentation and monitor global change (Nederbragt et al., 2000). Organic carbon data is used to determine the variation of oceanic conditions in the unit.

The Panuke B-90 well is an important contribution to this study because the Lower Aptian section has been continuously cored. This section can be thus thoroughly studied using bulk geochemistry, colour, and core spectral gamma in order to recognise changes in paleoclimate and paleoenvironment in a concise time scale and to compare with literature from equivalent outcrops on land in western Europe.

The objectives of this study are to: (i) correlate and identify the Mid Cretaceous Atlantic Ocean climatic events in the Aptian Naskapi Member, focusing on the Selli Event, and establish the conditions in which the shales of this member were deposited; and (ii) evaluate the limitation and significance of proposed analytical methods along

with previous spectral gamma and Inductively coupled plasma mass spectrometry (ICMPS) bulk geochemical data of samples from some of the wells being studied.

Chapter 2: Geological Setting

The Scotian Basin formed during the breakup of Pangaea and the opening of the North Atlantic Ocean. It is a Mesozoic-Cenozoic passive-margin basin on the Atlantic margin of south-eastern Canada (Fig. 1A). The basin received abundant sand supply in the Late Jurassic and Early Cretaceous, following the Late Triassic- Early Jurassic rifting, as a result of sediment supply from the rising Labrador rift shoulder. The resulting deltaic deposits comprise the Mississauga and Logan Canyon Formations, which are composed of sandy, deltaic, fluvial, and nearshore sandstones, with the shaly Naskapi Member at the base of the Logan Canyon Formation (Wade & MacLean, 1990; Fig. 1B).

The Naskapi Member is a transgressive thick shale unit of low sedimentation rate of the Logan Canyon Formation. It is between massive sandstone sequences of the Missisauga Formation and the interbedded sandstone and shale sequences of the Cree Member of the Logan Canyon Formation. It consists of shales of varied colours, including brown, brownish-grey, or green grey shale, and near the base is commonly reddish brown to pale red (Purcell et al., 1979). This member is commonly interbedded with silty and sandy zones and becomes increasingly sandy along the northern edge of the Abenaki Subbasin (Wade and MacLean, 1990).

The depositional environment of the Naskapi Member has been interpreted from macrofossils to be tidal flat to fully marine. The member represents a transgressive episode overlying a delta plain environment of the upper member of the Missisauga Formation. The base of the Naskapi Member shows a major lithological change from sandstone to shale (Wade and MacLean, 1990).

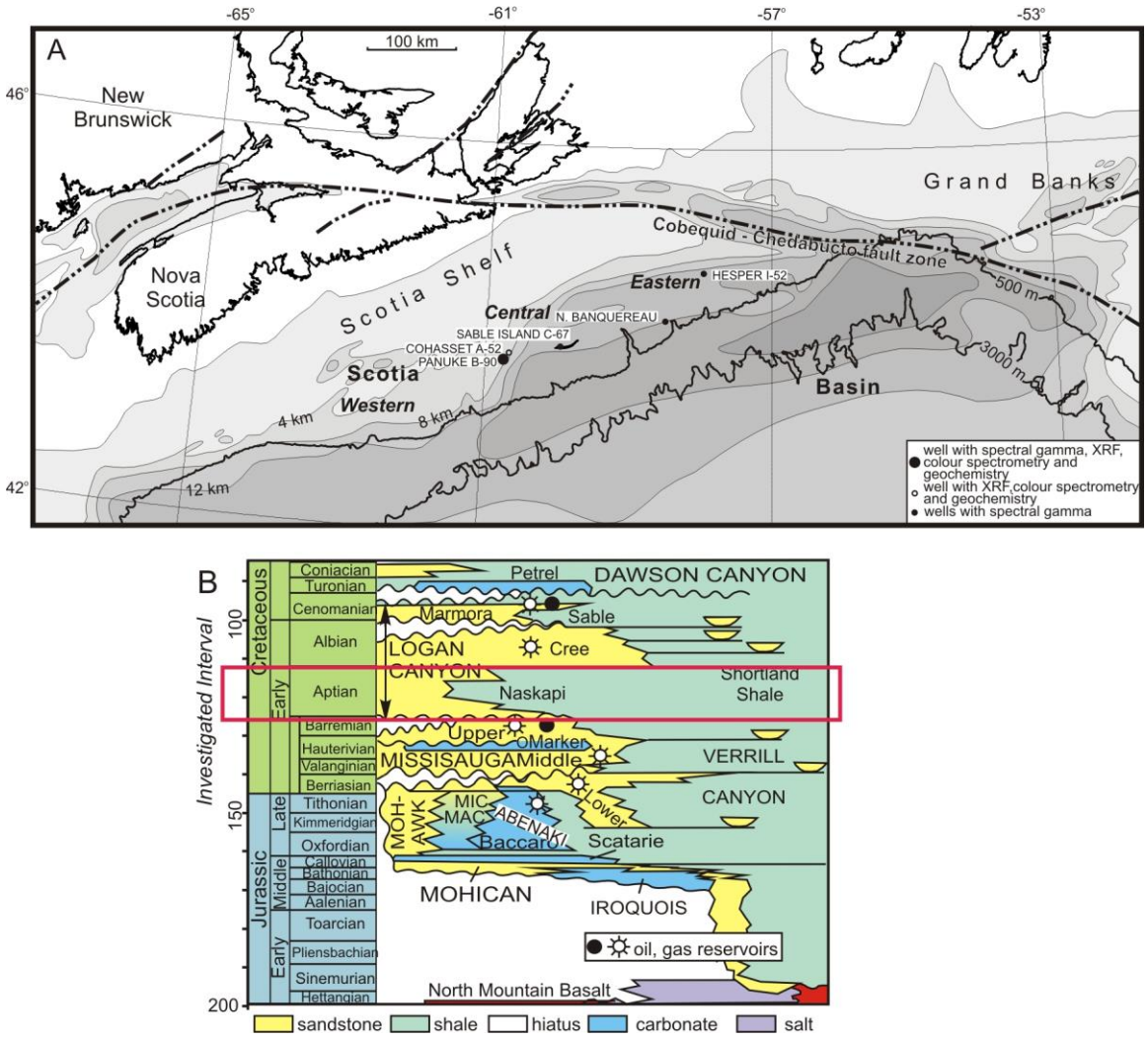

Figure 1: (A) Detailed isopach map of the Scotian Basin showing location of wells examined in this study (modified from Wade and MacLean, 1990). (B) Lower Jurassic-Upper Cretaceous stratigraphic summary of the Scotian Basin (modified from Weston et al., 2012). Red box highlights the stratigraphic interval in this study.

There are basalt flows and volcanoclastic rocks interbedded with the sediments of the Naskapi Member in several wells, which are interpreted to have originated at tensional fractures along the south flank of the Orpheus Graben (Bowman et al., 2012). Salt tectonics and faulting have subsequently interrupted the flows. The volcanic activity of the Scotian Shelf is thought to be related to a widespread period of midplate volcanism

in the western North Atlantic Ocean during the Early Cretaceous (Jansa and Pe-Piper, 1985).

In the Early Cretaceous, the drainage basin that was supplying the Scotian Basin was at the same paleolatitude as western European British Isles, Germany, and southern Sweden, because western Europe and Atlantic Canada had not yet fully separated (Ruffell & Batten, 2000; Ruffell & Worden, 2000).

The Naskapi Member resulted from the uplift of the Meguma Terrane and the extrusion of basalts in the Aptian which blocked the Labrador River that was supplying sediment to the basin through Cabot Strait, diverting it south-westwards to the Bay of Fundy (Piper et al., 2011).

The contact between the Upper Missisauga Formation and the Naskapi Member in Panuke B-90 starts with a fine-grained, low angle-inclined cross-stratified sandstone unit (classified as lithofacies 9s) that has an erosion surface with oysters at the top, followed by greenish-grey shales (lithofacies 2b) with abundant macrofauna including ammonites (*Deshayesites spp.*) (MacRae, 2011). Gould et al. (2012) have classified and interpreted the depositional environment of the top Missisauga Formation and Logan Canyon Formation in several wells, including Panuke B-90 well. The base of the cored interval through top Missisauga Formation and base Naskapi Member represent muddy shoreface deposits (lithofacies 2b).These deposits are overlain by transgressive shelf deposits (lithofacies 3x).

Chapter 3: Literature Review

The accelerated fragmentation of Pangaea in the Late Jurassic and Early Cretaceous (Le Pichon and Huchon, 1984) was accompanied by widespread volcanic activity and the formation of Large Igneous Provinces (Coffin and Eldholm, 1994), causing a major impact on the climate and turning the Cretaceous into a greenhouse period (Chamberlin and Salisbury, 1906). The boost in volcanic activity increased the volumes of mid-oceanic ridges (Pitman, 1978), global carbon dioxide levels (Berner, 1991) and global sea level (Haq et al., 1987). Consequently, the mega monsoonal Pangaean climate was modified and zonal climate along the opening of the Atlantic-Tethys seaway was established (Parrish, 1993). These effects resulted in high temperatures, high weathering rates and peculiar ocean circulation.

The paleoclimate of northwestern Europe was affected by the opening of the Atlantic in the Cretaceous, which resulted in the increasing of the Atlantic circulation to the north and west and decreasing the Tethyan circulation in the south (Ruffell et al., 2002). The high latitudes were probably ice-free, the latitudinal temperature contrast was weak (Barron and Peterson, 1990) and the ocean circulation was very different because ocean basins were elongated in east-west rather than the present north-south orientation.

The episodes of intensified greenhouse climate conditions led to an increase in weathering, erosion, runoff rates and elevated nutrient levels from continents into oceans, resulting in the decrease of carbonate nannofossils, the increase of phytoplankton production and black shale deposition (Weissert and Erba, 2004).

Higher fertility and organic carbon preservation in sediment resulted from the intensified nutrient delivery from weathering (Weissert, 2000), from sea-level changes, from advection of anoxic water masses from marginal sea far out into open ocean (Hallam and Bradshaw, 1979; Jenkyns, 1980) and from extensive volcanic activity along the North American margin during the Aptian (Jansa and Pe-Piper, 1985; Piper et al., 2007). The sequences of black shales formed due to oceanographic changes that were controlled by the plate tectonics and rising sea-level (Weissert, 1981; Jenkyns, 1980). Consequently, these sequences recorded global changes in carbon cycles and climate during the Oceanic Anoxic Event (OAE) in the Early Cretaceous.

The fluctuations in organic and inorganic carbon fluxes during the Early Cretaceous coincide with the black shales of OAEs. The observed warming trend precedes the negative carbon isotope excursion, indicating changes in ocean chemistry, and carbonate production. The following positive carbon isotope excursions in carbonate minerals of limestone and marls postdate the onset of the biocalcification and platform crisis and coincided with black shales of OAEs. There are two positive carbon isotope excursion characteristic of the Aptian, which lasted several million years with high amplitude (>4‰). These excursions have been identified in section from the Tethyan basin, North Atlantic and Pacific oceans (Lini, 1994, Erbacher, 1994, Weissert and Breheret, 1991; Föllmi et al., 1994, Weissert and Lini, 1991; Jenkyns, 1995).

The positive carbon isotope excursions were followed by short-term negative isotope excursions. These negative anomalies are considered additions of ^{12}C from the geosphere into the atmosphere and ocean systems due to the rapid release of methane

during times of warming climate (Gröcke et al., 1999) or volcanic activity (Jenkyns, 2003; Svensen et al., 2004).

The long-term semi-arid to semi-humid climate change in the early Aptian was synchronous with the rise in eustatic sea-level and global warming (Weissert, 1989). Both effects are reflected in the northern Tethyan stratigraphy and similar facies elsewhere. Vahrenkamp (1996) recorded similarities between the clastic rocks of the Aptian and Valanginian and some successions in the Middle East, indicating a global extent for these fluctuations. Gröcke (1977) indicated that the change from arid to humid conditions in the Barremian- Early Aptian could be recognised as far away as Australia. Aptian climates were predominantly arid in the Tethys and southern North Atlantic, where limestones and evaporites predominate, while humid episodes in the Tethys and the South Atlantic are represented by mudstone deposition.

In the Late Cretaceous, in contrast, Cretaceous Oceanic Red Beds (CORBs) are common (Wang et al., 2011). Even though the CORBs dominated in the Late Cretaceous, they became increasingly widespread from the Aptian through the Campanian. They were deposited in the middle to low latitude basins of the Tethys, Atlantic, Indian and Pacific Oceans on outer-shelf, continental slope and deep sea environments (Wang et al., 2011). The decrease in seafloor volcanic activity and burial of large amount of organic carbon during the Early and Mid-Cretaceous (Berner, 2003) decreased the carbon dioxide levels in the atmosphere (Clarke and Jenkyns, 1999) cooling thus the global temperatures. Global cooling increased the equator-to-pole temperature gradient, favoring the rates of oceanic turnover leading to a well-ventilated deep ocean, mainly along the Antarctic margin (Otto-Bliesner et al., 2002). When the connection between North and South

Atlantic oceans opened in the Campanian, the deep ocean water circulation improved, allowing deep waters generated in the southern hemisphere to circulate throughout the Atlantic basin (Poulsen et al., 2001). The cooler high latitude deep water introduced more oxygen to the deep ocean, oxidizing more organic matter and iron oxides formed at the sediment-seawater interface. At the same time, the continental input of phosphorus to the ocean decreased due to cooler climate (Föllmi, 1996). The decrease of phosphorus cycling from land to ocean lowered the productivity in the ocean (Tyrrell, 1999).

Chapter 4: Methods

4.1: Sample preparation

Samples of shales from the Early Cretaceous Upper Mississauga-Logan Canyon Formations mostly from conventional core were analysed, including samples from cuttings to fill in the gaps in order to cover the upper part of the Naskapi Member, where conventional core is not available. The Canada-Nova Scotia Offshore Petroleum Board made these samples available for the study. The samples cover the lower Naskapi Member in Panuke B-90, and the topmost Mississauga Formation and basal Cree Formation in Panuke B-90 and Cohasset A-52.

The wells Hesper I-52, Sable Island C-67 and North Banquereau I-13, which are located in the central and eastern Scotian Basin east and southeast of Panuke B-90, all have short intervals of conventional core (Gould et al., 2014). The Naskapi Member was correlated by gamma ray logs between these wells, and the presence of red, black and dark colours (dark grey, dark brown and dark grey-brown) in shale cuttings within this member (Fig. 2) as was recorded from offshore well history reports from Hesper I-52 (1976), North Banquereau I-13 (1983), Panuke B-90 (1988) and Sable Island C-67 (1968).

For this study, chemical analyses from a portable X-ray fluorescence (pXRF) spectrometer and colour from a spectrophotometer were taken both directly on the core and on pulverized samples of rubble spalled off solid core from similar and other depths. The analyses performed directly on the core did not require any preparation. The samples from core and cuttings were washed with distilled water and left to be dried.

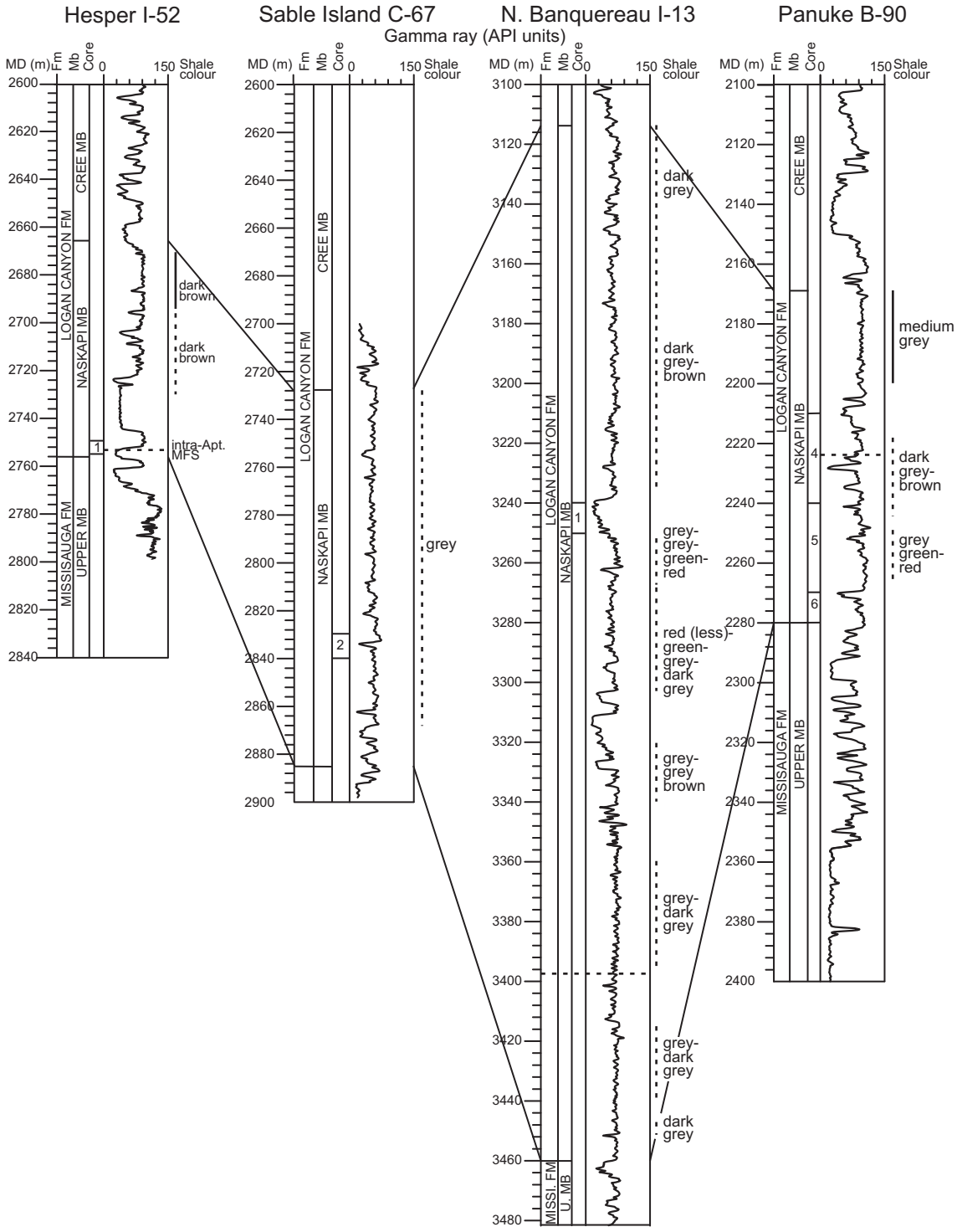

Figure 2: Regional gamma log correlation between wells near Panuke B-90 for the Naskapi Member. The distribution of shales in the Naskapi Member is marked with solid (pure shale) and dashed (interbedded shale, siltstone, sandstone and limestone) line with color description aside, based on lithologic descriptions from well history reports. No information about Aptian MFS for Sable Island C-67 well.

The core samples, in total 79, were later pulverized using a shatterbox with an iron bowl. The cutting samples, in total 27, were separated from grains that were not shales by hand under a binocular microscope and gently crushed with a spatula to form a homogenous powder.

Overall, we have four types of samples with corresponding analyses in this study:

(A) Powdered samples from core that were analyzed by ICPMS, pXRF and spectrophotometer
(B) Powdered samples from core that were analyzed by pXRF and spectrophotometer
(C) Core samples that were analyzed by in situ pXRF and spectrophotometer
(D) Powdered samples from cuttings that were analyzed by pXRF and spectrophotometer

4.2: In situ X-ray fluorescence (XRF) spectrometer

4.2.1: Principle

In situ XRF is a non-destructive method of chemical analysis in which high energy X-ray photons are emitted and strike the sample. In the atoms of the elements that make up the sample, these photons knock electrons out of their innermost orbitals and are replaced by electrons from outer orbitals creating a more stable electronic configuration. When an electron from the high energy outer orbital moves into the lower energy inner orbital, a secondary X-ray photon is emitted due to the decreased binding energy of inner electron orbitals compared to the outer ones. The emitted radiation is characteristic of a specific element and it is termed fluorescent radiation (Geotek Multi Sensor Core Logger Manual, version 17-02-14).

4.2.2: Settings of the spectrometer

The Innov-X Systems Delta Premium XRF spectrometer was used to measure selected elements of redox and paleoproductivity significance. This instrument possesses two different modes: Soil Mode and Mining Plus Mode and within each mode, there are different beams of different energies that target different elements. For this study, Soil Mode was selected, which offers speed, easy use, and generally good accuracy for concentration ranging from a few parts per million (ppm) levels up to 2-3 wt% concentrations. Elements are calibrated individually by the device itself and the spectra are normalized to the Compton scattering peak to account for the loss of photons in the matrix. This mode has 3 different beams of different energies that are used to target different elements.

In this study, Beam 2 (40kV with filter) and Beam 3 (15kV) were determined to be the best option. Beam 1 (40kV) was tested and found to give higher values for Th compared to ICPMS analyses; whereas, Beam 2 was also tested and gave better Th values than Beam 1, but still higher than the ICPMS analyses. The detection limit of U is 5 ppm, and P is 1 wt%: neither element was present in the studied samples at abundances above the detection limit. The absolute values depend on many variables including the nature of the bulk rock, the smoothness and thickness of its surfaces. Biplots comparing the ICPMS and pXRF analyses were used as a graphical representation of compatibility. More details for the settings of this instrument are given in Table 1. The same settings were used for all samples in this study.

Table 1: Summary of settings used with both the XRF spectrometer and spectrophotometer during this study.

Setting	pXRF spectrometer	Spectrophotometer
1. Mode	Soil- Beam 2 Soil- Beam 3	L*a*b* mode Spectro mode
2. Aperture	30 mm^2	3 mm
3. Voltage (kV)	Beam 2: 40 kV Beam 3: 15 kV	0.005 kV
4. Current (µA)	Beam 2: 0.1 µA Beam 3: 0.3 µA	2800000 µA
5. Acquisition time	Each beam = 30 seconds Total = 60 seconds	~5 seconds
6. Illuminant	D65	D65
7. Calibration	Calibration is done at the factory. Analyzer measures a 316 Stainless Steel Alloy 'coupon' and compares it to expected values	zero and white

Sample types A, B and D were placed in small plastic square-shaped containers, compacted to create a flat surface and covered with a Spectro-film Ultra-thin Polyester film for X-ray (0.000015") before being analyzed. The Mylar thin films were chosen in this study because the films would not affect the photon transmittance of the elements of interest. However, if lighter elements (atomic number less than 20) are to be studied in the future, thinner films should be employed.

Sample type C was analysed directly on the core surface without using any film. The standards for the areas analysed include smoothness and thickness of the surface, and nature of the rock. Areas of sandstone, limestone, staining or fractures were avoided for better results.

4.2.3: Error measurement

The standard deviation of every element abundance was determined by the XRF instrument. The instrument counts X-ray photons hitting the detector, but there is always

an associated uncertainty in the measurement that comes from statistical noise. The instrument thus reports the 1-sigma uncertainty (or standard deviation) associated with the readings (Tables A1, A2).

4.3: Spectrophotometer

4.3.1: Background

Colour is a visually perceived property derived from the spectrum of light interacting in the eye with the spectral sensitivities of the light receptors. The colour of an object depends on the physics of the object in its environment and the characteristics of the perceiving eye and brain. Some objects reflect light, whereas others transmit light or emit light themselves contributing to the colour. Quantifying the colour of objects can be difficult. Therefore, quantitative expressions have been devised. The Commission Internationale de I'Eclairage (CIE, an international organization concerned with light and colour) developed such a method. These values are measured with a spectrophotometer, which measures color by gathering and filtering different wavelengths of reflected light from the samples,and measuring their relative intensities. Colours are reported as spectral data in 10 nm increments from 360 nm to 740 nm. The spectral data can be expressed in the CIE L*a*b* color system in which three components were measured. The lightness (L*) determines the value for a position in a white to black plane, and the chroma (a*) and (b*) determine the values for the position in a red to green plane and in a yellow to blue plane, respectively (Geotek Multi Sensor Core Logger Manual, version 17-02-14).

4.3.2: Settings of the spectrophotometer

The studied cores were analysed directly on their surface; whereas core rubble and cuttings were analysed on their powders. The spectrophotometric analyses were made at

the Canada Nova Scotia Offshore Petroleum Board and at the Bedford Institute of Oceanography in Dartmouth, Nova Scotia, using the Konica Minolta Spectrophotometer CM-2600. The colour measurements were mainly taken on shales with the purpose to quantitatively determine the variation in colour among the samples as a proxy for carbonate, hematite and organic carbon. Before starting, a zero calibration without anything in the path of the instrument's light, and a white calibration using the provided white calibration plate were made. The settings used to analyze all the samples are summarized in the Table 1. For sample type C, samples were measured directly on the core without using any film. Smooth areas without inclusions, fractures, cracks, dust and staining were analyzed to avoid any effect they may have on the collected data. These limitations are not present for sample types A, B and D made of powders.

Type A, B and D samples were placed in plastic vials of different sizes depending on the quantity available of the sample powder. For each different size of plastic vial a mould of the cap with a hole was produced. When analyzing the samples, a piece of Glad plastic wrap was placed on the vial and kept in place with the mould. The procedure was repeated for all the samples.

4.4: Organic carbon measurements

4.4.1: Principle

A CHN analyzer is used to determine carbon, nitrogen and hydrogen content of samples. The analysis cycle of the instrument consists of three phases: purge, burn and analyze. During the purge phase, the encapsulated sample in the loading head is sealed and purged of any atmospheric gases. During the burn phase, one sample at a time is dropped into the primary furnace at 950°C and flushed with pure oxygen for very rapid

combustion. The products of combustion are passed through the after-burner furnace, furnace filter, pre-cooler, and thermoelectric cooler before collected in the ballast volume. During the analysis, the combustion gases in the ballast become homogeneous by passive mixing. Then infrared detectors measure the evolved gases for carbon and hydrogen. The values are displayed as weight percent after four minutes (Truspec Micro Elemental Series Manual).

4.4.2: Analytical Procedure

Organic carbon measurements were taken on powdered samples from core rubble and cuttings on the Leco Truspec CHN analyzer at the Bedford Institute of Oceanography in Dartmouth, Nova Scotia. The samples underwent several steps before being analyzed, which consisted of weighing the sample and placing it in labeled plastic tubes; acid digestion; rinsing; decanting; drying; crushing; and analyzing. To calculate only total organic carbon, acid digestion was used in order to remove inorganic carbon in the sample. For acid digestion around 10-15 mL of 10% concentration of HCl was added to each tube, and these tubes were then agitated in a vortex for 7 to 10 seconds. The samples were left to sit for 30 to 40 minutes before rinsing. For rinsing, the liquid was decanted and 10-15 mL distilled water was added. The tubes were agitated in the vortex, then filled completely with more distilled water and let them sit for two more rinses. After the last rinse, the tubes were decanted and set aside to dry. Once the samples were dry, they were crushed inside the tubes and put in the oven along with some standards to remove any moisture. To cool down, the samples were placed in a desiccator. 100 mg of the crushed samples and standards was weighed, encapsulated in small foil papers and placed in the

loading head of the instrument. Before any analysis, ten blanks were measured without samples in the instrument's loading head.

4.5: Lithofacies

The lithofacies scheme used in the study corresponds to modification by Gould et al. (2012) for the Missisauga and Logan Canyon formations in Panuke B-90 well. The lithofacies classification is based on environmental interpretation and are subdivided into subfacies to differentiate different rocks from the same depositional environment (Gould et al., 2011). Table 2 summarizes the lithofacies present in the cores studied from Panuke B-90 well, indicating a transition from fluvial to marine environments through the top of Missisauga Formation into the Logan Canyon Formation.

Table 2: Summary of sediment facies description found in cores 4-6 from Panuke B-90 well (modified by Gould et al., 2012) used in the detailed conventional down core plot of the Naskapi Member in Figures 3, 4 and 7.

Lithofacies	Subfacies	Lithology
0	0b	fine sst, slst, mst (sandstone > mudstone)
	0m	mst, siltstone, vf sst (mudstone >> sandstone)
1	-	Mst, <5% fine sst or slst
2	2b	Must, fine sst (10% -60%)
	2c	Fine sst (60% - 95%), mst
3	3i	intraclast cgl; common brown staining due to early siderite
	3l	bioclastic limestone
	3y	muddy sst (50% - 90% sand), granules; poorly sorted; common brown staining due to early siderite
	3x	sandy mst (10% - 50% sand); granules; poorly sorted; common brown staining due to early siderite
4	4g	medium to coarse sst; may have coarse-grained lag at base of unit; <5% mst
	4o	principally fine sst
9	9s	fine sst, minor mst, minor interbedded facies 0

Note: cgl, conglomerate; mst, mudstone; slst, siltstone; sst, sandstone; vf, very fine.

4.5: Visual colour nomenclature

The visual colour for the powdered samples were determined wit the naked eye, but were later correlated with an approximate range in L*a*b*. Table 3 shows the range in L*a*b* for each of the nine observed visual colour, the location of the wells the colours were found in and the number of samples with the observed colour.

Table 3: L*a*b* range for different visual colours for powdered samples from Panuke B-90 and Cohasset A-52 wells.

Visual Colour (naked eye)	**Samples #**	**Location of sample (well)**	**Spectrophotometry**					
			L*(D65)		**a*(D65)**		**b*(D65)**	
			low	**high**	**low**	**high**	**low**	**high**
brown	16	B-90, A-52	36.0	51.4	0.7	2.5	5.5	10.1
dark brown	1	B-90, A-52	52.2		0.7		6.5	
green	1	A-52	70.4		-3.1		8.3	
grey	23	B-90, A-52	58.2	66.1	-1.1	0.8	5.4	7.7
greyish brown	42	B-90, A-52	44.2	60.0	0.3	2.3	5.5	10.7
light brown	8	B-90	49.1	59.1	0.6	2.1	6.5	11.1
light grey	19	B-90, A-52	60.4	66.1	-0.8	-0.2	6.0	8.1
light greyish brown	16	B-90	50.9	63.0	-0.2	1.2	6.1	10.8
red	1	A-52	52.9		7.3		13.7	
Note: B-90= Panuke B-90; A-52= Cohasset A-52								

Chapter 5: Results

5.1: Variation in paleoenvironment proxies (element ratios)

The first step was to check the quality of our analytical data. Biplots were used, showing possible correlation of elements of interest (Fe, Mn, Ca, K, Th, Cr, Ti, S, V, Rb, Sr and Zr) between the chemical analyses of powdered samples from core (type A) and powdered samples from core and cuttings (types B and D) (more details about geochemical variation on samples analyzed by ICPMS are presented in Gould et al., 2012). Elements of interest showed good correlation between most elements of both types of powdered samples from core (types A and B; Fig. A1), with the exception of the elements Cr, V and Th that show a lower R^2 compared to the other element biplots (Table 4).

Table 4: Summary of correlation coefficient (R^2) of representative elements from pXRF and ICPMS analysis biplots, respectively for both powdered and in-situ core samples. See dataset in Tables A1 and A2.

Element		Ca	Cr	Fe	K	Mn	Rb	S	Sr	Th	Ti	V	Zr
R^2	**Powdered sample**	1.00	0.79	0.91	0.92	0.98	0.99	0.95	1.00	0.35	0.92	0.80	0.92
	In-situ core sample	1.00	0.49	0.96	0.97	0.96	0.97	0.40	0.84	0.55	0.85	0.28	0.74

There is also a good correlation between the powdered core samples (type A) and in-situ core samples (type C) geochemical data, but in these biplots, elements V, Cr, Th, S and Zr show a lower R^2 than the rest (Table 4, Fig. A2). The in-situ core samples (type C) seem to have more elements farther from the fitted regression line (lower R^2) compared to the powdered samples from core (type B) biplots, which could be due to inclusions,

microfractures, fractures, and other surface disturbances that are not present in the homogenous powdered samples (Fig. A2).

The whole rock chemical analyses of all sample types (A, B, C and D), were plotted against the stratigraphic column of the Naskapi Member of the Panuke B-90 well to see changes at different depths, facies and lithology (Fig. 3). The core plots cover 75 m in intervals of 20 m. The plots for the elemental ratios from in-situ core (type C) and powdered samples (types A, B and D) seem to correlate most wells (Figs. 3 and 4), with the exception of some cutting samples (type D) that lie as outliers. Type D samples are an average of over 5 m and do not derive from a specific depth as core powdered samples (types A and B). Furthermore, the potential of contamination is higher in cuttings powdered samples than in the other samples.

The K/Ti ratio starts with low values near the top of the section (interval 2215-2235 m; Figs. 3 and 4), then increases at 2240 m and drops again below 2279 m near the base of the Naskapi Member. The Mn/Ti ratio follows the same trend as it also starts with low values, then reaches its highest peak at 2254 to 2264 m and decreases at 2267 m until the base of the core. V/Ti ratio shows that the in-situ core samples (type C) and the powdered core samples (types A, B and D) are not matching as the other ratios are. The highest values for V/Ti ratio for the powdered samples (types A, B and D) are at 2245 to 2252 m below which the values seem to lower and rise slowly again at 2262 to 2265 m. The in-situ core samples (type C) show a high peak in the V/Ti ratio at 2233, 2241-2243 and 2262-2266 m. Continue (p. 32)

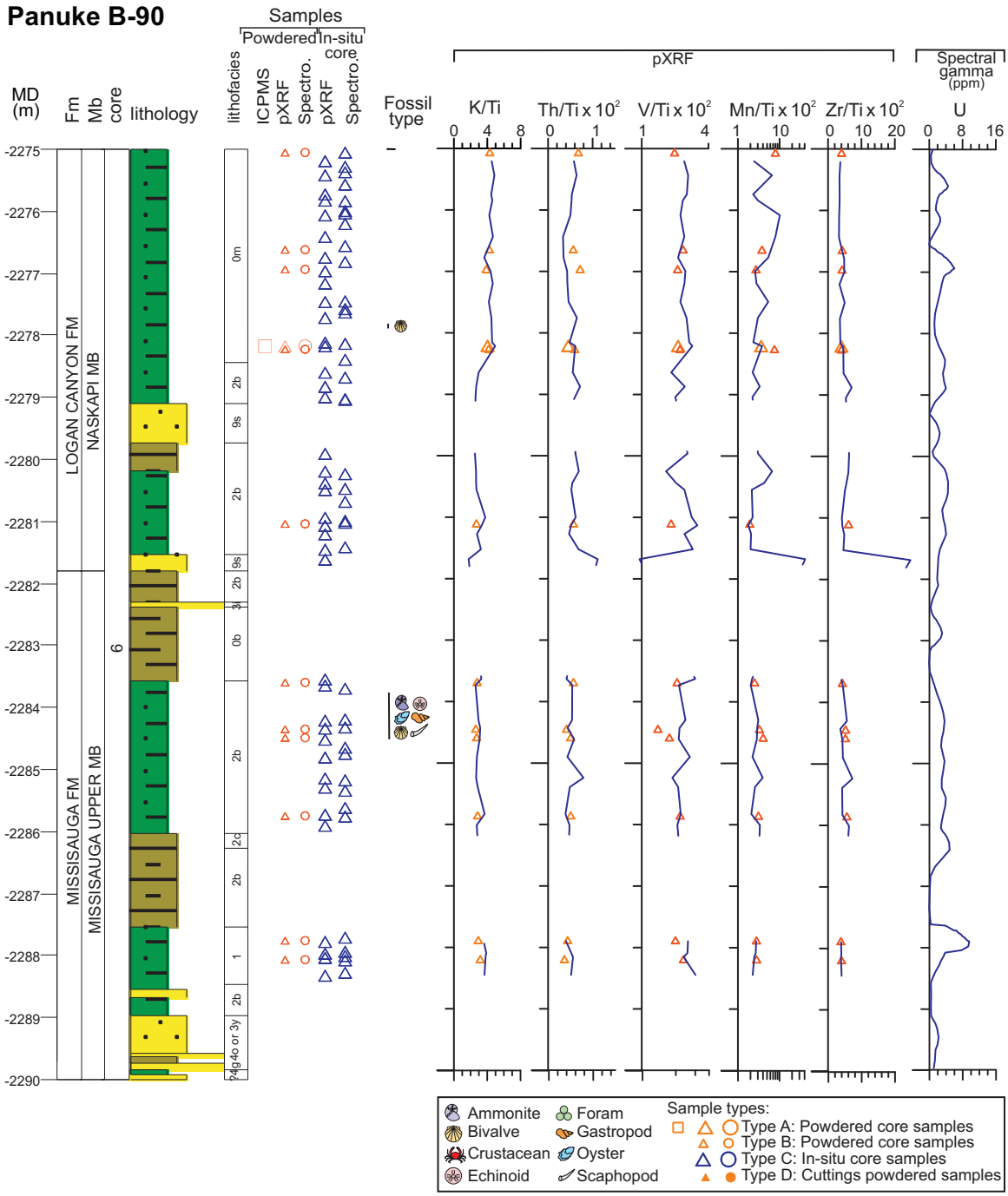

Figure 3: Conventional core with pXRF, colour, TOC and spectral gamma data, showing relationships between element ratios and colours. Line plots of K/Ti, Th/Ti, V/Ti, Mn/Ti ratios from pXRF and spectrophotometer analyses taken directly on core; scatter plots of these ratios from pXRF, spectrophotometer and TOC analyses taken on powdered samples. The powdered samples are composed of core, rubble and cuttings. ICPMS samples were cut from precisely located pieces of core (for more details see Zhang et al., 2014). Lithofacies (Gould et al., 2012). Sample position for this study are marked. The ratios for V/Ti, Mn/Ti and K/Th have a log scale. L* parameter dashed-line represents in-situ core samples and solid- line represents powdered samples.

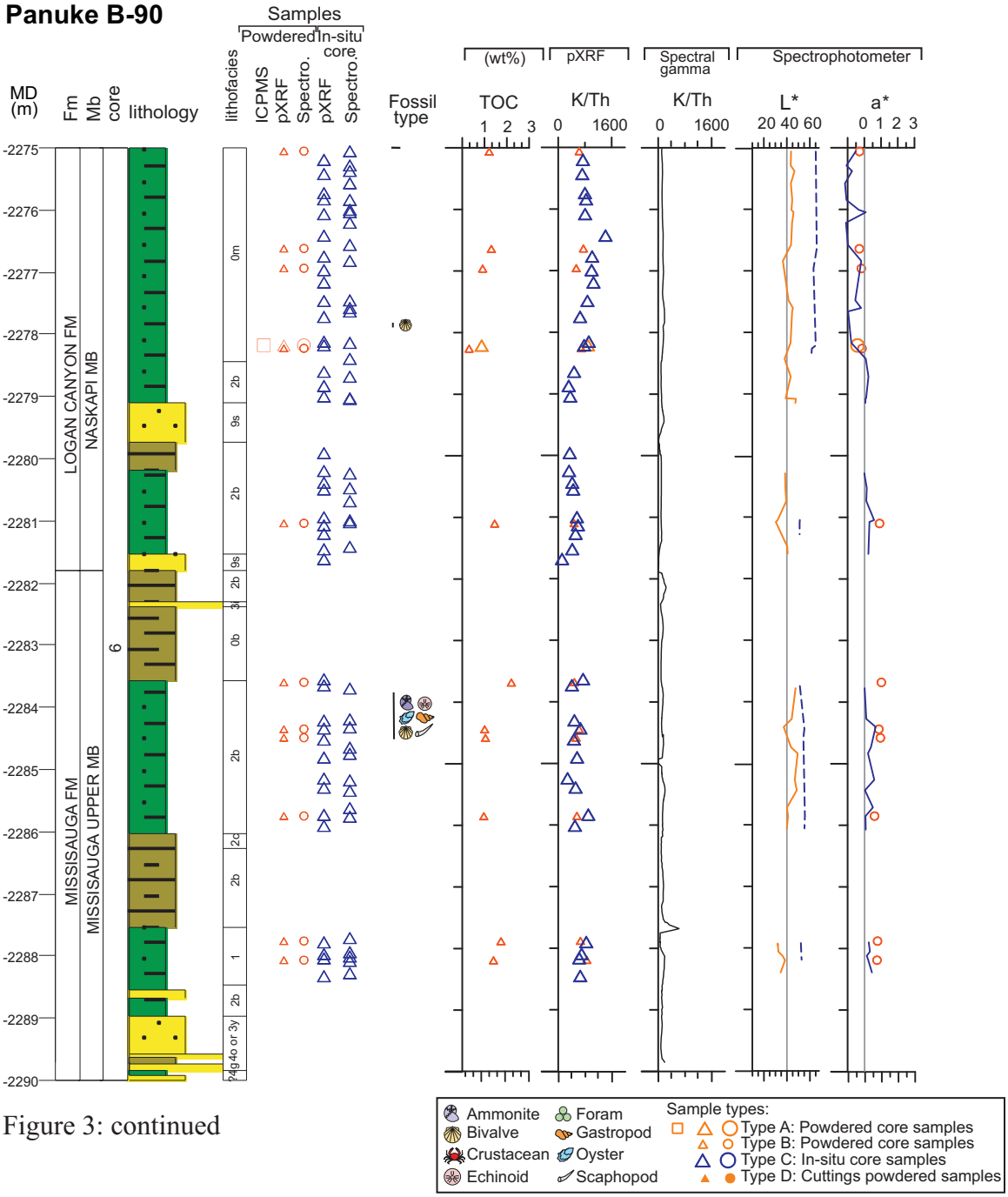

Figure 3: continued

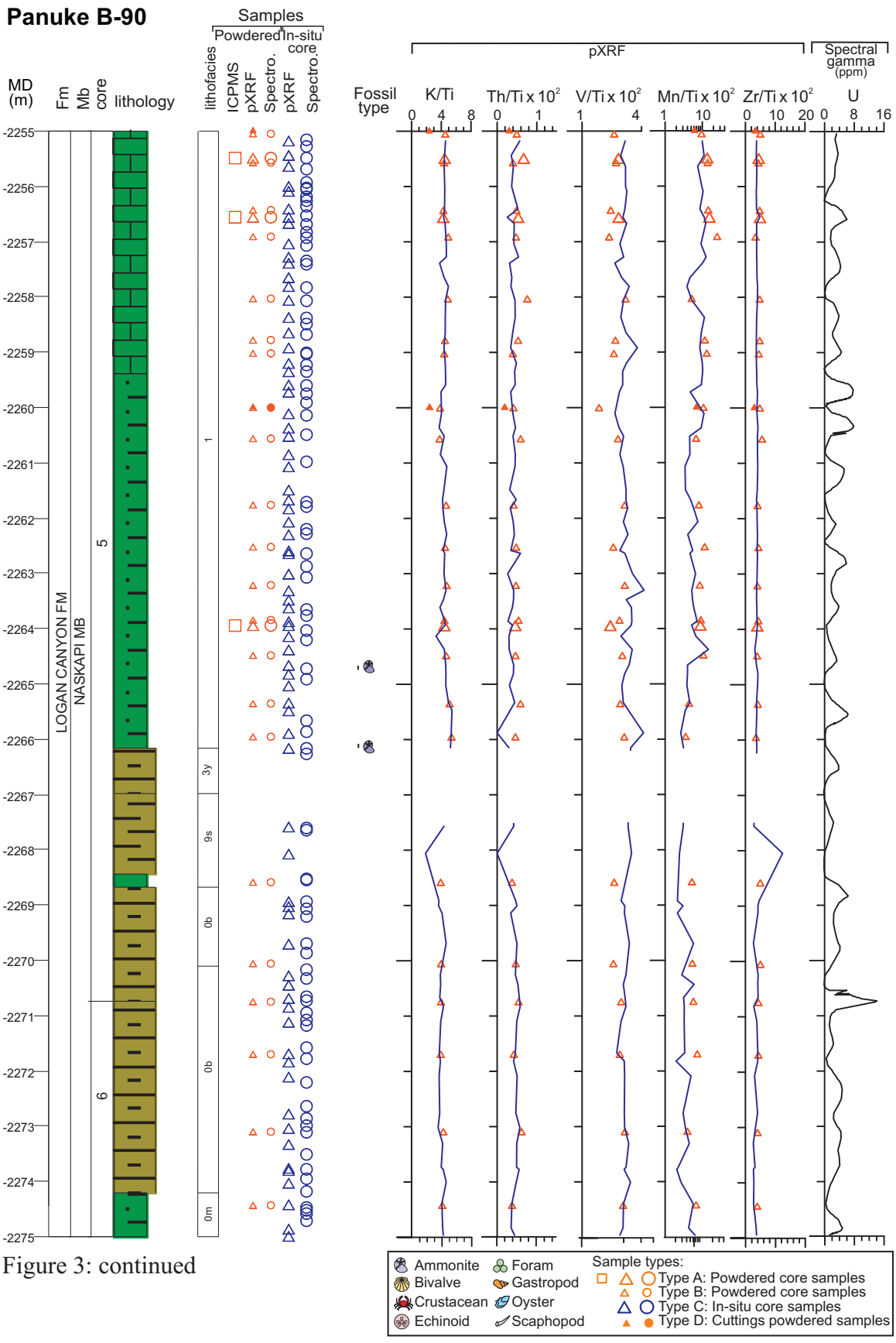

Figure 3: continued

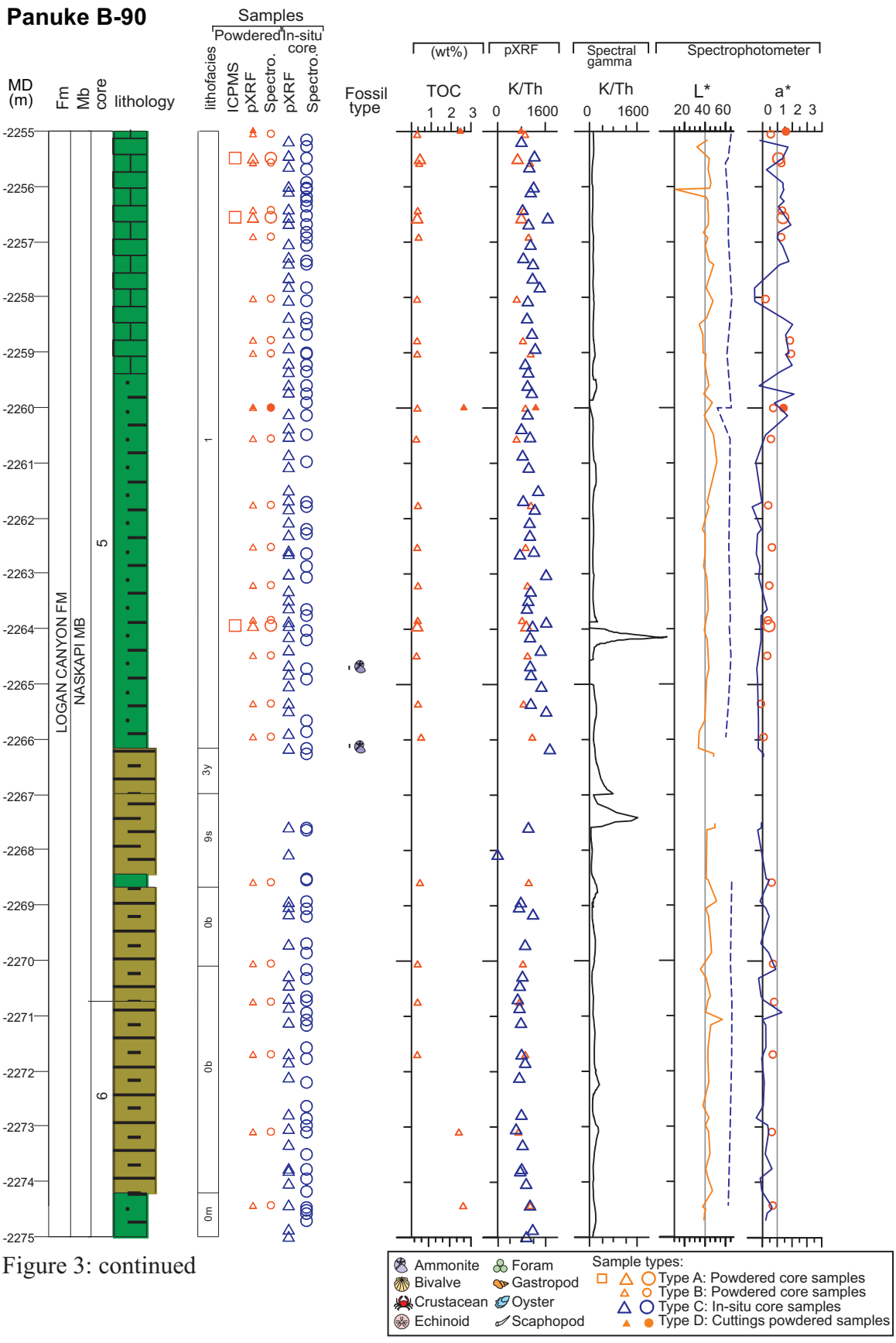

Figure 3: continued

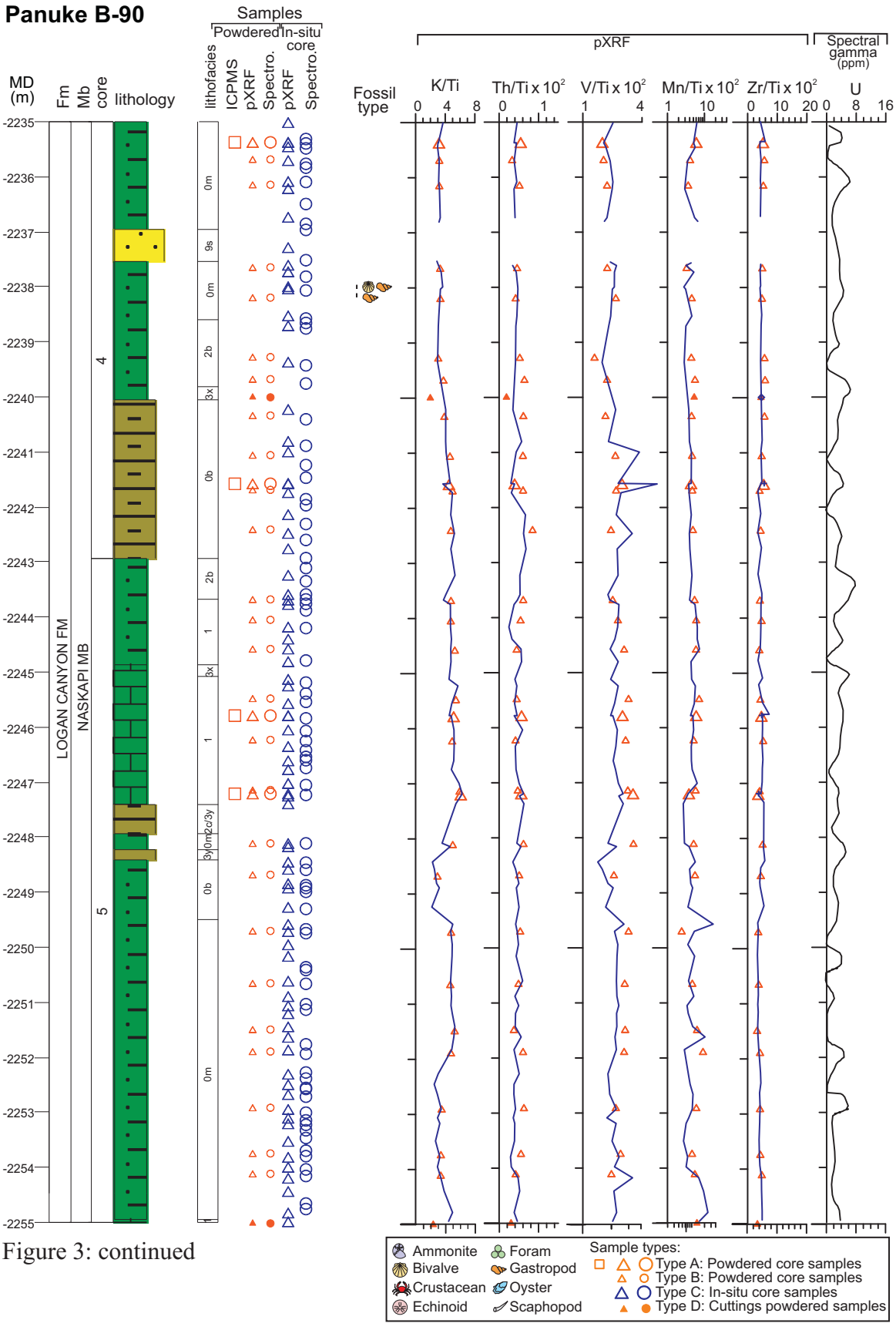

Figure 3: continued

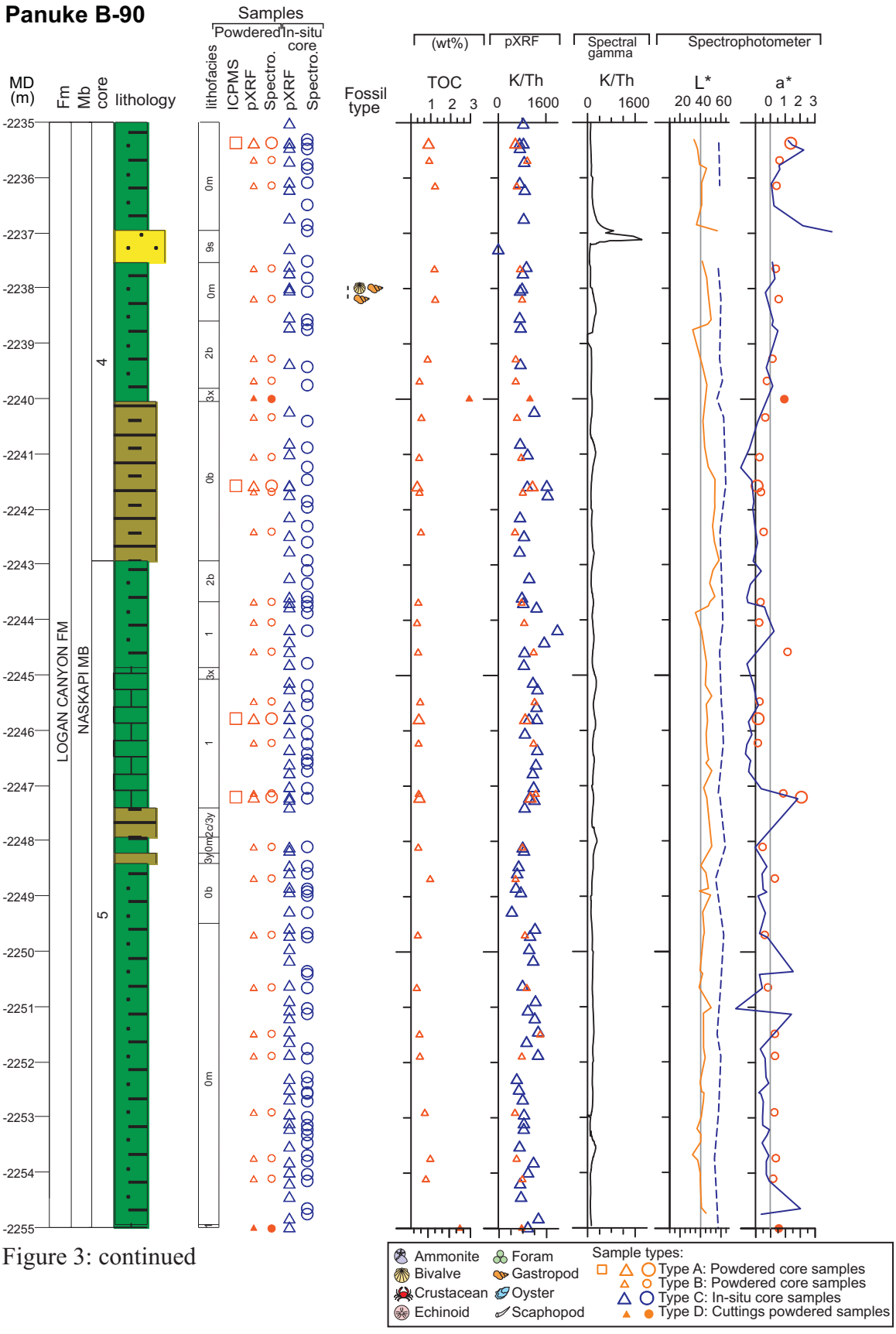

Figure 3: continued

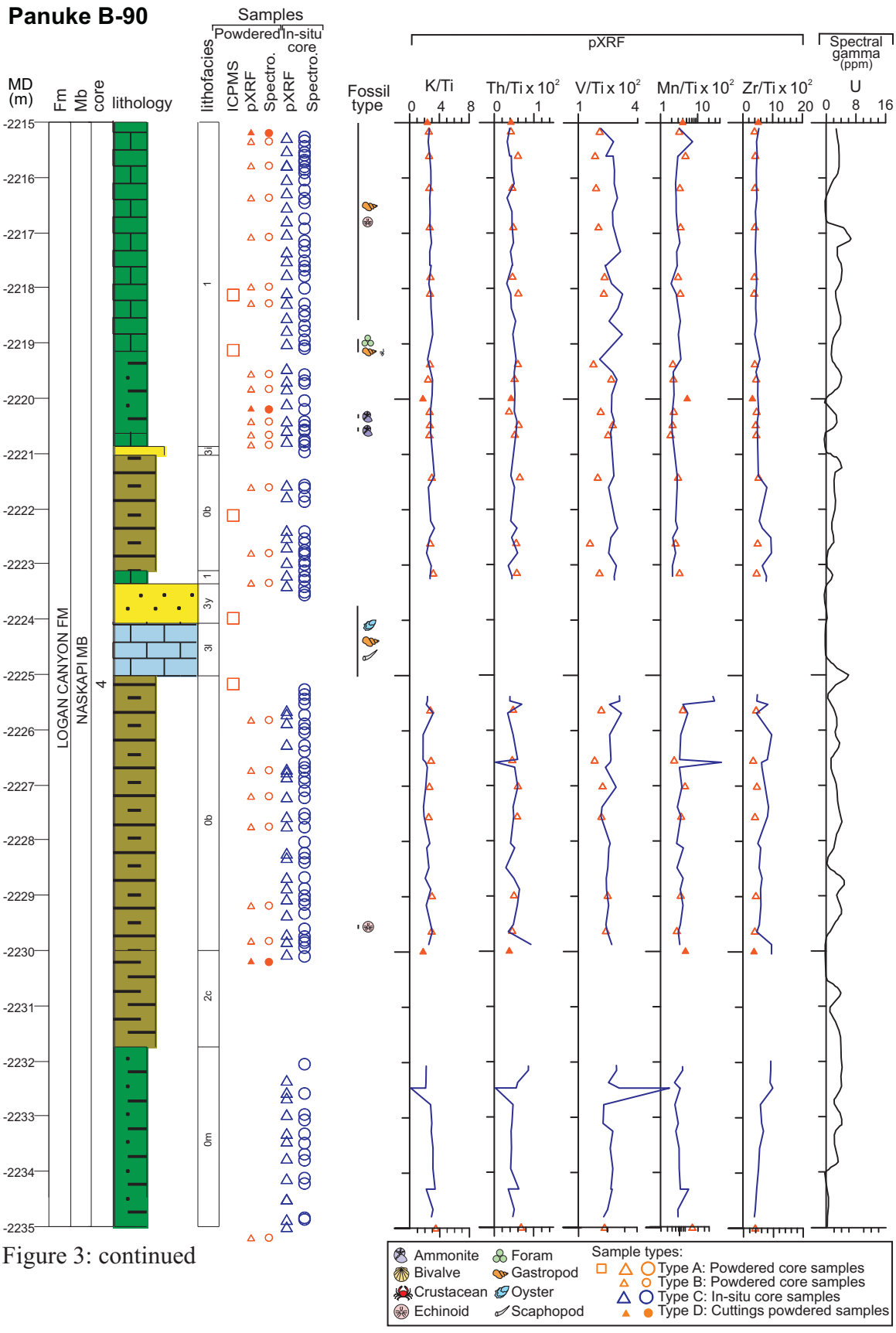

Figure 3: continued

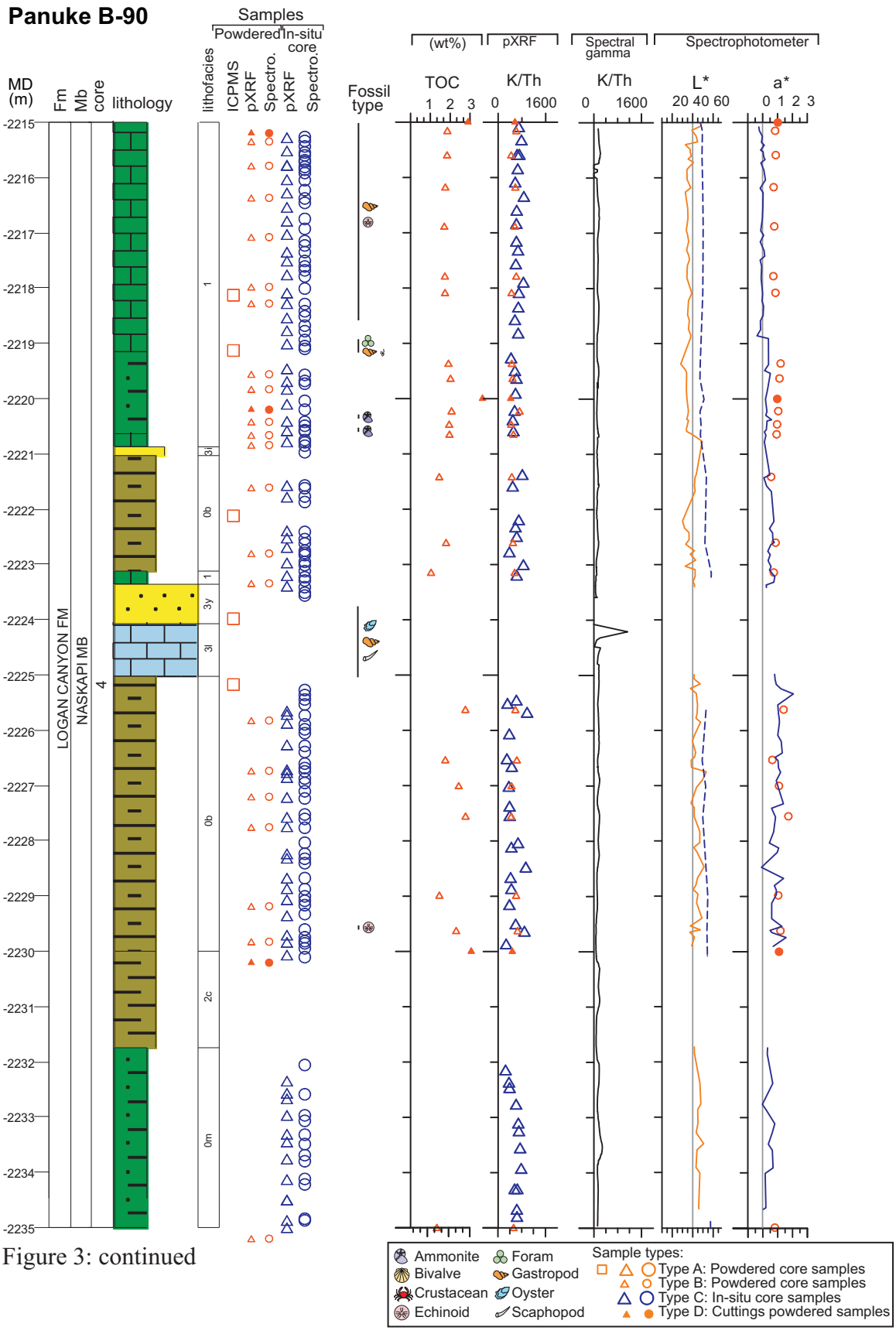

Figure 3: continued

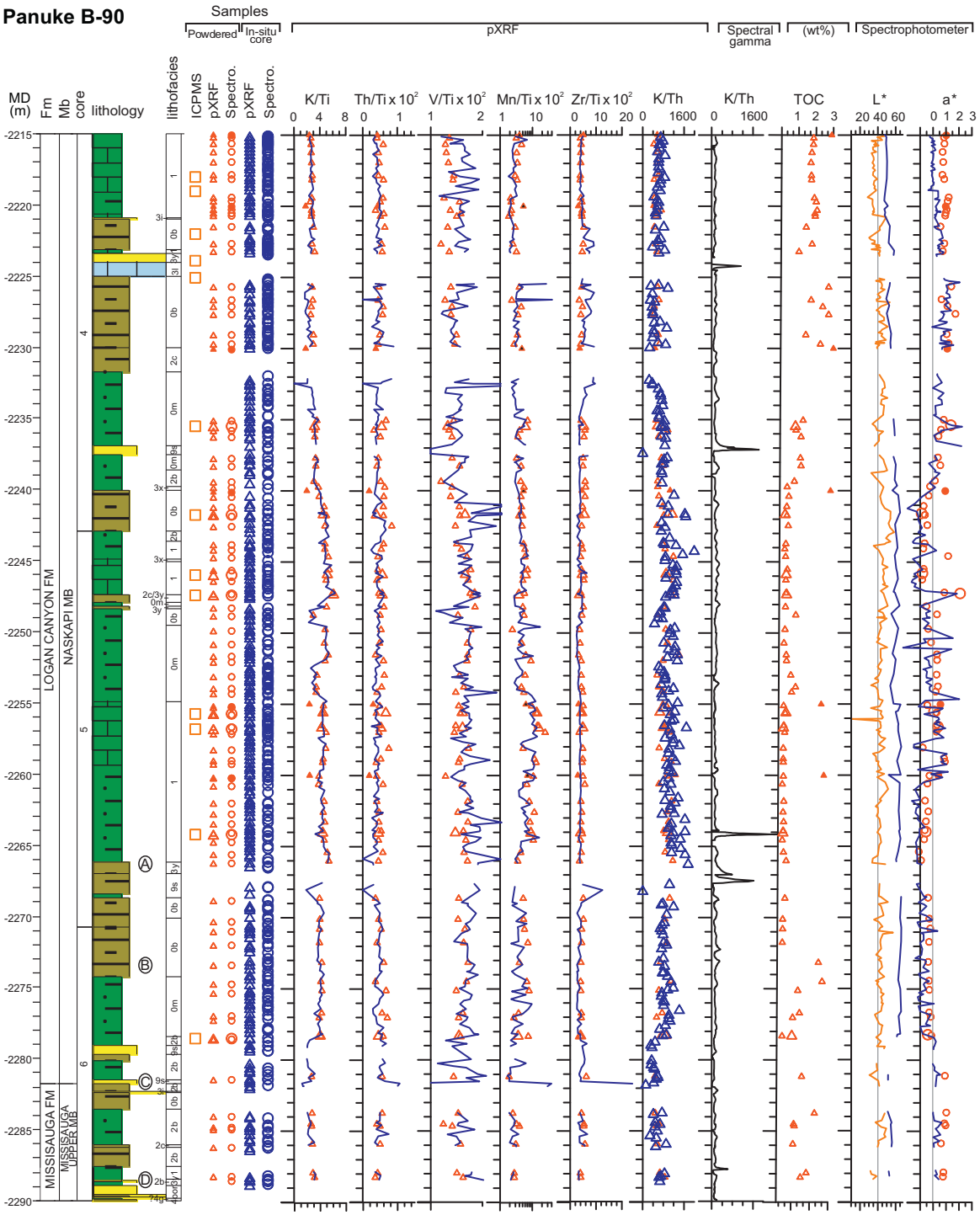

Figure 4: Summary diagram showing overall compositional and colour variation trends of the Naskapi Member from Panuke B-90 well throughout the studied core interval.

Zr/Ti ratio seems to have overall low values with some exceptions at various sandy intervals. At some intervals where shales are interbedded with siltstone, at 2221-2231 and 2240-2242 m, this ratio is also high. The U plot from spectral gamma shows no systematic trends or interesting peaks.

At the top of the Naskapi Member, TOC values in the shales vary from 1.80 wt% to 2.02 wt% (Fig. 3, Table 5). As the mudstone starts to have more sand and silt laminae and thin beds at 2219 m, the TOC values fluctuate from 1.33 wt% to 2.77 wt%. The values of TOC have a sudden decrease starting at 2235 m, going from 1.33 wt% to less than 1 wt%. The values keep decreasing with increasing depth with less than 0.50 wt%. At 2273 m TOC values increase shortly above 2 wt% and then fluctuate between 0.90 to 2.20 wt% near the base of the Naskapi Member in core 6 of Panuke B-90. TOC becomes lower when the lithofacies is 3, which comprises condensed section developed during rising (and perhaps falling) of sea-level (Table 5).

K/Th ratio from whole rock geochemical data from this study does not match perfectly the K/Th ratio from spectral gamma (Fig. 3), but they share peaks at the same location. Starting at the top of the core, there is a decrease in the K/Th ratio and goes as low as 250. The K/Th ratio from the spectral gamma shows pronounced peaks in the plot when the mudstone is interbedded with sand and silt or when the lithology changes to sandstones. From 2240 m to 2260 m, K/Th ratio from pXRF remains high in a range between 400 and 1650. At 2265 m, both pXRF and spectral gamma, K/Th ratios increase significantly. Towards the base of the studied core interval, the K/Th high values remain until after 2280 mwhere values decrease (<1000). At 2265 m, both pXRF and spectral

Table 5: Total organic carbon from powdered samples from the Panuke B-90 and Cohasset A-52

Well	Depth	Sample Type	TOC (%)
Cohasset A-52	2072.90	A	2.13
	2074.72	A	2.11
	2123.52	A	2.39
	2138.22	A	3.59
	2159.63	A	1.14
	2418.75	A	5.26
	2597.05	A	2.44
Panuke B-90	2097.27	A	5.73
	2215.15	B	1.86
	2215.59	B	1.84
	2216.17	B	1.75
	2216.88	B	1.70
	2217.78	B	1.74
	2218.08	B	1.74
	2219.36	B	1.92
	2219.63	B	2.02
	2220.22	B	2.07
	2220.46	B	1.95
	2220.64	B	1.97
	2221.41	B	1.45
	2222.60	B	1.79
	2223.14	B	1.04
	2225.62	B	2.77
	2226.53	B	1.76
	2227.00	B	2.43
	2227.55	B	2.78
	2228.98	B	1.45
	2229.62	B	2.30
	2234.99	B	1.33
	2235.37	A	0.88
	2235.68	B	0.92
	2236.14	B	1.21
	2237.64	B	1.19
	2238.19	B	1.22
	2239.27	B	0.84
	2239.67	B	0.43
	2240.33	B	0.52
	2241.05	B	0.41
	2241.57	A	0.32
	2241.68	B	0.43
	2242.40	B	0.50
	2243.67	B	0.37
	2244.04	B	0.30
	2244.57	B	0.36
	2245.47	B	0.46
	2245.78	A	0.39
	2246.22	B	0.38
	2247.13	B	0.39
	2247.20	A	0.43
	2248.10	B	0.37
	2248.67	B	0.97
	2249.69	B	0.34
	2250.64	B	0.29
	2251.48	B	0.43
	2251.88	B	0.45
	2252.90	B	0.70
	2253.73	B	0.97
	2254.10	B	0.75
	2255.05	B	0.29
	2255.49	A	0.43
	2255.57	B	0.39
	2256.43	B	0.32
	2256.56	A	0.29
	2256.91	B	0.36

Well	Depth	Sample Type	TOC (%)
Panuke B-90	2258.03	B	0.28
	2258.78	B	0.28
	2259.02	B	0.29
	2260.00	B	0.30
	2260.56	B	0.24
	2261.76	B	0.33
	2262.52	B	0.29
	2263.21	B	0.33
	2263.84	B	0.31
	2263.94	A	0.29
	2264.48	B	0.26
	2265.35	B	0.33
	2265.95	B	0.49
	2268.58	B	0.43
	2270.05	B	0.31
	2270.74	B	0.31
	2271.69	B	0.29
	2273.09	B	2.39
	2274.42	B	2.61
	2275.06	B	1.21
	2276.64	B	1.31
	2276.96	B	0.92
	2278.21	A	0.87
	2278.26	B	0.31
	2281.10	B	1.46
	2283.68	B	2.20
	2284.44	B	1.01
	2284.58	B	1.04
	2285.85	B	0.97
	2287.88	B	1.74
	2288.19	B	1.40
	2319.18	A	2.62
	2347.50	A	1.94
	2402.33	A	1.62
	2417.48	A	2.41
	2436.35	A	2.33
	2110	D	3.73
	2115	D	3.79
	2120	D	4.74
	2125	D	4.18
	2130	D	2.65
	2135	D	1.64
	2140	D	1.09
	2145	D	0.64
	2150	D	1.55
	2155	D	2.78
	2160	D	3.36
	2165	D	4.10
	2170	D	3.23
	2175	D	3.10
	2180	D	3.54
	2185	D	3.46
	2190	D	3.36
	2195	D	3.31
	2200	D	3.07
	2205	D	3.11
	2210	D	3.22
	2215	D	2.90
	2220	D	3.63
	2230	D	3.06
	2240	D	2.94
	2255	D	2.47
	2260	D	2.64

Note: Type A= Powdered core samples with ICPMS, pXRF and spectrophotometer analyses; Type B= Powdered core samples with pXRF and spectrophotometer analyses; Type D= Powdered samples from cuttings with pXRF and spectrophotometer analyses.

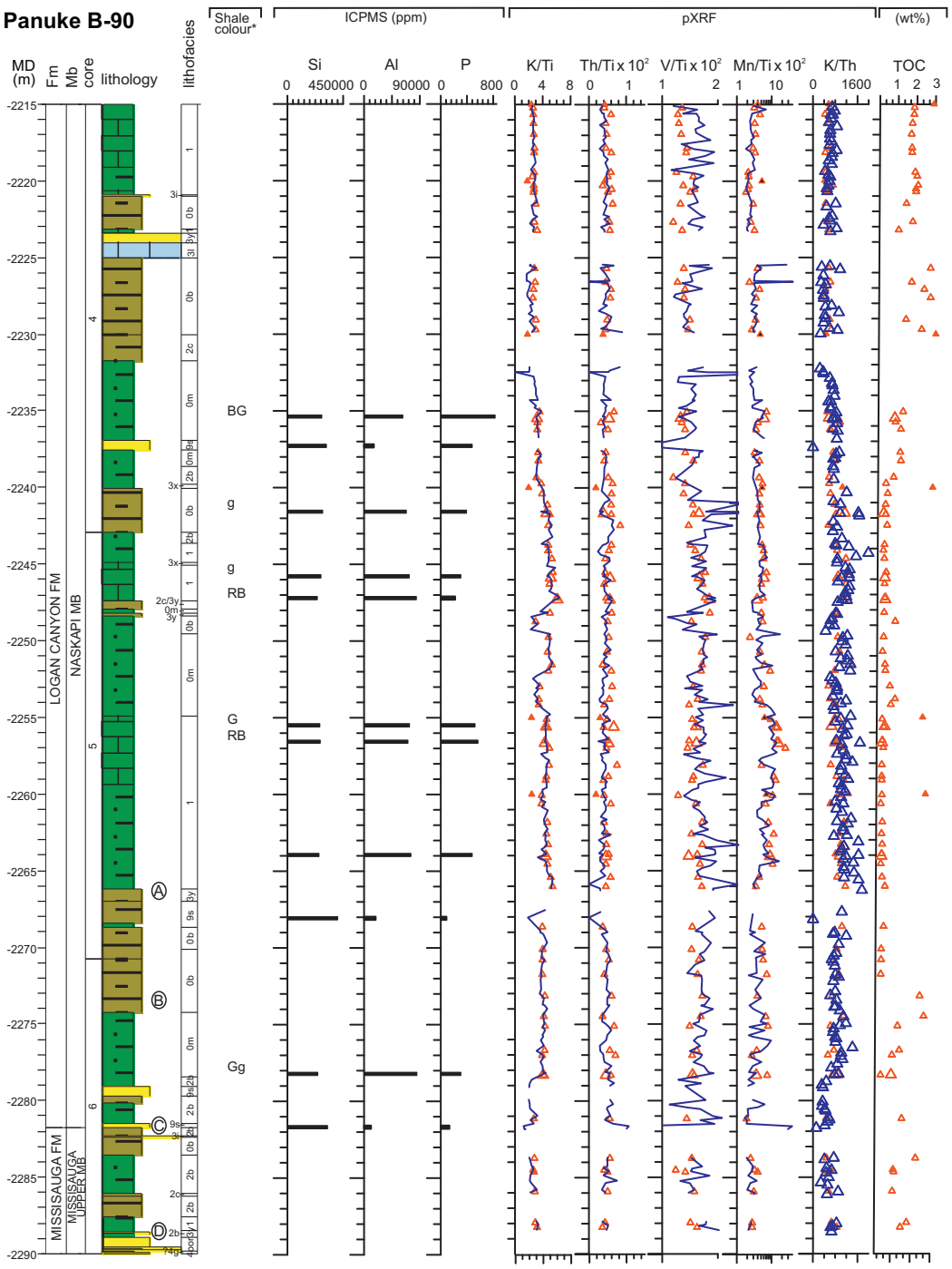

Figure 5: Summary of downcore plot showing correlation between colours from clay analyses, ICPMS Si, Al, and P analyses, pXRF elemental ratios and TOC content of the Naskapi Member from Panuke B-90 well. Colour from shales (report by Aneja, 2013): BG= brown-gray, g=green, G=gray, Gg= gray-green, and RB= red-brown.

gamma, K/Th ratios increase significantly. From 2269 m to 2240 m. K/Th ratio from pXRF remains high in a range between 400 and 1650.

The ICPMS values of Si, Al and P were measured at eleven locations within the Naskapi Member of Panuke B-90 (Fig. 5). The samples showing higher concentration of P occur with high content of TOC and brown-grey colour from the clay analyses. The red colour from the clay analyses at 2265.5 m occurs with higher levels of Mn/Ti (>0.1), whereas red clay analyses at 2247 m occurs with lower Mn/Ti ratio (<0.1).However, with only a few ICPMS measurements, it is challenging to find any distinct correlation as more data points would be needed.

The ratio Mn/Ti correlates with a* in intervals where both increase (Fig. 3). The Mn/Ti ratio and a* parameter increase at different depths, 2264 and 2260 m, respectively; and decrease at 2252 m. In Figure 6, the Mn/Ti ratio was plotted against the reliable colour spectrophotometer parameter a*. The plot shows that there is no systematic correlation between most colours and Mn content, with the exception of brown colour. The powdered samples (types A, B and D) with the visual colour grey and light grey cluster in the middle of the diagram as it is exception for normal background grey shales. The samples with brown colour show higher Mn/Ti ratio values and positive values of a*, showing correlation between colour parameter a* and Mn/Ti ratio. It seems that visual colours green and red have a distinct position along the colour parameter a*, which plot away from the majority of the samples. They plot on the negative values of a* (green) and on the positive values of a* (red).

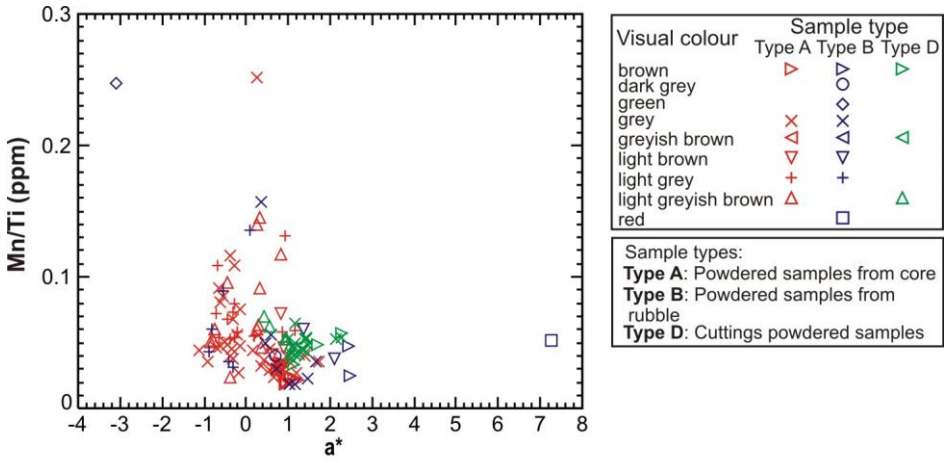

Figure 6: Mn/Ti vs. a* biplot showing a relationship between reducing conditions and colour of the samples.

The regional correlation of the four wells in central and eastern Scotian Basin, including the studied well Panuke B-90, show the base of the Logan Canyon Formation marked by an abrupt lithological change from sandstone to a dominantly shale unit (Fig. 2) in the Naskapi Member. The colours red, black, and dark colours in shale were compared in the four wells. North Banquereau I-12 and Panuke B-90 wells show both red and dark colours in shales, while Hesper I-52 and Sable Island C-67 show only dark coloured shales, including dark grey, dark brown and dark grey-brown.

5.2: Stratigraphic variations in colour from CIE L*a*b* colour system

Visually, the colour of powdered sample types A, B and D can be variable (Appendix 3 and 4). There are seven different visual colours of the sample types A, B and D, from Panuke B-90, ranging from brown, grey and greyish brown (Table 3). These colours include brown, dark brown, green, grey, greyish brown, light brown, light grey, light greyish brown and red. The samples from Panuke B-90 well have visual colours ranging from grey and brown. The visual colour of all sample types in the study is quite

variable compared to the variation in CIELab colour analyses measured, which could be due to irregular reflection from core surfaces. Consequently, the spectrophotometric parameters of L* and b* (not shown) on the sample type C do not correlate with the parameters from the powdered samples.

The approximate range in L*a*b* for each observed visual colour (Table 3) shows that darker visual colour such as the browns, red and greyish brown have lower L* than green and the light greys. The colours brown, light brown, red and greyish brown have positive a*, while the colours green and greys have negative a*.

Samples from Cohasset A-52 well have the largest visual colour variation, showing the typical brown, grey and greyish brown ranges with the addition of green and red. The visual colours red and green possess distinct colour ranges seen in their respective L*a*b* parameters (Table 3).

In the down core plot (Fig. 3), the parameter L* from the in-situ core samples (type C) is lower and does not correlate with the powdered samples (types A, B and D). Unlike parameter L*, the plots for the parameter a* from both in situ core and powdered samples seem to correlate well. These parameters, L* and a*, do not correlate with each other.

The L*a*b* values were displayed on a ternary plot (Fig. 7A), with the parameter a* recalculated to (a* + 3.1) x 10 to obtain positive values. There seems to be one main trend of almost all the samples, with the exception of the visual colour green, which plots on a trend away from a* to L*. The visual colours green and red both plot on opposite sides from each other. Red plots towards the a* apex, while green sample plots on the b*

line approaching L* apex. The visual colours brown, dark brown and light brown plot on the main trend approaching the apex L*, as the sample colour becomes lighter. The visual grey shades show high lightness L* and lower chroma a*. It seems that there is a moderate correlation between visual colours and the colours determined by CIELab approach. The sample type D has less visual colour variation compared to the sample type A and B. The sample type A show the highest variation, including the distinct green and red shale.

In most cases, the spectrophotometric parameters L*, a* and b* seem to be better discriminators of colour than the variation in visual colour. There are factors affecting the visual colour of in-situ core samples (sample type C), but these factors tend to not play a role for powdered samples (sample types A, B and C). Powdered samples are homogenous, unlike in-situ core, which contain inhomogeneities, fractures, and microfractures.

The plot L* vs a* (Fig. 7B) shows visual colours green and red plot on the opposite side of each other. The green sample plots a negative value of a* (green) with high L* (lightness), indicating a light green colour. The red sample plots a positive a* value (red) with also high L*, indicating a light red colour. The plot shows a better correlation between visual colour and spectrophotometric parameters L* and a*. The visual colours seem to be grouped accordingly, such as brown and greyish brown seem to plot towards positive a* values (red), unlike on the ternary plot. The values from the parameter L* proved to be not as reliable as the parameter a* when it comes to quantifying colour ranges due to high variation between the in-situ (type C) and powdered (types A, B and C) sample plot (Fig. 3).

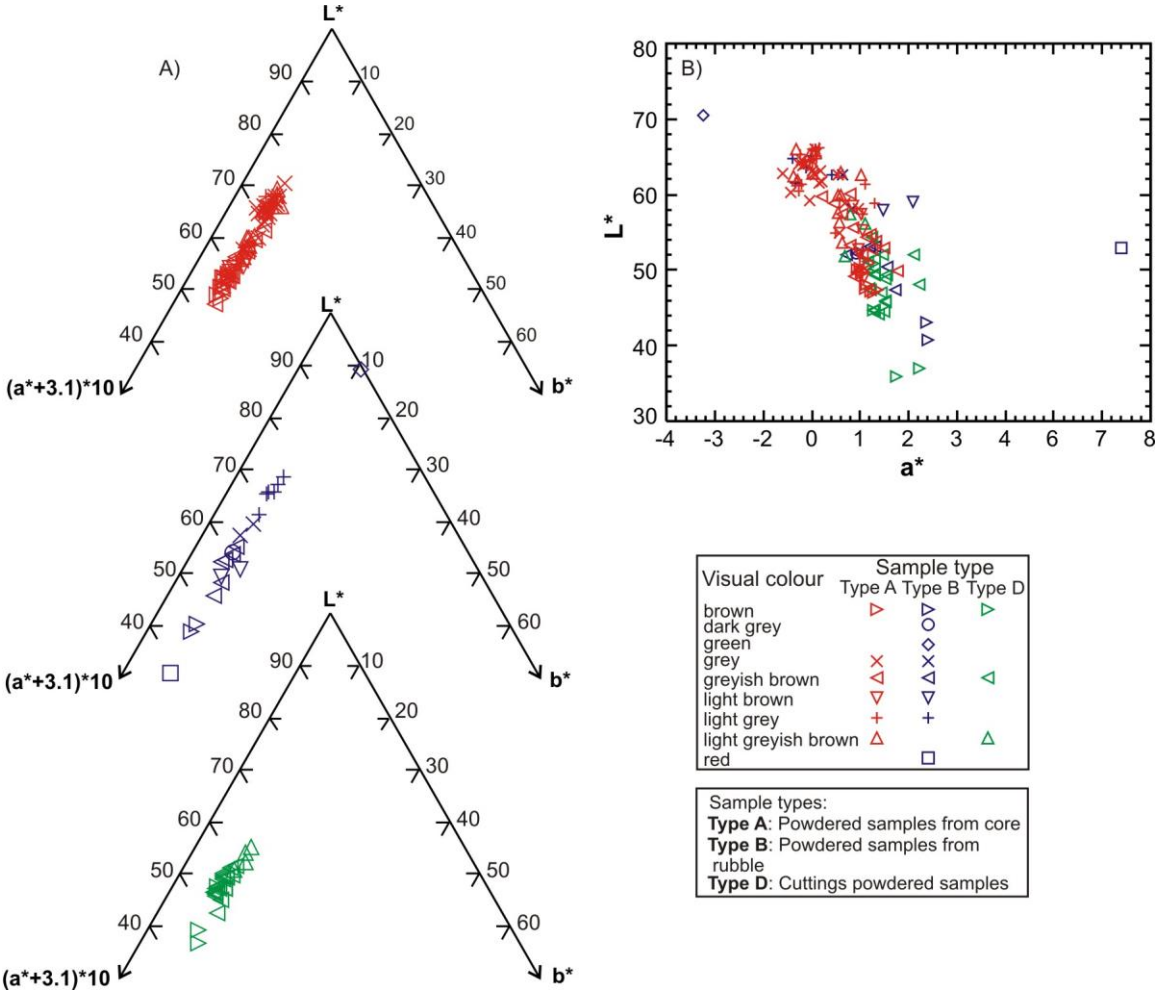

Figure 7: Plots showing colour variation between in-situ core and powdered samples. (A) Ternary plot showing the relationship between L*, a*, and b* spectral data. (B) Biplot of L* and a* from spectral analyses from Panuke B-90. Symbols for (A) and (B) indicate different visual colours and different colours indicate type of powdered samples: red is rubble, blue is core and green is cutting.

5.3: Macrofossils as indicators of paleoenvironment

From the literature, the macrofossils present in the Naskapi Member of the Panuke B-90 well include gastropods, echinoids, forams, bivalves, ammonites, scaphopods, oysters and rare crustaceans (MacRae, 2011; Tables 6 and 7). Bivalves, gastropods, crustaceans, and oysters can live either in marine, estuarine, or brackish water. To determine the environment, we need to find an association with another fossil that is restricted to a specific environment. Ammonites and echinoids are found to be very useful environment indicators as they are found only in fully marine environments. Other macrofossils such as forams and scaphopods are found in marine environments and are rarely found in brackish water, but their environment can be confirmed with the association of ammonite or echinoids present in the same interval or succession.

MacRae (2011) recognized two macrofossil assemblages: high diversity and low diversity of macrofossil body fossils. The high diversity assemblage, based on the low tolerance of echinoids and ammonites to reduced salinities, is interpreted to indicate normal marine salinity waters. The low diversity assemblage, based on the abundance of oysters, is interpreted to indicate a stressed brackish-water environment. Scaphopods, gastropods, and bivalves were observed as components of both assemblages, but in abundance they indicate a brackish environment. Crustaceans were observed only in high diversity normal marine environment. The environment where these fossils lived tells us more about the depositional environment of the sediments that we are analyzing. We know that the depositional environment for the sediments in the area of study changed, giving us different lithologies such as multi-colour shales, mudstones, sandstones and limestones.

Table 6: Summary of macrofossil types in Naskapi Member of the Panuke B-90 well (modified from MacRae, 2011).

Well	Core	Box	Specific Depth (m)	Fossil type
Panuke B-90	4	1	2215.00-2215.75	high-spired gastropods, echinoids
		2		high-spired gastropods, echinoids
		3		high-spired gastropods, echinoids
		4		high-spired gastropods, echinoids
		5	2218.50-2218.55	high-spired gastropods, echinoids
		6	2218.95-2219.16	pyritized forams, high spired gastropods, small bivalve, other gastropods, echinoids.
		8	2220.33	ammonite
			2220.56	ammonite
		13	2223.76-2224.46	oysters, minor gastropods and scaphopods
		14	2224.46-2225.00	oysters, minor gastropods and scaphopods
		21	2229.58	echinoid
		32	2237.98	asymmetric bivalves, knobby gastropods
		33	2238.12	knobby gastropods
		overall occurrence		bivalve, gastropod, scaphopod, echinoid, and ammonite
	5	30	2264.65	ammonite
		32	2266.1	ammonite
		overall occurrence		Ammonites (deshayesites, prodeshayesites), bivalves, gastropods including aporrhaid gastropods, scaphopods, rare crustacean fragments, irregular echinoids, small disarticulated cup-shaped oysters
	6	10	2277.83	small bivalves
		19		ammonite
		overall occurrence		oysters, small bivalves, gastropods, scaphopods, and echinoids

Table 7: Summary of environment of macrofossil found in the Naskapi Member of the Panuke B-90 well (modified from MacRae, 2011).

Macrofossil	Environment			Fossil Record	Notes
	Marine	Fresh water	Brackish water		
irregular echinoid	√ preferentially normal salinity			Cambrian - Recent	
ammonite				Jurassic - Cretaceous	
oyster	√		√	Jurassic - Recent	also esturine water
gastropod	√	√	√	Cambrian - Recent	needs to be specified by associations
bivalve	√	√	√	Cambrian - Recent	needs to be specified by associations
foram	√			Cambrian - Recent	rare in brackish water
scaphopod	√			Cambrian - Recent	rare in brackish water
crustacean	√ (prob)	√	√	Carboniferous - Recent	needs to be specified by associations

Chapter 6: Assessment of methods used

The advantages of the portable XRF instrument are that it can be portable and also be used non-destructively directly on core/ sediment or on a stand on powdered samples. It gives relatively precise analyses based on comparison with ICMPS geochemical data. However, there are some limitations to using this method. The instrument is sensitive to irregular surfaces, fractures, dust and is also influenced by local material of different composition such as concretions. The sample to be analyzed should have a smooth and flat surface and is preferably thicker than 1 cm on all types of samples. Any kind of surface disturbance can have an effect on the analyses. Therefore, the availability and suitability of the sample is crucial. The preparation for the powdered samples is time consuming, as more steps are needed before analysing. All analyses need to be performed by a certified technician who possesses a licence to use the instrument due to radiation safety precautions (Table 8).

Spectrophotometry analyses offer a fast, cost-effective and quantified colour range. The instrument is easy to operate and can be used either on a flat and smooth surface of core, or on powders. It can be portable or can download to a computer when analyzing. As the XRF analyses, surface disturbances are also a limitation for the spectrophotometer when taking measurements directly on core. In this study, we noticed that the spectrophotometric parameter L* and b* measured directly on core did not reliably represent the colour. The variation in colour between in-situ (type C) and powdered (types A, B and D) samples was much higher compared to the parameter a*, which showed good correlation between both sample types.

When using the XRF, it is important to know what elements are of interest from the beginning because different beams of the XRF count the energies of different elements and the detection limit of elements varies. When analyzing in-situ core samples, it is important to take analyses that are representative of the lithology that is being studied, avoiding areas of varying lithology, fractures or concretions. When analyzing powdered samples, it is vital to homogenize the powders and to choose the appropriate film. The choosing of the thin films depends on the element of interest in order to prevent the least amount of disturbances in the photon transmittance of the analyses.

When using the spectrophotometer, it is important to analyse samples that are representative of the core's colour variability and are relevant to the study. Keeping a record of the visual colour and any other observations of the analysed sample is important in order to decide colour ranges based on the spectroparameters L*, a* and b*.

ICPMS is a fast laboratory method to obtain whole rock geochemical analyses. It is commonly chosen because it provides a wide range of sensitivities with detection limits between 10^8 and 10 ppb depending on the elements to be analysed . This method also provides accurate results from a wide range of elements that are analyzed simultaneously (30 to 40 trace elements). The samples have to be sent to a laboratory, where additional steps are done, such as pulverization and digestion of the samples into a liquid, before the analyses are taken. Compared to pXRF, ICPMS has lower detection limits, providing a more complete set of analyses.

For this study, the ICPMS geochemical analyses served as a comparison guideline to assess the precision of the pXRF analyses. Biplots of the elements of interest between

Table 8: Summary of advantages and disadvantages of methods used.

Methods	Type	Advantages	Disadvantages	Applications	References
This study:					
Spectrophotometry CIELab	in-situ	Non-destructive		Facies characterisation	Helmke et al., 2002
		Easy to use and maintain	No identification of constituents		Debret et al., 2006
		Portable for the field			Roth and Reijmer, 2005
		Fast to implement			
		Capable of high resolution		a*: iron oxide content b*: diatom vs terrigenous L*: aragonite or calcite content	This study
		Vast range of applications			
	Powder	Homogeneous	Preparation of sample is time consuming		
		Can use rubble and cuttings	Contamination of sample	Quantification if calibrated with geochemistry	
		Fast	Little loss of sample when analyzing		
		Precise results (wider range in colour)	Requires enough sample		
pXRF	in-situ	Non-destructive	Sensitive to fractures, heterogeneities, dust	Measures elements of redox and/or paleoproductivity significance	This study
		Cost-effective	Need of license to use instrument		
		Do not need to move core	Cannot use instrument stand, have to hold it by hand		
		Accurate enough	Need big and deep enough surface to analyze		
		Fast	Need flat and smooth surfaces		
	Powder	Homogeneous sample	Preparation of sample is time consuming		
		Can use rubble and cuttings	Possible contamination and loss of sample		
		Can use instrument stand	Requires more steps and utencils to prepare sample		
		Representative composition	Need of license to use instrument		
		Precise results	Requires enough sample		
From previous studies (Gould et al., 2014, Gould et al., 2012):					
ICPMS		Fast analyses	Requires pulverized sample	Measures whole rock geochemistry	Zhang et al., 2014
		Accurate results	Requires digesting the sample		
			High cost	Sediment provenance	
		Low detection limits	Preparation of sample is time consuming		
Spectral gamma		Fast and inexpensive method	Only available for a few wells	Correlation of wells	Gould et al., 2014
		Availability of data from oil companies and scientific boreholes		Identification of sediment facies	Ruffel and Worden, 2000
				Interpretation of hinterland paleoclimate	

both pXRF analyses (this study) and ICPMS geochemical analyses (Gould et al., 2012) showed that there is a good linear correlation. The in-situ XRF analyses show a weaker correlation than the powdered analyses due to surface disturbances that may have affected the measurements. Heterogeneity including concretions, fossils, and microfractures are present in the conventional core, but are not present in the homogeneous powders.

The biplots of elements of interest showed that most elements display above 74 % of total variance (Table 4, Figs. A1 and A2). The powdered sample (types A, B and D) values display above 90% of total variance and a linear correlation, with the exception of the elements Cr, Th and V. The in-situ core (type C) sample values display total variance above 74 % in a linear correlation, with the exception of Cr, V, Th and S. In both sample types, the same elements Cr, Th, and V plotted away from the mean, which indicates interference when analyzing them. It is common to have inter-element interferences when analyzing environmental soil samples; for example, high levels of Fe can interfere with low levels of Cr (Innov-X Systems Delta Handheld XRF Analyzer manual).It was thus shown that both methods, pXRF and ICPMS, can be used to indicate paleoenvironmental proxies.

Chapter 7: Discussion

The Early Aptian is a period of climate and environmental change during which important episodes of environmental change (EEC) developed, including the well-known and studied Selli Episode. The organic carbon-rich deposits in the Early Aptian, which are associated with fluctuations of atmospheric CO_2 from intensified volcanic activity, are widespread worldwide (Föllmi, 2012). The changes in global atmospheric CO_2 level caused an effect in aridity and humidity in the hinterland, in sea level, in ocean circulation, and in ocean acidity and the rate of sediment supply was affected by tectonics in the hinterland. These effects are preserved in the sediments and can be recognised in different basins around the world.

7.1: Age Model

All species of ammonite *Deshayesites* are restricted to Early Aptian (Bogdanova and Mikhailova, 2004), thereby the occurrence of species *Prodeshayesites* in the Boreal realm and the species *Deshayesites* in the Tethyan realm mark the lower Aptian. The presence of ammonites is also considered a useful indicator of a marine environment (MacRae, 2011). MacRae (2011) recognised four erosion surfaces ("A, B, C, and D" in Fig. 4) from the Upper Missisauga to the lowest part of the Naskapi Member in the Panuke B-90 well, that indicate the change of conditions in the environment of deposition.

The first erosion surface recognised in the Upper Missisauga, as defined by Maclean and Wade (1993) ("D" in Fig. 4), marks a change in lithofacies and biofacies from brackish/estuarine environments below to normal marine above. The lithology above this marker, still interbedded mudstone and sandstone, shows cross stratification

and moderate to strong bioturbation. The macrofauna becomes more diverse upwards towards the Upper Missisauga-Naskapi lithostratigraphic boundary as defined by Maclean and Wade (1993). At this boundary, another erosion surface developed ("C" in Fig. 4) where the presence of lithofacies 3 suggests the transition to normal marine shelf environment in the Early Aptian. Uncertainty on the precise position of the Barremian-Aptian boundary was inferred by MacRae (2011) based on the distribution of ammonites at the top of the Missisauga Formation and near the base of the Logan Canyon Formation in the well. The presence of *Deshayesites* species within the uppermost Missisauga Formation in Panuke B-90 and other wells (i.e. F-99 well) suggests the beginning of the Aptian deeper into the Missisauga, perhaps where the erosion surface "D" is located.

Smaller erosion surfaces occurred throughout the Naskapi Member interval of the well, indicating hiatuses in normal marine and below normal wave base conditions on a marine shelf. The overall evidence suggests a deepening of the marine environment towards the top of the Naskapi Member, which correlates with the Intra-Aptian Maximum Flooding Surface (MFS) identified by the Offshore Energy Technical Research Association "Play Fairway Analysis" (OETRA PFA) biostratigraphy team (Weston et al., 2012). The Selli Event occurred soon after the MFS (Ogg et al., 2004), still within the Early Aptian.

7.2: Sea-level

Global sea level can change either 1) by changes in the amount of water in the ocean including sequestration of glacial water in ice caps, deglaciations and the variations of ocean's water exchange with the deep mantle or 2) by changes in the volume of ocean due to tectonic activities (Haq, 2014). It has been suggested that black-shale episodes

such as the Selli Event are consequence of rapid eustatic sea level rise (Grötsch et al., 1998), however, evidence suggests that this might not be the only cause.

More information is needed to determine whether the sea level cycles were in fact eustatic. Nonetheless, eustasy cannot be ruled out, considering that there were ephemeral ice sheets on the Antarctica present at this time (Haq, 2014). Tectonic processes seem to have been one of the major factors leading to basin scale paleogeographic changes along with dynamic topography. In the Scotian Basin, the Cobequid-Chedabucto-SW Grand Banks fault system reactivated in the Late Jurassic. However, the rapid increase in subsidence rate in the Early Cretaceous cannot be attributed to regional cooling of oceanic lithosphere or to isostatic load effects from seamount volcanoes (Pe-Piper and Piper, 2004), but is a consequence of salt tectonics (Kendell, 2012).

The changes in lithofacies and biofacies have shown (Figs. 3 and 4) that during the Late Barremian and early Aptian of the Panuke B-90 well several regression-transgression cycles occurred. These changes are indicated by the lithofacies 3 (with the exception of erosion surface "B" with the lithofacies 0), which represents lowering of the sea level. Lithofacies 3 occurs as a transgressive unit in deep water as a result of sea-level changes, indicated by intraclast conglomerate and muddy sandstone, which are absent in the shale sections. Lithofacies 0 indicates a transition from river mouth to shoreface with the presence of mudstone interbedded with fine sandstone and siltstone (Gould et al., 2011). These intervals have mostly brackish or estuarine fossils, in contrast to mostly normal marine fossils in the thick shale intervals.

At least nine sea-level lowstands were recorded in a relatively short period of four million years, an average of 0.4 Ma per sea-level cycle during the base to the middle of the Naskapi Member. Haq (2014) studied sea-level changes in the Cretaceous and identified short-term sea-level events with a varied duration between 0.5 Ma and 3 Ma, with an average of 1.38 Ma/cycle. These short-term sea-level events are difficult to explain compared to long-term sea-level events.

7.3: Black shales with high Total Organic Carbon (TOC)

TOC results show two small peaks at the base of the uncertain "Barremian-Aptian" boundary, followed by a subtle peak in the middle (~2254 m) and a prolonged high peak towards the top of the cored part of the Naskapi Member (Fig. 4).

The peaks of organic carbon seem to occur after episodes of regression (lithofacies 3 in Figs. 3, 4 and 8). Masse and Fenerci-Masse (2013) recognised flooding events in the Late Barremian- Early Aptian platform carbonates of SE France (Fig. 8), which preceded the formation of black shales, including the main Selli OAE. In the Scotian Basin, there seems to be a correlation of the flooding events with the distribution of ammonites.

The late Barremian is characterized by lower organic-matter preservation in the Tethyan basin and cooler temperatures (Ruffell and Batten, 1990), which changed towards the Barremian-Aptain boundary with an increase in organic-matter burial (Stein et al., 2012). Föllmi et al. (2012) recognised short-lived anoxic episodes occurring in between the Faraoni OAE in the Late Hauterivian and Selli OAE in the Early Aptian, two of which are shown in the TOC plot of this study above erosion surfaces "C" and "B"

(Fig. 4). Both of these OAEs are associated with intensified volcanic activity and environmental change that lead to higher rates of primary productivity, nutrient rates, and conditions of ocean anoxia (Baudin, 2005; Tejada et al., 2009). The series of thin organic-rich mudstone interlayers extending into the Barremian and Aptian have low TOC values (less than 2 wt%) and have been documented in the central Tethyan realm (Heldt et al., 2008), northern Atlantic (Weissert, 1981; Bralower et al., 1994) and Lower Saxony Basin (Mutterlose et al., 2009, 2010).

The correlation of the TOC-rich black shales from 2215 to 2230 m with the Selli event is based on the presence of the specific ammonites of the genus *Desheyesites* sp. indicating Early Aptian age, the sequence thickness, the location of the intra-Aptian MFS based on lithology and climate, and the presence of an important sea-level lowering correlating with the sea-level lowering in Fig. 8 within the middle of the limit.

The Selli Episode was the first OAE in the Tethys to be identified and organic-rich sediments associated with this event were recognised in marine basins in France (Breheret, 1988, 1997), Germany (Kemper and Zimmerle, 1982; Mutterlose et al., 2009), Turkey (Yilmaz et al., 2004), the southern Tethyan realm (Heldt et al., 2008), the central and southern Atlantic (Bralower et al., 1994) and the middle and northwestern Pacific (Sliter et al., 1989; Bralower et al., 2002).

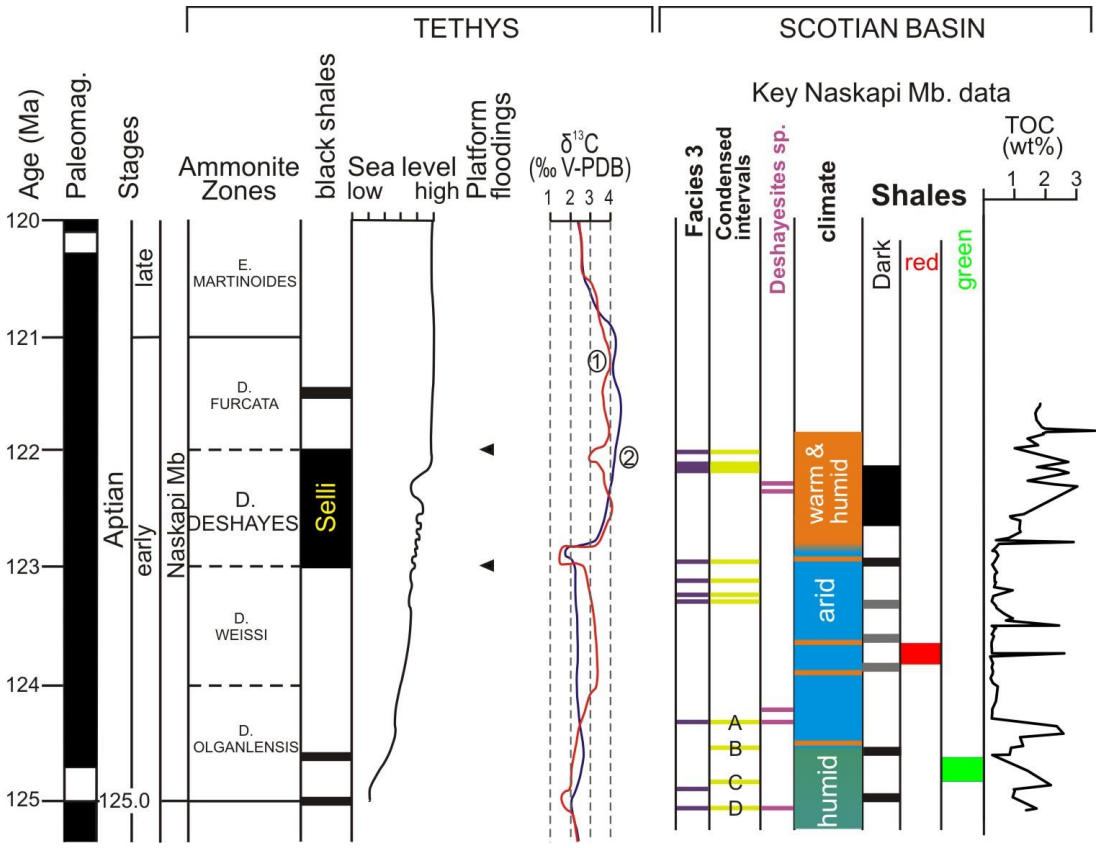

Figure 8: Synthesis diagram showing paleoceanographic and paleoenvironmental trends for the Early Cretaceous. From left to right: Timescale after Cohen and Gibbert (2014); paleomagnetic reversal scale after Haq (2014) and Follmi (2012); biozones after Haq (2014) and Föllmi (2012); Tethys black shales record after Coccioni et al. (2006); sea level curve after Peropadre et al. (2013); flooding events after Masse and Fenerci-Masse (2013); the acidification of ocean waters after Skelton and Gili (2012) and whole rock carbon isotope records ($\delta^{13}C$): (1) after Emmanuel and Renard (1993), Hennig et al. (1999), Van de Schootbrugge et al. (2000), Herrle et al. (2004), Godet et al. (2006) and Föllmi (2006); (2) after Sprovieri et al. (2006).

7.4: Green and red shales

An unusual erosion surface ("B" in Fig. 4) in the Naskapi Member interval of the Panuke B-90 well marks a shale-on-shale contact between grey well-bioturbated mudstones below and greenish-grey non-bioturbated shales above. These shales are finely laminated and usually lack of bioturbation, except the silty and sandy beds that have intermittent zones of macrofauna and ichnofauna. Ammonites of the genus *Deshayesites* are present in abundance in the intermittent intervals. The colour of the shales grades from greenish- grey to pale reddish to brownish grey with sporadic maroon siderite cement. The colour remains a matter of debate because there are no similar shale units in the Early Cretaceous succession in the Scotian Basin. MacRae (2011) suggested a marine shelf environment well below normal wave base for this unit, representing a transgression to deeper water conditions. There are two theories about the development of anoxic conditions in oceanic water. The first theory is based on eutrophication, whereas the second theory is based on ocean water acidification.

The changes in climate and rainfall distribution along the Atlantic-Tethys seaway as a consequence of intensified volcanic activity might have caused the biocalcification and platform crisis based on eutrophication. The elevated CO_2 levels in the atmosphere and increased rainfall enhanced global warming, thus favoured weathering, erosion and runoff patterns. P is considered an important and limiting nutrient that is derived from continental weathering, and influences primary productivity in oceans. The flux of dissolved P into the ocean is mainly controlled by continental runoff via river water (Föllmi, 1996). P transfers into the sedimentary reservoir incorporating into organic matter or aggregating in clay particles and iron and manganese oxyhydroxides (Delaney,

1998). The increase in P levels increased the nutrient level by consuming the oxygen in the water and accumulating organic matter in oxygen-deprived areas.

An alternative theory was suggested by Skelton and Gili (2011). In this theory ocean acidification is the cause for platform crisis (reduction in biodiversity on carbonate shelves) and thus the appropriate conditions of organic carbon sequestration in sediments. The increase in atmospheric pCO_2 levels from volcanic activities reached a thermal maximum and was followed by cooling and lowering of the ocean water pH. The pH and carbon supersaturation of the oceans decreased to the point that nannofossils did not need or could not calcify (nannoconid crisis; Erba and Tremolada, 2004). The acidification of sea water inhibited biocalcification in surface waters and caused the uplift of the carbonate compensation depth (CCD) (Heldt et al., 2008; Erba et al., 2010). Consequently, the accumulation of higher nutrient from weathering, phosphate additions from anoxic sea floors and through bacterial nitrogen fixation, increased the fertility and intensification of organic carbon sequestration in sediments (Weissert, 2000).

From both theories on the development of oceanic anoxic events, the acidification hypothesis seems to correlate with the samples from the Naskapi Member in Panuke B-90 well. The water acidification, which is synchronous with Tethyan samples, agrees with the presence of green shales lacking of bioturbation in the Panuke B-90 well.

In Panuke B-90 well, red shales occurred above the greenish-grey shales (Figs. 2 and 4). The high peak of Mn/Ti ratio and the high peak of the parameter a* (Fig. 4) indicate the occurrence of red shales soon after the occurrence of the unusual greenish-grey shales at the bottom of the Naskapi Member (Early Aptian). In the Late Cretaceous,

Cretaceous Oceanic Red Beds (CORBs) are common. The deposition of CORBs was highly abundant during the Late Cretaceous in the middle to low latitude basins of the Tethys, Atlantic, Indian and Pacific Oceans. Nonetheless, these deposits were also increasingly widespread from the Aptian through the Campanian (Wang et al., 2011). CORBs occurred when the climate cooled as CO_2 levels in the atmosphere decreased due to decrease of seafloor volcanic activity (Larson, 1991) and burial of large amounts of organic carbon (Berner, 2003). Global cooling enhanced cold deep water and dissolved oxygen content, increasing its oxidizing capacity (Wang et al., 2011).

The colour variability of sediments is a representation of the climatic and environmental conditions when deposition occurred. The sediments deposited under reducing conditions or oxidizing conditions will have characteristic colours, black to greenish-grey or reddish brown, dark brown respectively. The Scotian Basin is on a shelf, whereas the Tethyan Basin is in deep water with a stratified ocean, making the comparison between both basins challenging. The Scotian Basin lies above the thermocline, unlike the Tethyan Basin, therefore in the Scotian Basin the water is mixed regularly thus inhibiting the conditions of absolute anoxia in some areas. In our study, the V/Ti ratio seems not to correlate with the TOC concentration, bringing us the question: did the shale deposits form under anoxic conditions in the Scotian Basin?

7.5: Climate and sediment supply

In the Tethys, climatic conditions controlled LOM deposition and preservation during the Early Cretaceous. Under arid climates with lower precipitation rates, runoff rates and nutrient fluxes, the oceans were partly stratified enhancing LOM preservation. The longer periods of arid conditions in the Late Jurassic and Early Cretaceous (early

Berriasian) allowed stable and stratified oceans to be developed. In deeper parts of these basins anoxic conditions allowing preservation of organic matter (Föllmi, 2012). Under humid climates, LOM depositions with higher nutrient fluxes and upwelling, increased primary productivity, biogeochemical weathering and development of oxygen- depleted zones, favouring preservation of organic matter. The conditions which enhanced the deposition of LOM lasted for shorter periods than LOM deposition during arid climate conditions (Föllmi, 2012).

Studies have shown that climate-sensitive clay minerals, such as kaolinite, can provide information about paleogeography and stratigraphic information on paleoclimates. Jeans (1978) demonstrated that during periods of arid climate, there is absence of kaolinite. During periods of humid climate, a higher proportion of kaolinite to illite was delivered by rivers because of greater leaching during soil development (Gould et al., 2014). Potassium, present in feldspar, mica, some clays and some evaporites, is present in illite, but not in kaolinite. Therefore, the K/Th ratio is lower during humid kaolin-rich periods than during arid kaolin-poor periods (Ruffell & Worden, 2000; Gould et al., 2014).

In our samples, K/Th ratio increases with decreasing TOC (Fig. 3). In general, where organic matter content is high, there were humid conditions, and where organic matter content is low, there was a more arid environment. At the Barremian and Early Aptian boundary, the values for TOC and K/Th ratio fluctuate until 2265 m. At this point, TOC values are low and K/Th ratio is high, indicating more arid conditions. As TOC increases, K/Th ratio decreases towards a more humid condition. TOC shows a relevant increase at a higher level in the Early Aptian, indicating humid conditions (Figs. 4 and 5).

The correlation between TOC and K/Th shows the changes in climate conditions and organic carbon content. More organic carbon was preserved during times of humid conditions and less organic carbon during arid or less humid conditions. K/Th ratio shows correlation with TOC concentration, which suggests periods of aridity when organic carbon is low and periods of humidity when organic carbon is high.

Chapter 8: Conclusion

The purpose of this thesis was to correlate and identify the OAE Selli Event in the Early Aptian of the Naskapi Member and establish the condition in which the shales were deposited; and to test the methodology of portable XRF and colour spectrophotometry, along with previous spectral gamma and ICPMS bulk geochemical data, with in-situ and powdered samples.

1. The Selli OAE was shown to occur in the Early Aptian, based on the stratigraphic position of a major interval of high TOC. The erosion surfaces recognized by MacRae (2011; "A, B, C and D in Fig. 4) from the Upper Missisauga to the base of the Naskapi Member of the Panuke B-90 well indicate hiatuses in normal marine and below normal wave base conditions on a marine shelf. These erosion surfaces preceded the presence of ammonite fossils, which are indicators of normal marine conditions and the genus is present only in the Early Aptian. The Naskapi Member shows a deepening of the marine environment towards the top, correlating with the Intra-Aptian Maximum Flooding Surface (MFS) identified by OETRA PFA.
2. The precise position of the Barremian-Aptian boundary was challenged by MacRae (2011) based on the ammonite distribution on the Naskapi Member cores, also shown in this study. We suggest that the beginning of the Aptian and the Barremian-Aptian boundary thus might have occurred deeper into the Missisauga Formation at the erosion surface "D".
3. The Total Organic Carbon (TOC) results show various peaks with high carbon concentrations from the base to the top of the Naskapi Member, indicating the

occurrences of various both, major and minor, oceanic anoxic episodes with black shale units. These black shale units show correlation with the Tethyan OAEs, which occurred during the Early Aptian. Therefore, these OAEs in the Scotian Basin seem to be Aptian, since they correlate with the Tethyan Basin and have occurrence of ammonites. These events seem to have occurred after regression conditions (lithofacies 3) followed by flooding events.

4. The sea-level changes leading to the formation of black shale episodes (e.g. Selli Event) might have been a consequence of tectonic processes in the Scotian Basin.
5. The unique occurrence of green shales in the Naskapi Member of the Panuke B-90 is still a matter of discussion. The development of anoxic conditions has been explained by two theories, either by eutrophication or by ocean water acidification. However, the lacking of bioturbation from these green shales indicates that the acidification hypothesis is the most acceptable.
6. In this study, V/Ti ratio does not correlate with TOC concentration. V/Ti ratio is not a good indicator of anoxia conditions in samples from Panuke B-90 well. On the other hand, the presence of red shales coincides with high peaks Mn/Ti ratio and high peak of parameter a*. Low K/Th ratio correlates with high TOC and the occurrence of black shales in western Europe, indicating humid environmental conditions.
7. Humid conditions occur when organic matter is high and less humid to arid conditions occur when organic matter is low. In our samples, the K/Th ratio increases with decreasing TOC. K/Th ratio is lower during humid kaolin-rich periods and higher during arid kaolin-poor periods.

8. The use of portable XRF and colour spectrophotometer in determining the environmental conditions of the studied shales, proved to be efficient. The powdered samples from core and rubble showed better correlation with the geochemical ICPMS data than the cutting powders and the in-situ core samples. The in-situ samples for both methods showed limitation such as heterogeneity and finding the right location to analyze throughout the core, which are not present in powdered samples.

References

Allen, P. (1998). Purbeck-Wealden (early Cretaceous) climates. *Proceedings of the Geologists' Association, **109,*** 197 – 236.

Arthur, M., Dean, W., & Pratt, L. (1988). Geochemical and climatic effects of increased marine organic carbon burial at the Cenomanian/Turonian boundary. *Nature, **335***, 714 – 717.

Baudin, F. (2005). A Late Hauterivian short-lived anoxic event in the Mediterranean Tethys: the "Faraoni Event". *Comptes Rendus Geoscience, **337*** (16), 28-52.

Berner, R. (1991). A model for atmospheric CO2 over Phanerozoic time. *American Journal of Science., **291***, 339 – 376.

Berner, R. A. (2003). The long-term carbon cycle, fossil fuels and atmospheric composition. *Nature, **426*** (6964), 323 – 326.

Berner, R., Lasaga, A., & Garrels, R. (1983). The carbonate-silicate geochemical cycle and its effect on atmospheric carbon dioxide ove the past 100 million years. *American Journal of Science, **283***, 641 – 683.

Bernoulli, D. (1972). North Atlantic and Mediterranean Mesozoic Facies, a comparison. In J. E. C.D. Hollister (Ed.), *Reports of the Deep Sea Drilling Project* (pp. 801 – 822). Washington, D.C: U.S. Govt. Printing Office.

Bodin, S., Vermeulen, J., Godet, A., & Follmi, K. (2006). New data on the age of the installation of Urgonian-type carbonates along the northern Tethyan margin: biostratigraphy of the Chopf Member (Helvetic Alps, eastern Switzerland). *Comptes Rendus Geoscience, **338*** (10), 727 – 733.

Bogdanova, T., & Mikhailova, I. (2004). Origin, evolution and stratigraphic significance of the superfamily Deshayesitaceae Stoyanow.1949. *Bulletin de l'Institut Royal des Sciences Naturelles de Belgique, **74***, 198 – 243.

Bowman, S., Pe-Piper, G., Piper, D., Fensome, R., & King, E. (2012). Early Cretaceous volcanism in the Scotian Basin. *Canadian Journal of Earth Science, **49,*** 1523 – 1539.

Bralower, T., Arthur, M., Leckie, R., Sliter, W., Allard, D., & Schlanger, S. (1994). Timing and paleoceanography of oceanic dysoxia/anoxia in the Late Barremian to Early Aptian (Early Cretaceous). *Paleios*, 335 – 369.

Breheret, J. G. (1988). Episodes de sédimentation riche en matière organique dans les marnes bleues d'âge aptien et albien de la partie pélagique du bassin vocontien. *Bulletin de la Société géologique de France*, ***4*** (2), 349 – 356.

Bréhéret, J. G. (1997). L'Aptien et l'Albien de la Fosse vocontienne (des bordures au bassin). Evolution de la sédimentation et enseignements sur les événements anoxiques (Doctoral dissertation).

Chamberlin, T., & Salisbury, R. (1906). The Pleistocene or Glacial Period. London: *Geology*, ***3***.

Chamley, H., 1989. Clay Minerals. In: Clay Sedimentology. *Springer-Verlag*, Berlin, 3 – 20.

Coccioni, R., Luciani, V., & Marsili, A.(2006) Cretaceous oceanic anoxic events and radially elongated chambered planktonic foraminifera: paleoecological and paleoceanographic implications. Palaeogeography, Palaeoclimatology, Palaeoecology, **235**, 66 – 92.

Cohen, K.M., Finney, S.C., & Gibbard, P.L.(2014). International Chronostratigraphic Chart. International Commission on Stratigraphy.

Debret, M., Desmet, M., Balsam, W., Copard, Y., Francus., P. & Laj, C. (2006). Spectrophotometer analysis of holocene sediments from an anoxic fjord: Saanich Inlet, British Columbia, Canada. *Marine Geology*, ***229*** (1-2), 15 – 28.

Delaney, M. L. (1998). Phosphorus accumulation in marine sediments and the oceanic phosphorus cycle. *Global Biogeochemical Cycles*, ***12*** (4), 563 – 572.

Emeis, K.-C., & Weissert, H. (2009). Tethyan-Mediterranean organic carbon-rich sediments from Mesozoic black shales to sapropelsl. *Sedimentology*, ***56***, 247 – 266.

Emmanuel, L., & Renard, M. (1993). Carbonate geochemistry (Mn,δ13C, δ18O) of the late Tithonian-Berriasian pelagic limestones of the Vocontian trough (SE France). *Bulleting de Centre de Recherches et Exploration-Production*. *Elf-Aquitaine*, ***17***, 205 – 221.

Erba, E. (2010). Calcareous nannoplankton response to surface-water acidification around Oceanic Anoxic Event 1a. *Science*, ***329*** (5990), 428 – 432.

Erba, E. & Tremolada, F. (2004). Nannofossil carbonate fluxes during the early Cretaceous: phytoplankton response to nitrification episodes, atmospheric CO_2 and anoxia. *Paleoceanography*, ***19***, PA1008, doi:10.1029/2003PA000884.

Föllmi, K. (2012). Early Cretaceous life, climate and anoxia. *Cretaceous Research, **35,*** 230 – 257.

Föllmi, K., Godet, A., Bodin, S., & Linder, P. (2006). Interactions between environmental change and shallow-water carbonate build-up along the northern Tethyan margin and their impact on the early Cretaceous carbon-isotope record. *Paleoceanography, **21**, PA4211, doi:10.1029/2006PA001313.*

Föllmi, K. B. (1996). The phosphorus cycle, phosphogenesis and marine phosphate-rich deposits. *Earth-Science Reviews, **40*** (1), 55 – 124.

Godet, A., Bodin, S., Föllmi, K. B., Vermeulen, J., Gardin, S., Fiet, N., Adatte, T., Berner, Z., Stuben, D., & van de Schootbrugge, B. (2006). Evolution of the marine stable carbon-isotope record during the early Cretaceous: a focus on the late Hauterivian and Barremian in the Tethyan realm. *Earth and Planetary Science Letters, **242,*** 254 – 271.

Gould, K. M., Piper, D. J., & Pe-Piper, G. (2011). Lateral variation in sandstone lithofacies from conventional core, Scotian Basin: Implications for reservoir quality and conductivity. *Geological Survey of Canada*, Open File 6838, doi:10.4095/288758

Gould, K. M., Piper, D. J., & Pe-Piper, G. (2012). Lateral variation in sandstone lithofacies from conventional core, Scotian Basin: Implications for reservoir quality and conductivity. *Canadian Journal of Earth Science, **49***, 1478 – 1503.

Gould, K. M., Piper, D. J., Pe-Piper, G., & MacRae, R. A. (2014). Facies, provenance and paleoclimate interpretation using spectral gamma logs: application to the Lower Cretaceous of the Scotian Basin, *Marine and Petroleum Geology*, ***57***, 445 –454.

Gröcke, D., Hesselbo, S., & Jenkyns, H. (1999). Carbon-isotope composition of lower Cretaceous fossil wood: ocean-atmosphere chemistry and relation to sea-level change. *Geology, **27***, 155 – 158.

Grotsch, J. B. (1998). Carbon-isotope stratigraphy in shallow-water carbonates:

implications for Cretaceous black-shale deposition. *Sedimentology, **45*** (4), 623 – 634.

Hallam, A., & Bradshaw, M. (1979). Bituminous shales and oolitic ironstones as indicators of transgressions and regressions. *Journal of the Geological Society of London, **136,*** 157 – 164.

Haq, B. U. (2014). Cretaceous eustasy revisited. *Global and Planetary Change, **113***, 44 – 58.

Haq, B., Hardenbol, J., & Vail, P. (1987). Chronology of fluctuating sea levels since the Triassic. *Science, **235,*** 1156 – 1167.

Heldt, M., Bachmann, M., & Lehmann, J. (2008). Microfacies, biostratigraphy, and geochemistry of the hemipelagic Barremian-Aptian in north-central Tunisia: Influence of the OEA 1a on the southern Tethys margin. *Paleogeography, Paleoclimatology, Paleoecology, **261*** (3), 246 – 260.

Helmke, J.P., Schultz, M., & Bauch, H.A. (2002). Sediment-Color record from the northeast atlantic reveals patterns of millennial-scale climate variability during the past 500,000 years. *Quaternary Research, **57***, (1), 49 – 57.

Henning, S., Weissert, H., & Bulot, L. (1999). C-isotope stratigraphy, a calibration tool between ammonite- and magnetostratigraphy: the Valanginian-Hauterivian transition. *Geologica Carpathica, **50***, 91 – 96.

Herrle, J.O., Kössler, P., Friedrich, O., Erlenkeuser, H., & Hemleben, C. (2004). High-resolution carbon isotope records of the Aptian to lower Albian from SE France and the Mazagan Plateau (DSP Site 545): a stratigraphic tool for paleoceanographic and paleobiologic reconstruction. *Earth and Planetary Science Letters, **218***, 149 – 161.

Hesselbo, S., Groecke, D., Jenkyns, H., Bjerrum, C., Farrimond, P., Morgans Bell, H., et al. (2000). Massive dissociation of gas hydrate during a Jurassic oceanic anoxic event. *Nature, **406***, 392 – 395.

Jeans, C.V. 1978. The origin of the Triassic clay assemblages of Europe with special reference to the Keuper Marl and Rhaetic of parts of England. *Philosophical Transactions of the Royal Society of London. Series A: Mathematical, Physical and Engineering Sciences, **289***, 91 – 105.

Jenkyns, H. (1980). Cretaceous anoxic events: from continents to oceans. *Journal of the Geological Society of London, **137,*** 171 – 188.

Jenkyns, H. (2003). Evidence for rapid climate change in the Mesozoic-Paleogene greenhouse world. *Philosophical Transactions of the Royal Society of London, **361,*** 1885 – 1916.

Kemper, E., & Zimmerle, W. (1982). Das Ablagerungsmilieu zur Zeit des späten Apt und frühen Alb im niedersächsischen Becken. *Geologisches Jahrbuch A, **65***, 655 – 660.

Larson, R. L. (1991). Geological consequences of superplumes. *Geology, **19*** (10), 963 – 966.

Larson, R., & Erba, E. (1999). Onset of the mid-Cretaceous greenhouse in the Barremian-Aptian: igneous events and the biological, sedimentary, and geochemical responses. *Paleoceanography, **14,*** 663 – 678.

MacRae, R. (2011). Age and paleoenvironmental significance of macrofossils and sedimentary facies from the Alma K-85 and Panuke B-90 wells, Early Cretaceous, Upper Missisauga and Logan Canyon formations, offshore Nova Scotia. Unpublished report to OETR.

Masse, J., & Fenerci-Masse, M. (2013). Drowning events, development and demise of carbonate platforms and controlling factors: The Late Barremian-Early Aptian record of Southeast France. *Sedimentary Geology*, ***298,*** 1532 – 1540.

Mutterlose, J., Malkoc, M., Schouten, S., Sinnighe Damste, J., & Forster, A. (2010). TEX 86 and stable 18O paleothermometry of early Cretaceous sediments: Implications for belemnite ecology and paleotemperature proxy application. *Earth and Planetary Science Letters*, ***298*** (3), 286 – 298.

Mutterlose, J., Pauly, S., & Steuber, T. (2009). Temperature controlled deposition of early Cretaceous (Barremian-early Aptian) blackshales in an epicontinental sea. *Paleogeography, Paleoclimatology, Paleocology, **273*** (3), 330 – 345.

Myers, K. (1987). Onshore Outcrop Gamma-Ray Spectroscopy as a Tool in Sedimentological Studies. *Unpubl. Ph.D Thesis, Univ. London*.

Nederbragt, A. J., Dunbar, R. B., Osborn, A. T., Palmer, A., Thurow, J. W., & Wagner, T. (2006). Sediment colour analysis from digital images and correlation with sediment composition. *Geological Society, London, Special Publications*, ***267*** (1), 113 –128.

Nunn, E., & Price, E. (2010). Late Jurassic (Kimmeridgian-Tithonian) stable isotopes and Mg/Ca ratios: New paleoclimate data from Helmsdale, northeast Scotland. *Paleogeography, Paleoclimatology, Paleocology.*, ***292,*** 325 – 335.

Ogg, J., Agterberg, F., & Gradstein, F. (2004). The Cretaceous Period. In F. Gradstein, J. Ogg, & A. Smith, *A Geological Time Scale* (pp. 344 – 383). Cambridge University Press.

OETR (Offshore Energy Technical Research Association). 2011. Play Fairway Analysis Atlas-Offshore Nova Scotia. Nova Scotia Department of Energy Report 88-11-

0004-01, 349 p. Available from: http://www.novascotiaoffshore.com/analysis. (Assessed Aug 2014).

Parkinson, D. N. (1996). Gamma-ray spectrometry as a tool for stratigraphical interpretation: examples from the western European Lower Jurassic. *Geological Society, London, Special Publications, **103*** (1), 231 – 255.

Parrish, J. (1982). Upwelling and petroleum source beds, with reference to Paleozoic. *AAPG Bulletin, **66***, 750 – 774.

Parrish, J., & Curtis, R. (1982). Atmospheric circulation, upwelling, and organic-rich rocks in the Mesozoic and Cenozoic eras. *Paleogeography, Paleoclimatology, Paleocology., **40***, 31 – 66.

Pedersen, T., & Calvert, S. (1990). Anoxia vs. productivity. What controls the formation of organic-carbon-rich sediments and sedimentary rocks? *The American Association of Petroleum Geologists Bulletin, **74***, 454 – 466.

Pe-Piper, G. &. (2014). The effects of strike-slip motion along the Cobequid-Chedabucto-southwest Grand Banks fault system on the Cretaceous-Tertiary evolution of Atlantic Canada. *Canadian Journal of Earth Sciences, **41*** (7), 799 – 808.

Peropadre, C., Liesa, C. L., & Meléndez, N. (2013). High-frequency, moderate to high-amplitude sea-level oscillations during the late Early Aptian: Insights into the Mid-Aptian event (Galve sub-basin, Spain). Sedimentary Geology, **294**, 233 – 250.

Piper, D., Bowman, S., Pe-Piper, G., & MacRae, R. (2011). The ups and downs of Guysborough County- the mid Cretaceous Naskapi Member in the Scotian Basin: eustacy or tectonics? *Atlantic Geology, **47***, 37 – 38.

Piper, D.J.W., Pe-Piper, G., Hundert, T., & Venugopal, D. (2007). The Lower Cretaceous Chaswood Formation in southern New Brunswick: provenance and tectonics. *Canadian Journal of Earth Sciences, **44***, 665 – 677.

Pitman, W. I. (1978). Relationship between eustacy and stratigraphic sequences of passive margins. Geological Society of America Bulletin, ***89***, 1389 – 1403.

Purcell, L., Rashid, M., & Hardy, I. (1979). Geochemical Characteristics of Sedimentary Rocks in Scotian Basin. *The American Association of Petroleum Geologists Bulletin, **63***, 87 – 105.

Roth, S., & Reijmer, J.J.G. (2005). Holocene millennial to centennial carbonate cyclicity recorded in slope sediments of the Great Bahama bank and its climatic implications. *Sedimentology, **52***, (1), 161 – 181.

Ruffell, A., & Batten, D. (1990). The Barremian-Aptian arid phase in western Europe. *Paleogeography, Paleoclimatology, Paleocology.*, ***80***, 197 – 212.

Ruffell, A., & Worden, R. (2000). Paleoclimate analysis using spectral gamma-ray data from the Aptian (Cretaceous) of southern England and southern France. *Paleogeography, Paleoclimatology, Paleoecology*, ***155,*** 265 – 283.

Ruffell, A., McKinley, J., & Worden, R. (2002). Comparison of clay mineral stratigraphy to other proxy paleoclimate indicators in the Mesozoic of NW Europe. *Philosophical Transactions of the Royal Society of London. Series A: Mathematical, Physical and Engineering Sciences, **360***, 675 – 693.

Ryan, W., & Cita, M. (1977). Ignorance concerning episodes of oceanwide stagnation. *Marine Geology, **23,*** 197 – 215.

Scotchman, I. (1989). Diagenesis of the Kimmeridge Clay Formation, onshore UK. *Journal of the Geological Society London, **146***, 285 – 303.

Skelton, P. W.& Gili,E. (2012). Rudists and carbonate platforms in the Aptian: a case study on biotic interactions with ocean chemistry and climate. *Sedimentology, **59*** (1), 81 – 117.

Sliter, W. V. (1989). Aptian anoxia in the Pacific Basin. *Geology*, **17**(10), 909 – 912.

Sprovieri, M., Coccioni, R., Lirer, F., Pelosi, N., & Lozar, F. (2006). Orbital tuning of a lower Cretaceous composite record (Maiolica Formation, central Italy). *Paleoceanography, **21,*** PA4212**.**

Svensen, H., Planke, S., Malthe-Sorenssen, A., Jamtveit, B., Myklebust, R., Eidem, T., et al. (2004). Release of methane from a volcanic basin as a mechanism for initial Eocene global warming. *Nature, **429***, 542 – 545.

Tejada, M., Suzuki, K., Kuroda, J., Coccioni, R., Mahoney, J., Ohkouchi, N., et al. (2009). Ontong Java Plateau eruption as a trigger for the early Aptian oceanic event. *Geology*, ***37*** (9), 855 – 858.

Vahrenkamp, V.E. (1996). Carbon isotope stratigraphy of the Upper Kharib and Shuaiba Formations: implications for the early Cretaceous evolution of the Arabian Gulf region. *The American Association of Petroleum Geologists Bulletin, **80***, 647 – 662.

Van de Schootbrugge, B., Föllmi, K.B., Bulot, L.G., & Burns, S., J. (2000). Paleoceanographic changes during the Early Cretaceous (Valaginian-Hauterivian): evidence from oxygen and carbon stable isotopes. *Earth and Planetary Science Letters, **181,*** 15 – 31.

Wade, J., & MacLean, B. (1990). The geology of the southeastern margin of Canada. In G. S. Canada, & M. K. Williams (Ed.), *Geology of the Continental Margin of Eastern Canada* (pp. 167 – 238). Ottowa, Canada.

Wang, C. H. (2011). Cretaceous oceanic red beds as possible consequence of oceanic anoxic events. *Sedimentary Geology*, ***235*** (1), 27 – 37.

Weissert, H. (1981). The Environment of Deposition of Black Shales in the Early Cretaceous: an Ongoing Controversy.*The Society of Economic Paleontologists and Mineralogist, **32,*** 547 –560.

Weissert, H. (1989). C-isotope stratigraphy, a monitor of paleoenvironmental change: a case study from the Early Cretaceous. *Surveys in Geophysics, **10***, 1 – 61.

Weissert, H. (2000). Global change- deciphering methane's fingerprint. *Nature, **406,*** 356 – 357.

Weissert, H., & Erba, E. (2004). Volcanism, CO2 and paleoclimate: a Late Jurassic-Early Cretaceous carbon and oxygen isotope record. *Journal of the Geological Society, **161,*** 695 – 702.

Weissert, H., McKenzie, J., & Hochuli, P. (1979). Cyclic anoxic events in the early Cretaceous Tethys ocean. *Geology, **7,*** 147 – 151.

Yilmaz, I.Ö, Vennemann, T., Altiner, D., & Satir, M., (2004). Stable isotope evidence for meter-scale sea level changes in lower Cretaceous inner platform and pelagic carbonate successions of Turkey. *Geologica Carpathica*, ***55***, 19 – 36.

Zhang, Y., Pe-Piper, G., & Piper, D. J. W.(2014). Sediment geochemistry as a provenance indicator: unravelling the cryptic signatures of polycyclic sources, climate change, tectonism and volcanism. *Sedimentology*, ***61***, 383 – 410.

Appendix 1: Figure A1- Biplots of powdered samples and previous ICPMS geochemical analyses from the same core locations.

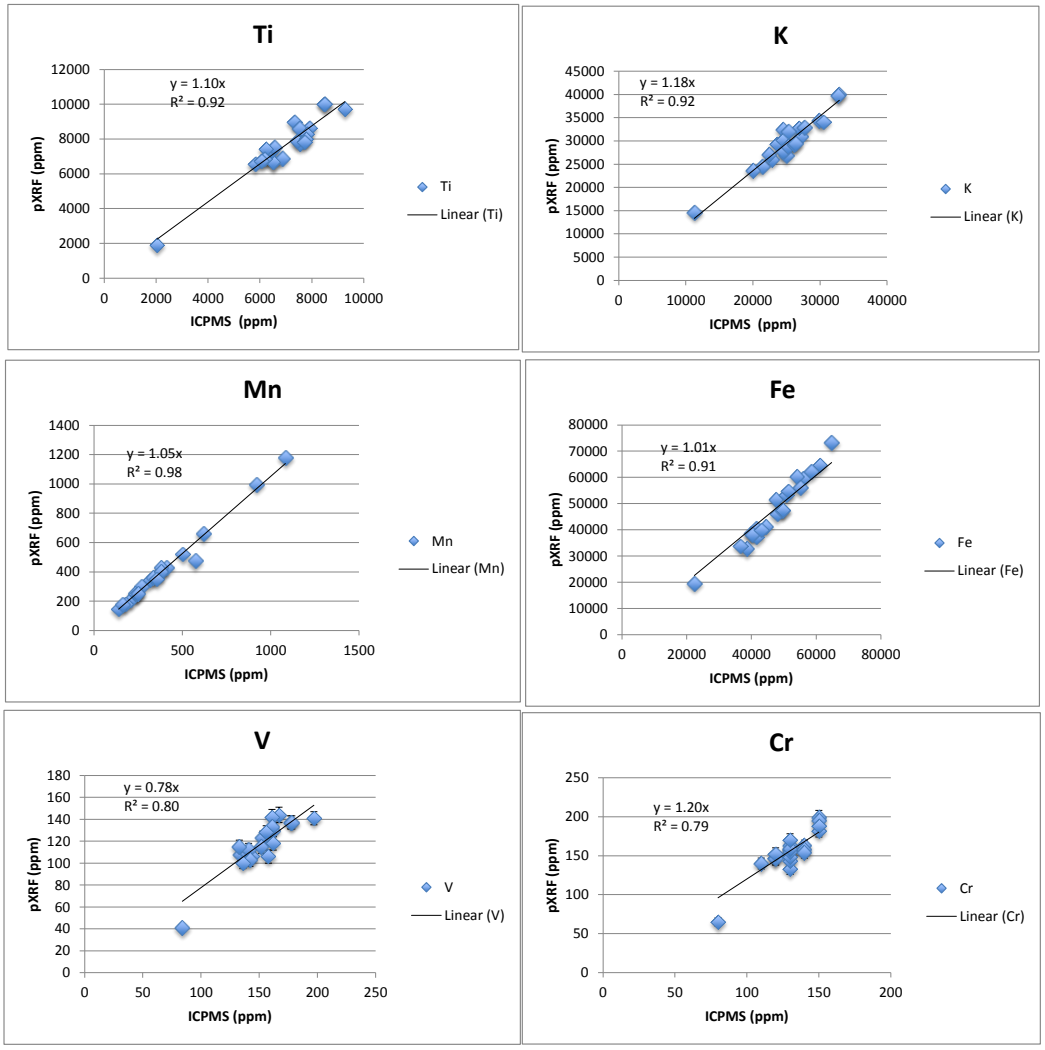

Notes: the error bars for most elements, with exception of Th, are the size of the symbol.

Figure A1- continued.

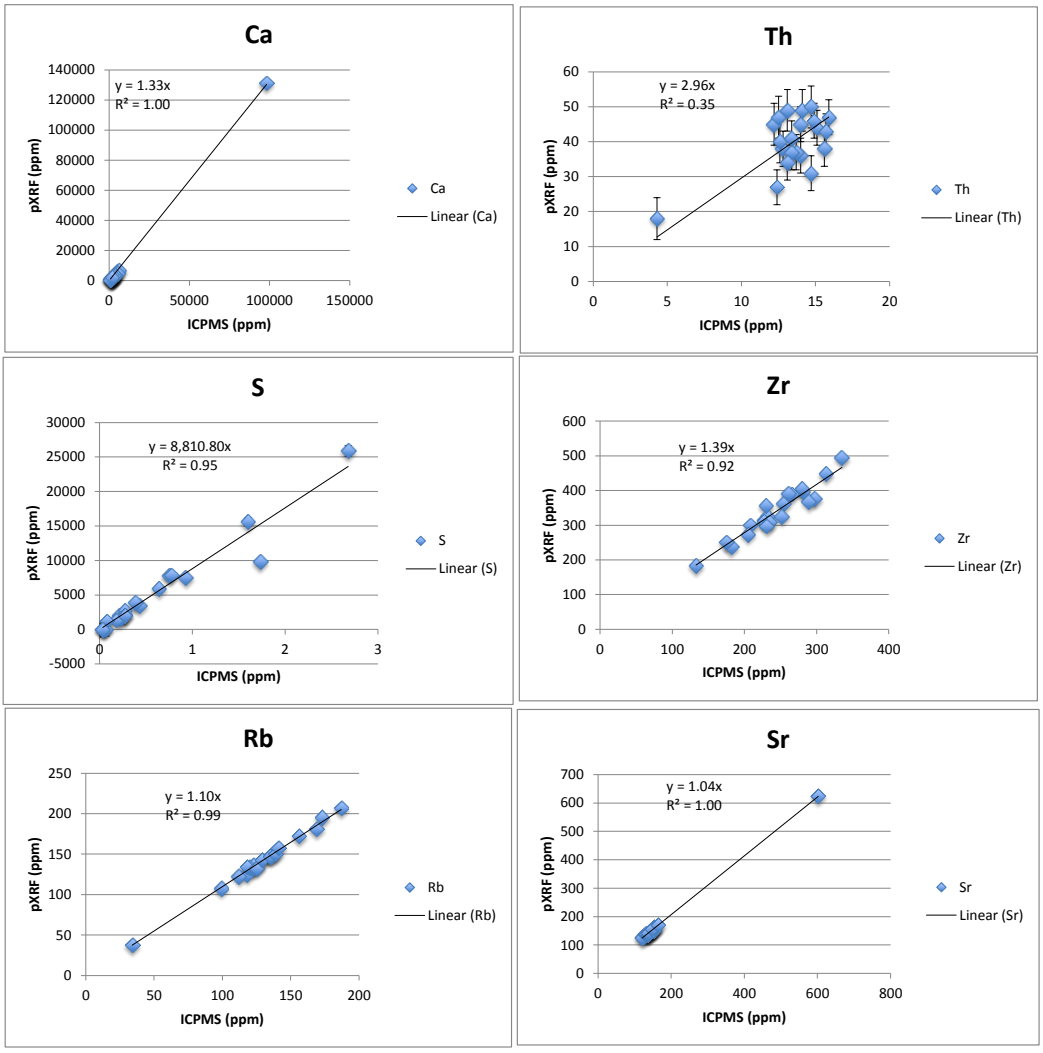

Appendix 1: Figure A2- Biplots of in-situ core samples and ICPMS geochemical samples from the same core locations

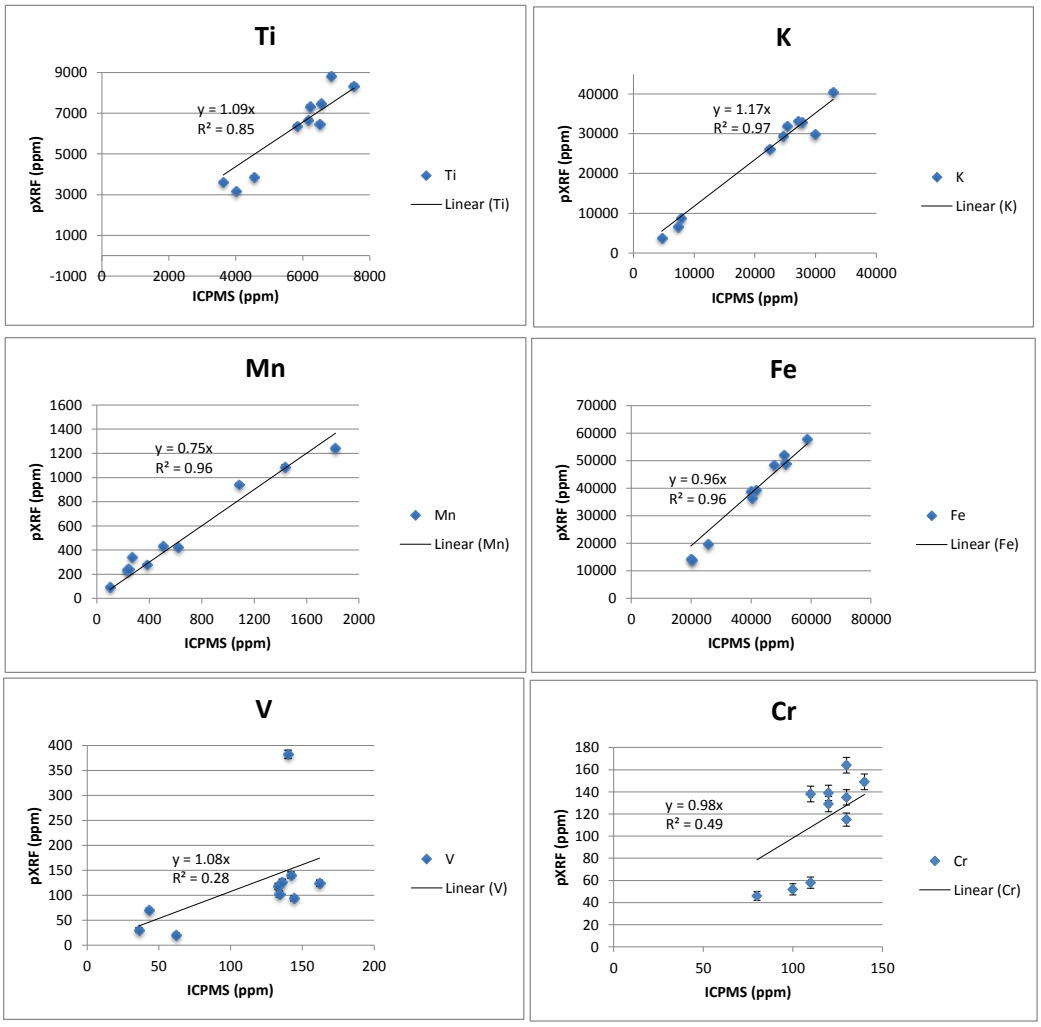

Notes: the error bars for most elements, with exception of Th, are the size of the symbol.

Figure A2- continued

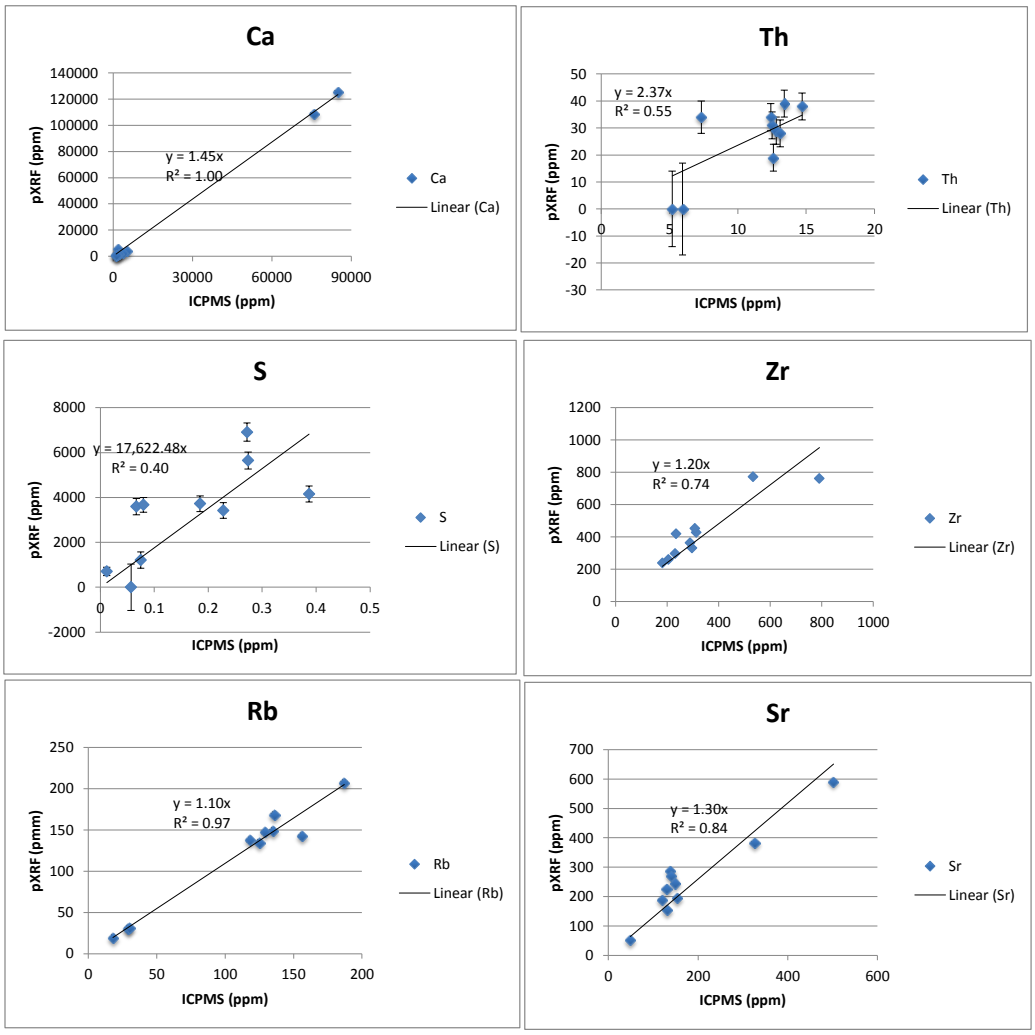

Appendix 2: Table A1- Comparison between in-situ XRF on powdered samples and previous ICPMS geochemical analyses from the core locations.

Sample	A-52 2072.90			A-52 2074.72			A-52 2123.52			A-52 2138.22			A-52 2159.63		
Lithology	Mudstone			Mudstone			Mudstone			Mudstone			Mudstone		
Type	ICMPS	pXRF	SD	ICMPS	pXRF	SD	ICMPS	pXRF	SD	ICMPS	pXRF	SD	ICMPS	pXRF	SD
Si	267955	-	-	244157	-	-	248365	-	-	239949	-	-	297785	-	-
Al	82004	-	-	87020	-	-	79762	-	-	70870	-	-	11020	-	-
Fe	41686	37107	143	48051	45955	180	49520	47297	185	64838	73343	286	22312	19527	92
Mn	410	431	9	372	389	10	318	343	9	333	359	10	573	474	9
Mg	8081	-	-	8443	-	-	9348	-	-	10313	-	-	2895	-	-
Ca	2001	1713	61	1787	1812	66	1787	1584	64	3717	4235	94	98141	130968	1131
Na	5341	-	-	5490	-	-	6157	-	-	6454	-	-	2671	-	-
K	21418	24546	280	20007	23644	289	22829	26055	308	24489	32418	382	11290	14636	206
Ti	7546	7738	79	7432	7887	86	7905	8645	92	8499	10017	109	2038	1913	32
P	305	<LOD	2030	218	<LOD	2243	305	<LOD	2409	1091	<LOD	2904	131	<LOD	4739
Sc	21	-	-	21	-	-	21	-	-	19	-	-	5	-	-
Be	3	-	-	3	-	-	3	-	-	3	-	-	1	-	-
V	153	123	6	158	106	6	162	130	6	167	144	7	84	41	3
Cr	140	163	7	140	158	7	150	182	8	150	199	9	80	65	5
Co	26	16.9	0.7	25	21	0.8	27	20.5	0.8	25	30.9	1	3	7.4	0.5
Ni	86	<LOD	20	89	<LOD	21	96	32	7	98	<LOD	25	13	<LOD	18
Cu	33	53	3	32	40	3	30	41	3	28	34	3	9	14	3
Zn	86	146	3	83	75	2	88	83	3	106	91	3	27	16	1.8
Cd	< 0.5	-	-	< 0.5	-	-	< 0.5	-	-	< 0.5	-	-	< 0.5	-	-
S	0.214	2062	289	0.432	3431	354	0.753	7812	449	1.6	15594	631	0.041	<LOD	1072
Ga	28	-	-	30	-	-	28	-	-	26	-	-	5	-	-
Ge	1.8	-	-	1.6	-	-	1.5	-	-	1.4	-	-	1.1	-	-
As	8	16.4	1.2	9	13.2	1.2	15	17.9	1.2	15	19.8	1.3	5	3.7	0.9
Rb	125	134.8	1.4	118	125	1.4	122	132	1.5	112	122.1	1.5	34	37.8	1
Sr	124	127.5	1.3	136	139	1.4	131	137	1.4	154	162.1	1.6	602	625	3
Y	31.9	-	-	31.5	-	-	32	-	-	39.4	-	-	6.2	-	-
Zr	228	315	2	232	325	3	254	362	3	281	397	3	133	183	2
Nb	28.1	-	-	28	-	-	33	-	-	35.5	-	-	7.6	-	-
Mo	4	5.6	1.2	< 2	<LOD	3.8	< 2	<LOD	3.8	< 2	<LOD	4.1	< 2	<LOD	3.8
Ag	0.3	<LOD	16	< 0.3	<LOD	17	0.4	<LOD	17	0.4	<LOD	18	< 0.3	<LOD	18
In	< 0.1	-	-	< 0.1	-	-	< 0.1	-	-	< 0.1	-	-	< 0.1	-	-
Sn	7	<LOD	27	4	<LOD	29	4	<LOD	29	3	<LOD	31	2	<LOD	30
Sb	1.3	<LOD	29	0.4	<LOD	31	0.4	<LOD	31	0.4	<LOD	32	< 0.2	<LOD	31
Cs	8.3	-	-	8.1	-	-	7.8	-	-	6.5	-	-	0.7	-	-
Ba	390	-	-	359	-	-	380	-	-	386	-	-	292	-	-
La	51.1	-	-	53.1	-	-	52.7	-	-	60.5	-	-	13.3	-	-
Ce	106	-	-	110	-	-	110	-	-	128	-	-	35.8	-	-
Pr	11.7	-	-	12.4	-	-	12.2	-	-	14.6	-	-	3.57	-	-
Nd	42.9	-	-	45.2	-	-	44	-	-	53.4	-	-	13.3	-	-
Sm	8.16	-	-	8.54	-	-	8.17	-	-	10.3	-	-	2.56	-	-
Eu	1.68	-	-	1.73	-	-	1.67	-	-	2.18	-	-	0.518	-	-
Gd	6.4	-	-	6.52	-	-	6.22	-	-	8.27	-	-	1.85	-	-
Tb	1.02	-	-	1.03	-	-	1.01	-	-	1.29	-	-	0.26	-	-
Dy	5.98	-	-	5.85	-	-	6.01	-	-	7.37	-	-	1.38	-	-
Ho	1.17	-	-	1.14	-	-	1.21	-	-	1.42	-	-	0.25	-	-
Er	3.36	-	-	3.29	-	-	3.44	-	-	4.02	-	-	0.7	-	-
Tm	0.506	-	-	0.491	-	-	0.527	-	-	0.594	-	-	0.103	-	-
Yb	3.49	-	-	3.42	-	-	3.53	-	-	3.95	-	-	0.7	-	-
Lu	0.584	-	-	0.6	-	-	0.6	-	-	0.643	-	-	0.118	-	-
Hf	6.4	-	-	6.5	-	-	6.9	-	-	7.4	-	-	3.5	-	-
Ta	1.71	-	-	1.77	-	-	1.98	-	-	2.23	-	-	0.52	-	-
W	2.5	<LOD	11	2	<LOD	11	1.8	<LOD	11	2.1	<LOD	12	< 0.5	<LOD	11
Tl	0.48	-	-	0.48	-	-	0.51	-	-	0.48	-	-	0.07	-	-
Pb	18	30.6	1.6	19	26.4	1.6	13	24.9	1.7	18	29	1.9	10	12.7	1.4
Bi	< 0.1	<LOD	13	< 0.1	<LOD	14	< 0.1	<LOD	14	< 0.1	<LOD	15	< 0.1	<LOD	14
Th	15.1	44	5	15.6	38	5	14.9	46	5	14.1	49	6	4.3	18	6
U	3.22	<LOD	4.5	3.24	<LOD	4.7	3.29	<LOD	4.8	3.68	<LOD	5.1	0.63	<LOD	5.6
Cl	-	1221	118	-	1170	128	-	970	126	-	1575	154	-	2609	144
Se	-	<LOD	1.4	-	<LOD	1.4	-	<LOD	1.5	-	<LOD	1.6	-	<LOD	1.4
Cd	-	<LOD	18	-	<LOD	19	-	<LOD	19	-	<LOD	20	-	<LOD	19
Hg	-	<LOD	4.3	-	<LOD	4.6	-	7.1	1.6	-	5.3	1.7	-	<LOD	4.5

Notes: 1. All values are in ppm, 2. SD= standard deviation, 3. LOD= limit of detection

Table A1- continued.

Sample	A-52 2418.75			A-52 2597.05			B-90 2097.27			B-90 2235.37			B-90 2241.57		
Lithology	Mudstone			Mudstone			Mudstone			Mudstone			Mudstone		
Type	ICMPS	pXRF	SD	ICMPS	pXRF	SD	ICMPS	pXRF	SD	ICMPS	pXRF	SD	ICMPS	pXRF	SD
Si	229850	-	-	263186	-	-	223257	-	-	278101	-	-	285114	-	-
Al	62852	-	-	85310	-	-	74594	-	-	62624	-	-	68210	-	-
Fe	61271	64645	256	44554	41304	160	56025	59480	225	47632	51436	202	39938	38472	151
Mn	240	253	9	209	209	8	379	429	10	503	521	11	271	299	8
Mg	10674	-	-	9227	-	-	13147	-	-	8805	-	-	10614	-	-
Ca	5575	6098	108	1001	629	55	6219	6781	112	5075	4699	93	1930	1507	64
Na	7270	-	-	4674	-	-	6751	-	-	6973	-	-	7048	-	-
K	23576	29310	350	24987	26916	307	24489	30218	349	22414	27092	322	27146	30993	341
Ti	8493	10035	108	6527	6661	73	7324	8970	96	7528	8595	93	6857	6883	74
P	1135	<LOD	2953	305	<LOD	2112	960	<LOD	2671	829	<LOD	2452	393	<LOD	2131
Sc	16	-	-	21	-	-	20	-	-	17	-	-	19	-	-
Be	2	-	-	3	-	-	4	-	-	3	-	-	3	-	-
V	161	142	7	141	109	5	197	141	6	134	108	6	140	109	5
Cr	130	158	8	130	158	7	150	195	8	110	140	7	130	133	7
Co	20	27.3	0.9	20	18.5	0.7	20	25.6	0.9	25	22	0.8	23	16.6	0.7
Ni	85	<LOD	23	73	<LOD	20	93	<LOD	22	71	<LOD	22	69	<LOD	20
Cu	22	26	3	38	38	3	31	33	3	29	36	3	38	38	3
Zn	99	86	3	77	73	2	97	77	2	105	87	3	119	89	3
Cd	< 0.5	-	-	< 0.5	-	-	< 0.5	-	-	< 0.5	-	-	< 0.5	-	-
S	2.68	25881	777	0.269	2170	302	0.772	7867	470	0.387	3858	375	0.272	2720	315
Ga	23	-	-	28	-	-	27	-	-	22	-	-	23	-	-
Ge	0.9	-	-	1.9	-	-	3.2	-	-	1.6	-	-	1.9	-	-
As	21	22.9	1.3	7	10.5	1.1	17	14.6	1.1	9	11.3	1.1	9	10.3	1.1
Rb	99	107.6	1.4	123	136.9	1.5	120	133.5	1.5	118	134.2	1.5	136	147.1	1.5
Sr	153	150.8	1.5	139	142.9	1.4	147	155	1.4	154	156.9	1.5	120	125.6	1.3
Y	30.9	-	-	31.4	-	-	30.8	-	-	31.7	-	-	29.2	-	-
Zr	266	390	3	209	300	2	227	312	3	313	448	3	297	376	3
Nb	41.3	-	-	22.1	-	-	40	-	-	33.1	-	-	26.3	-	-
Mo	< 2	<LOD	4	< 2	<LOD	3.7	< 2	<LOD	3.7	< 2	<LOD	4	< 2	<LOD	3.7
Ag	0.5	<LOD	18	< 0.3	<LOD	17	0.4	<LOD	17	< 0.3	<LOD	18	< 0.3	<LOD	17
In	< 0.1	-	-	< 0.1	-	-	< 0.1	-	-	< 0.1	-	-	< 0.1	-	-
Sn	2	<LOD	30	4	<LOD	28	4	<LOD	29	3	<LOD	30	2	<LOD	28
Sb	0.5	<LOD	32	0.7	<LOD	30	0.8	<LOD	31	< 0.2	<LOD	31	0.3	<LOD	30
Cs	5.3	-	-	7.7	-	-	8.3	-	-	6.8	-	-	6.7	-	-
Ba	372	-	-	337	-	-	366	-	-	333	-	-	343	-	-
La	57.2	-	-	52.1	-	-	58.2	-	-	49	-	-	47.2	-	-
Ce	122	-	-	105	-	-	120	-	-	104	-	-	93.8	-	-
Pr	13.7	-	-	12	-	-	13.5	-	-	11.1	-	-	10.2	-	-
Nd	49.4	-	-	43.3	-	-	48.6	-	-	42.9	-	-	35.9	-	-
Sm	9.1	-	-	8.08	-	-	8.99	-	-	8.29	-	-	6.19	-	-
Eu	1.99	-	-	1.73	-	-	1.9	-	-	1.82	-	-	1.28	-	-
Gd	7.36	-	-	6.43	-	-	7.33	-	-	6.74	-	-	4.93	-	-
Tb	1.1	-	-	1.01	-	-	1.12	-	-	1.12	-	-	0.85	-	-
Dy	6.15	-	-	5.85	-	-	6.31	-	-	6.33	-	-	5.2	-	-
Ho	1.18	-	-	1.12	-	-	1.21	-	-	1.19	-	-	1.07	-	-
Er	3.31	-	-	3.18	-	-	3.52	-	-	3.43	-	-	3.25	-	-
Tm	0.496	-	-	0.472	-	-	0.543	-	-	0.536	-	-	0.527	-	-
Yb	3.24	-	-	3.2	-	-	3.4	-	-	3.49	-	-	3.5	-	-
Lu	0.508	-	-	0.525	-	-	0.493	-	-	0.485	-	-	0.499	-	-
Hf	6.2	-	-	5.8	-	-	6.2	-	-	8.5	-	-	7.8	-	-
Ta	2.49	-	-	1.35	-	-	2.25	-	-	2.06	-	-	1.54	-	-
W	1.6	<LOD	12	1.7	<LOD	10	2.4	12	4	1.6	<LOD	11	< 0.5	<LOD	11
Tl	0.46	-	-	0.47	-	-	0.41	-	-	0.44	-	-	0.48	-	-
Pb	17	25.4	1.8	16	26.3	1.6	15	19.9	1.6	22	23.4	1.7	18	20.2	1.5
Bi	< 0.1	<LOD	15	< 0.1	<LOD	14	0.3	<LOD	14	< 0.1	<LOD	14	< 0.1	<LOD	13
Th	12.2	45	6	14	36	5	13.7	37	5	12.5	47	6	12.4	27	5
U	3.42	<LOD	4.9	3	<LOD	4.6	2.95	<LOD	4.7	3.01	<LOD	4.9	2.89	<LOD	4.6
Cl	-	1981	158	-	622	110	-	1029	134	-	781	126	-	532	108
Se	-	<LOD	1.6	-	<LOD	1.4	-	<LOD	1.5	-	<LOD	1.5	-	<LOD	1.4
Cd	-	<LOD	20	-	<LOD	18	-	<LOD	19	-	<LOD	19	-	<LOD	19
Hg	-	<LOD	5	-	<LOD	4.4	-	<LOD	4.8	-	<LOD	4.8	-	6.2	1.6

Table A1- continued.

Sample	B-90 2245.78			B-90 2247.20			B-90 2255.49			B-90 2256.56			B-90 2263.94		
Lithology	Mudstone			Mudstone			Mudstone			Mudstone			Mudstone		
Type	ICMPS	pXRF	SD	ICMPS	pXRF	SD	ICMPS	pXRF	SD	ICMPS	pXRF	SD	ICMPS	pXRF	SD
Si	271368	-	-	242053	-	-	261784	-	-	266038	-	-	255846	-	-
Al	72922	-	-	84436	-	-	73340	-	-	70908	-	-	75506	-	-
Fe	41686	40467	158	50919	53292	207	54136	60282	240	58683	62173	241	51409	54760	215
Mn	379	400	9	232	249	9	922	996	16	1084	1177	17	620	659	12
Mg	11338	-	-	11820	-	-	12544	-	-	12062	-	-	11760	-	-
Ca	2144	1809	68	1573	1347	70	3217	3031	84	3645	3518	86	2359	2197	75
Na	6973	-	-	6009	-	-	6232	-	-	6232	-	-	5861	-	-
K	29885	34312	371	32874	40034	439	26897	32763	386	25320	32029	373	27727	32799	377
Ti	6503	6664	73	5826	6559	76	6461	7342	85	6551	7507	85	6221	7413	84
P	305	<LOD	2188	218	<LOD	2453	524	<LOD	2639	567	<LOD	2656	480	<LOD	2404
Sc	19	-	-	22	-	-	20	-	-	21	-	-	22	-	-
Be	3	-	-	3	-	-	3	-	-	3	-	-	3	-	-
V	144	106	5	162	118	6	141	112	6	133	115	6	142	103	6
Cr	130	143	7	130	148	8	120	147	8	120	146	8	120	152	23.6
Co	21	18.5	0.7	27	22.6	0.8	30	25.5	0.9	29	24.2	0.9	27	23.6	0.8
Ni	75	<LOD	21	95	<LOD	22	82	<LOD	23	79	<LOD	23	80	<LOD	22
Cu	34	36	3	39	45	3	41	51	3	44	52	3	39	44	3
Zn	91	74	2	103	89	3	94	88	3	95	72	3	99	91	3
Cd	< 0.5	-	-	< 0.5	-	-	< 0.5	-	-	< 0.5	-	-	< 0.5	-	-
S	0.274	2002	302	0.228	1548	320	0.039	<LOD	939	0.067	<LOD	939	0.185	1350	317
Ga	24	-	-	28	-	-	25	-	-	24	-	-	26	-	-
Ge	1.9	-	-	2	-	-	2	-	-	1.9	-	-	1.9	-	-
As	9	11	1.1	13	12.6	1.1	8	9.1	1.2	10	10	1.1	8	8.7	1.1
Rb	156	172	1.6	187	207	1.9	129	142.3	1.6	125	132.2	1.5	135	147.9	1.6
Sr	130	139.4	1.4	139	146.2	1.4	147	151.8	1.5	141	144.4	1.4	149	152.2	1.5
Y	26.5	-	-	24.7	-	-	35.7	-	-	37.5	-	-	31.7	-	-
Zr	235	309	3	182	237	2	252	325	3	289	368	3	231	297	3
Nb	24.8	-	-	22.8	-	-	25.3	-	-	24.8	-	-	26.1	-	-
Mo	< 2	<LOD	3.7	< 2	<LOD	3.8	< 2	<LOD	4	< 2	<LOD	3.9	< 2	<LOD	3.9
Ag	< 0.3	<LOD	17	< 0.3	<LOD	18	0.4	<LOD	18	0.3	<LOD	18	0.3	<LOD	18
In	< 0.1	-	-	< 0.1	-	-	< 0.1	-	-	< 0.1	-	-	< 0.1	-	-
Sn	3	<LOD	29	3	<LOD	29	3	<LOD	30	3	<LOD	30	3	<LOD	30
Sb	0.5	<LOD	30	0.6	<LOD	31	0.9	<LOD	32	0.8	<LOD	32	0.7	<LOD	32
Cs	7.9	-	-	10.7	-	-	7	-	-	6.6	-	-	7.5	-	-
Ba	359	-	-	388	-	-	396	-	-	353	-	-	363	-	-
La	47.4	-	-	50.1	-	-	53.1	-	-	50.7	-	-	53.3	-	-
Ce	93.7	-	-	102	-	-	108	-	-	102	-	-	106	-	-
Pr	10.4	-	-	11.6	-	-	12.5	-	-	11.8	-	-	12.4	-	-
Nd	36.3	-	-	41.9	-	-	45.5	-	-	43.9	-	-	45	-	-
Sm	6.18	-	-	7.34	-	-	8.42	-	-	8.27	-	-	8.17	-	-
Eu	1.28	-	-	1.49	-	-	1.74	-	-	1.81	-	-	1.74	-	-
Gd	4.77	-	-	5.12	-	-	6.73	-	-	6.81	-	-	6.51	-	-
Tb	0.8	-	-	0.85	-	-	1.13	-	-	1.18	-	-	1.08	-	-
Dy	4.84	-	-	4.88	-	-	6.65	-	-	6.76	-	-	6.12	-	-
Ho	0.98	-	-	0.95	-	-	1.28	-	-	1.31	-	-	1.17	-	-
Er	2.99	-	-	2.83	-	-	3.84	-	-	3.89	-	-	3.49	-	-
Tm	0.497	-	-	0.464	-	-	0.604	-	-	0.62	-	-	0.552	-	-
Yb	3.26	-	-	3.02	-	-	3.84	-	-	3.99	-	-	3.56	-	-
Lu	0.464	-	-	0.435	-	-	0.556	-	-	0.567	-	-	0.507	-	-
Hf	6.4	-	-	4.9	-	-	6.9	-	-	7.5	-	-	6.1	-	-
Ta	1.45	-	-	1.36	-	-	1.5	-	-	1.46	-	-	1.49	-	-
W	0.8	<LOD	11	< 0.5	<LOD	12	< 0.5	<LOD	12	< 0.5	<LOD	11	0.7	13	4
Tl	0.54	-	-	0.69	-	-	0.52	-	-	0.47	-	-	0.5	-	-
Pb	17	18.5	1.5	23	21.2	1.6	18	21.3	1.7	17	21	1.7	15	23.1	1.7
Bi	0.1	<LOD	14	0.2	<LOD	14	0.2	<LOD	15	0.2	<LOD	14	0.2	<LOD	14
Th	12.8	38	5	13.4	37	5	13.1	49	6	12.6	40	6	13.1	34	5
U	2.75	<LOD	4.7	2.58	<LOD	5	3.29	<LOD	5	3.23	<LOD	4.8	2.95	<LOD	4.9
Cl	-	701	113	-	461	119	-	923	133	-	1100	135	-	663	124
Se	-	<LOD	1.4	-	<LOD	1.5	-	<LOD	1.5	-	<LOD	1.4	-	<LOD	1.5
Cd	-	<LOD	19	-	<LOD	19	-	<LOD	20	-	<LOD	20	-	<LOD	20
Hg	-	<LOD	4.5	-	<LOD	4.8	-	<LOD	4.9	-	<LOD	4.7	-	<LOD	4.8

Table A1- continued.

Sample	B-90 2278.21			B-90 2319.18			B-90 2347.50			B-90 2402.33			B-90 2417.48		
Lithology	Mudstone			Mudstone			Mudstone			Mudstone			Mudstone		
Type	ICMPS	pXRF	SD	ICMPS	pXRF	SD	ICMPS	pXRF	SD	ICMPS	pXRF	SD	ICMPS	pXRF	SD
Si	244998	-	-	261924	-	-	257108	-	-	250702	-	-	257248	-	-
Al	85234	-	-	77862	-	-	76722	-	-	81738	-	-	76532	-	-
Fe	40218	38347	149	49730	47615	188	43015	39812	160	38539	32734	128	36650	33765	130
Mn	240	246	8	248	249	8	178	180	8	139	144	7	163	176	7
Mg	9287	-	-	10011	-	-	11458	-	-	9951	-	-	9468	-	-
Ca	1072	706	55	1787	1553	66	1430	1160	63	786	437	55	2716	2441	69
Na	4674	-	-	6009	-	-	7048	-	-	4896	-	-	4525	-	-
K	24572	27654	312	25237	28854	337	26150	29210	340	30549	34079	357	26316	29374	317
Ti	6179	6851	74	7816	8302	90	9278	9740	102	7768	7992	81	7714	7841	79
P	305	<LOD	2073	480	<LOD	2497	524	<LOD	2209	262	<LOD	2052	916	<LOD	2154
Sc	20	-	-	20	-	-	22	-	-	22	-	-	20	-	-
Be	3	-	-	4	-	-	4	-	-	5	-	-	4	-	-
V	136	100	5	177	137	6	161	133	6	178	137	6	156	128	6
Cr	140	154	7	130	163	8	150	188	8	130	155	7	130	159	7
Co	21	16.9	0.7	20	22.4	0.8	26	17.9	0.7	21	16.7	0.6	21	14.1	0.6
Ni	76	<LOD	20	71	<LOD	22	79	<LOD	20	74	<LOD	20	66	23	6
Cu	27	27	3	31	31	3	35	33	3	33	33	3	30	34	3
Zn	63	47	2	84	65	2	88	71	2	150	146	3	74	69	2
Cd	< 0.5	-	-	< 0.5	-	-	< 0.5	-	-	< 0.5	-	-	< 0.5	-	-
S	0.08	1184	269	0.641	5916	416	0.273	2013	312	1.73	9792	450	0.927	7530	407
Ga	28	-	-	26	-	-	28	-	-	29	-	-	26	-	-
Ge	1.9	-	-	1.3	-	-	1.6	-	-	0.9	-	-	1.5	-	-
As	16	13.7	1.1	11	15.6	1.2	< 5	7.2	1	5	13.2	1	8	11.3	1
Rb	129	142.6	1.5	135	147.3	1.6	139	150	1.6	173	195.1	1.7	141	157.8	1.5
Sr	131	138.7	1.3	140	139.5	1.4	137	136.9	1.4	138	142	1.3	147	155.9	1.4
Y	28.5	-	-	29.6	-	-	37.2	-	-	39.2	-	-	38.7	-	-
Zr	205	273	2	280	406	3	335	494	3	261	392	3	230	356	3
Nb	24.1	-	-	31.7	-	-	30.1	-	-	39.1	-	-	26.9	-	-
Mo	< 2	<LOD	3.6	< 2	<LOD	3.9	< 2	<LOD	4	< 2	<LOD	3.6	< 2	<LOD	3.6
Ag	< 0.3	<LOD	17	0.4	<LOD	18	< 0.3	<LOD	17	0.5	<LOD	16	< 0.3	<LOD	16
In	< 0.1	-	-	< 0.1	-	-	< 0.1	-	-	< 0.1	-	-	< 0.1	-	-
Sn	3	<LOD	28	3	<LOD	29	4	<LOD	29	3	<LOD	28	3	<LOD	27
Sb	0.9	<LOD	30	< 0.2	<LOD	31	< 0.2	<LOD	30	< 0.2	<LOD	29	< 0.2	<LOD	29
Cs	8	-	-	8.3	-	-	8.4	-	-	10.3	-	-	8.7	-	-
Ba	337	-	-	388	-	-	453	-	-	390	-	-	388	-	-
La	51.7	-	-	52.4	-	-	54.8	-	-	70.1	-	-	59.2	-	-
Ce	96.8	-	-	110	-	-	109	-	-	146	-	-	121	-	-
Pr	10.8	-	-	11.8	-	-	12.2	-	-	16.7	-	-	14.2	-	-
Nd	38	-	-	42.2	-	-	43.8	-	-	61.4	-	-	53.1	-	-
Sm	6.85	-	-	7.75	-	-	8.18	-	-	12	-	-	10.4	-	-
Eu	1.44	-	-	1.6	-	-	1.7	-	-	2.41	-	-	2.29	-	-
Gd	5.29	-	-	5.97	-	-	7.01	-	-	9.48	-	-	8.96	-	-
Tb	0.91	-	-	0.99	-	-	1.16	-	-	1.44	-	-	1.38	-	-
Dy	5.4	-	-	5.69	-	-	6.89	-	-	7.96	-	-	7.56	-	-
Ho	1.04	-	-	1.11	-	-	1.37	-	-	1.52	-	-	1.43	-	-
Er	3.1	-	-	3.22	-	-	4.05	-	-	4.3	-	-	4.01	-	-
Tm	0.494	-	-	0.489	-	-	0.621	-	-	0.634	-	-	0.582	-	-
Yb	3.16	-	-	3.28	-	-	4.18	-	-	4.17	-	-	3.79	-	-
Lu	0.458	-	-	0.545	-	-	0.691	-	-	0.664	-	-	0.598	-	-
Hf	5.8	-	-	7.4	-	-	8.2	-	-	6.6	-	-	5.8	-	-
Ta	1.44	-	-	1.97	-	-	2.05	-	-	2.36	-	-	1.76	-	-
W	< 0.5	<LOD	10	1.9	<LOD	12	2.1	<LOD	11	2.4	<LOD	10	1.8	<LOD	10
Tl	0.49	-	-	0.46	-	-	0.54	-	-	0.52	-	-	0.52	-	-
Pb	21	27.2	1.6	14	21.6	1.6	15	16.1	1.5	9	18.6	1.5	6	13.1	1.4
Bi	0.2	<LOD	13	< 0.1	<LOD	14	< 0.1	<LOD	14	< 0.1	<LOD	13	< 0.1	<LOD	13
Th	14.7	31	5	14	45	5	14.7	50	6	15.7	43	5	13.4	41	5
U	3.01	<LOD	4.6	3.14	<LOD	4.9	4.29	<LOD	4.8	4.11	<LOD	4.6	4.33	<LOD	4.5
Cl	-	<LOD	305	-	401	117	-	662	121	-	453	105	-	335	102
Se	-	<LOD	1.4	-	<LOD	1.5	-	<LOD	1.5	-	<LOD	1.4	-	<LOD	1.4
Cd	-	<LOD	18	-	<LOD	19	-	<LOD	19	-	<LOD	18	-	<LOD	18
Hg	-	<LOD	4.4	-	5.4	1.6	-	<LOD	4.6	-	7.5	1.5	-	5.3	1.5

Table A1- continued.

Sample	B-90 2436.35		
Lithology	Mudstone		
Type	ICMPS	pXRF	SD
Si	229943	-	-
Al	93518	-	-
Fe	55186	55917	215
Mn	356	349	9
Mg	11519	-	-
Ca	2001	1882	73
Na	4970	-	-
K	32708	39729	424
Ti	6065	6732	75
P	305	<LOD	2370
Sc	23	-	-
Be	3	-	-
V	152	115	6
Cr	130	170	8
Co	16	22.2	0.8
Ni	62	<LOD	22
Cu	33	41	3
Zn	47	43	2
Cd	< 0.5	-	-
S	0.034	<LOD	825
Ga	32	-	-
Ge	2	-	-
As	< 5	5.6	1
Rb	169	180.9	1.7
Sr	164	169.8	1.5
Y	32.6	-	-
Zr	175	251	2
Nb	29.5	-	-
Mo	< 2	<LOD	3.7
Ag	0.3	<LOD	18
In	< 0.1	-	-
Sn	5	<LOD	29
Sb	0.6	<LOD	31
Cs	10.7	-	-
Ba	446	-	-
La	48.1	-	-
Ce	95.5	-	-
Pr	10.9	-	-
Nd	39.4	-	-
Sm	7.65	-	-
Eu	1.59	-	-
Gd	6.41	-	-
Tb	1.02	-	-
Dy	5.84	-	-
Ho	1.13	-	-
Er	3.23	-	-
Tm	0.487	-	-
Yb	3.25	-	-
Lu	0.535	-	-
Hf	5.1	-	-
Ta	1.85	-	-
W	2.4	<LOD	11
Tl	0.57	-	-
Pb	6	18	1.6
Bi	0.3	<LOD	14
Th	15.9	47	5
U	2.87	<LOD	5
Cl	-	572	117
Se	-	<LOD	1.5
Cd	-	<LOD	19
Hg	-	<LOD	4.6

Appendix 2: Table A2: Comparison between in-situ XRF on core samples and previous ICPMS geochemical analyses from the core location.

Sample	B-90 2235.37			B-90 2241.57			B-90 2245.78			B-90 2247.20		
Lithology	Mudstone			Mudstone			Mudstone			Mudstone		
Type	ICPMS	pXRF	SD	ICPMS	pXRF	SD	ICPMS	pXRF	SD	ICPMS	pXRF	SD
Si	278101	-	-	285114	-	-	271368	-	-	242053	-	-
Al	62624	-	-	68210	-	-	72922	-	-	84436	-	-
Fe	47632	48372	187	39938	38872	153	41686	39306	154	50919	52221	202
Mn	503	434	10	271	339	9	379	278	8	232	235	8
Mg	8805	-	-	10614	-	-	11338	-	-	11820	-	-
Ca	5075	3885	82	1930	5417	96	2144	1289	61	1573	979	65
Na	6973	-	-	7048	-	-	6973	-	-	6009	-	-
K	22414	26250	301	27146	33206	355	29885	29876	326	32874	40545	429
Ti	7528	8363	87	6857	8855	89	6503	6488	70	5826	6385	72
P	829	<LOD	2385	393	<LOD	2311	305	<LOD	2229	218	<LOD	2362
Sc	17	-	-	19	-	-	19	-	-	22	-	-
Be	3	-	-	3	-	-	3	-	-	3	-	-
V	134	103	6	140	382	8	144	94	5	162	124	6
Cr	110	138	7	130	135	7	130	115	6	130	164	7
Co	25	20.8	0.8	23	16	0.7	21	17.4	0.7	27	23.4	0.8
Ni	71	<LOD	21	69	22	7	75	<LOD	21	95	<LOD	22
Cu	29	36	3	38	38	3	34	48	3	39	41	3
Zn	105	71	2	119	92	3	91	77	2	103	94	3
Cd	< 0.5	<LOD	19	< 0.5	<LOD	19	< 0.5	<LOD	19	< 0.5	<LOD	19
S	0.387	4154	359	0.272	6910	410	0.274	5647	377	0.228	3418	352
Ga	22	-	-	23	-	-	24	-	-	28	-	-
Ge	1.6	-	-	1.9	-	-	1.9	-	-	2	-	-
As	9	9.2	1.1	9	10.5	1.1	9	10.3	1	13	14.3	1.2
Rb	118	137.2	1.5	136	168.5	1.6	156	142.3	1.5	187	207	1.9
Sr	154	195.3	1.6	120	189.7	1.6	130	224.9	1.7	139	287	2
Y	31.7	-	-	29.2	-	-	26.5	-	-	24.7	-	-
Zr	313	428	3	297	332	3	235	420	3	182	239	2
Nb	33.1	-	-	26.3	-	-	24.8	-	-	22.8	-	-
Mo	< 2	<LOD	3.8	< 2	<LOD	3.7	< 2	<LOD	3.8	< 2	<LOD	3.7
Ag	< 0.3	<LOD	17	< 0.3	<LOD	17	< 0.3	<LOD	17	< 0.3	<LOD	18
In	< 0.1	-	-	< 0.1	-	-	< 0.1	-	-	< 0.1	-	-
Sn	3	31	10	2	<LOD	29	3	<LOD	29	3	<LOD	30
Sb	< 0.2	<LOD	31	0.3	<LOD	31	0.5	<LOD	31	0.6	<LOD	32
Cs	6.8	-	-	6.7	-	-	7.9	-	-	10.7	-	-
Ba	333	-	-	343	-	-	359	-	-	388	-	-
La	49	-	-	47.2	-	-	47.4	-	-	50.1	-	-
Ce	104	-	-	93.8	-	-	93.7	-	-	102	-	-
Pr	11.1	-	-	10.2	-	-	10.4	-	-	11.6	-	-
Nd	42.9	-	-	35.9	-	-	36.3	-	-	41.9	-	-
Sm	8.29	-	-	6.19	-	-	6.18	-	-	7.34	-	-
Eu	1.82	-	-	1.28	-	-	1.28	-	-	1.49	-	-
Gd	6.74	-	-	4.93	-	-	4.77	-	-	5.12	-	-
Tb	1.12	-	-	0.85	-	-	0.8	-	-	0.85	-	-
Dy	6.33	-	-	5.2	-	-	4.84	-	-	4.88	-	-
Ho	1.19	-	-	1.07	-	-	0.98	-	-	0.95	-	-
Er	3.43	-	-	3.25	-	-	2.99	-	-	2.83	-	-
Tm	0.536	-	-	0.527	-	-	0.497	-	-	0.464	-	-
Yb	3.49	-	-	3.5	-	-	3.26	-	-	3.02	-	-
Lu	0.485	-	-	0.499	-	-	0.464	-	-	0.435	-	-
Hf	8.5	-	-	7.8	-	-	6.4	-	-	4.9	-	-
Ta	2.06	-	-	1.54	-	-	1.45	-	-	1.36	-	-
W	1.6	<LOD	11	< 0.5	<LOD	11	0.8	12	4	< 0.5	<LOD	12
Tl	0.44	-	-	0.48	-	-	0.54	-	-	0.69	-	-
Pb	22	19.6	1.6	18	23.1	1.6	17	16.8	1.5	23	20.3	1.6
Bi	< 0.1	<LOD	14	< 0.1	<LOD	14	0.1	<LOD	14	0.2	<LOD	14
Th	12.5	31	5	12.4	34	5	12.8	29	5	13.4	39	5
U	3.01	<LOD	4.8	2.89	<LOD	4.8	2.75	<LOD	4.9	2.58	<LOD	5.2
LE	-	-	-	-	-	-	-	-	-	-	-	-
Cl	-	930	120	-	974	119	-	612	107	-	481	113
Se	-	<LOD	1.5	-	<LOD	1.5	-	<LOD	1.5	-	<LOD	1.5
Hg	-	6.3	1.6	-	<LOD	4.6	-	<LOD	4.6	-	6.2	1.6

Notes: 1. All values are in ppm, 2. SD= standard deviation, 3. LOD= limit of detection

Table A2- continued.

Sample	B-90 2256.56			B-90 2263.94			B-90 2278.21			B-90 2237.28		
Lithology	Mudstone			Mudstone			Mudstone			Sandstone		
Type	ICPMS	pXRF	SD	ICPMS	pXRF	SD	ICPMS	pXRF	SD	ICPMS	pXRF	SD
Si	266038	-	-	255846	-	-	244998	-	-	314570	-	-
Al	70908	-	-	75506	-	-	85234	-	-	15770	-	-
Fe	58683	57878	224	51409	49013	188	40218	36398	141	25529	19679	92
Mn	1084	941	14	620	422	9	240	241	8	1433	1090	14
Mg	12062	-	-	11760	-	-	9287	-	-	3136	-	-
Ca	3645	2498	75	2359	1358	64	1072	322	53	84989	125495	1048
Na	6232	-	-	5861	-	-	4674	-	-	5193	-	-
K	25320	31996	358	27727	32925	357	24572	29479	325	7803	8745	146
Ti	6551	7477	82	6221	7337	78	6179	6682	72	4537	3875	47
P	567	<LOD	2446	480	<LOD	2372	305	<LOD	2087	480	<LOD	4673
Sc	21	-	-	22	-	-	20	-	-	4	-	-
Be	3	-	-	3	-	-	3	-	-	< 1	-	-
V	133	118	6	142	141	6	136	127	5	36	31	4
Cr	120	139	7	120	129	7	140	149	7	100	52	5
Co	29	25.6	0.9	27	23	0.8	21	16.3	0.6	5	8.8	0.5
Ni	79	<LOD	23	80	<LOD	22	76	<LOD	20	20	<LOD	19
Cu	44	62	4	39	49	3	27	38	3	11	18	3
Zn	95	74	3	99	79	2	63	45.1	2	38	13.6	1.7
Cd	< 0.5	<LOD	20	< 0.5	<LOD	19	< 0.5	<LOD	18	< 0.5	<LOD	20
S	0.067	3595	366	0.185	3723	351	0.08	3671	332	0.075	1209	360
Ga	24	-	-	26	-	-	28	-	-	5	-	-
Ge	1.9	-	-	1.9	-	-	1.9	-	-	1	-	-
As	10	7.1	1.1	8	8.9	1.1	16	19.8	1.1	< 5	3.4	0.9
Rb	125	134.6	1.5	135	148.9	1.5	129	146.8	1.5	29	30.2	0.9
Sr	141	269.4	2	149	244.6	1.8	131	153	1.4	502	591	3
Y	37.5	-	-	31.7	-	-	28.5	-	-	22.6	-	-
Zr	289	364	3	231	297	3	205	261	2	534	773	4
Nb	24.8	-	-	26.1	-	-	24.1	-	-	18.8	-	-
Mo	< 2	<LOD	3.9	< 2	<LOD	3.7	< 2	<LOD	3.6	< 2	<LOD	4.3
Ag	0.3	<LOD	18	0.3	<LOD	17	< 0.3	<LOD	17	< 0.3	<LOD	18
In	< 0.1	-	-	< 0.1	-	-	< 0.1	-	-	< 0.1	-	-
Sn	3	<LOD	30	3	<LOD	29	3	<LOD	28	< 1	<LOD	30
Sb	0.8	<LOD	32	0.7	<LOD	31	0.9	<LOD	30	0.4	<LOD	32
Cs	6.6	-	-	7.5	-	-	8	-	-	0.8	-	-
Ba	353	-	-	363	-	-	337	-	-	202	-	-
La	50.7	-	-	53.3	-	-	51.7	-	-	22.3	-	-
Ce	102	-	-	106	-	-	96.8	-	-	48.1	-	-
Pr	11.8	-	-	12.4	-	-	10.8	-	-	5.4	-	-
Nd	43.9	-	-	45	-	-	38	-	-	20.7	-	-
Sm	8.27	-	-	8.17	-	-	6.85	-	-	4.07	-	-
Eu	1.81	-	-	1.74	-	-	1.44	-	-	0.845	-	-
Gd	6.81	-	-	6.51	-	-	5.29	-	-	3.72	-	-
Tb	1.18	-	-	1.08	-	-	0.91	-	-	0.64	-	-
Dy	6.76	-	-	6.12	-	-	5.4	-	-	3.83	-	-
Ho	1.31	-	-	1.17	-	-	1.04	-	-	0.76	-	-
Er	3.89	-	-	3.49	-	-	3.1	-	-	2.29	-	-
Tm	0.62	-	-	0.552	-	-	0.494	-	-	0.373	-	-
Yb	3.99	-	-	3.56	-	-	3.16	-	-	2.46	-	-
Lu	0.567	-	-	0.507	-	-	0.458	-	-	0.364	-	-
Hf	7.5	-	-	6.1	-	-	5.8	-	-	13.2	-	-
Ta	1.46	-	-	1.49	-	-	1.44	-	-	0.98	-	-
W	< 0.5	<LOD	12	0.7	<LOD	11	< 0.5	<LOD	10	< 0.5	<LOD	11
Tl	0.47	-	-	0.5	-	-	0.49	-	-	0.11	-	-
Pb	17	22	1.7	15	22.6	1.6	21	23.9	1.5	9	7.1	1.3
Bi	0.2	<LOD	14	0.2	<LOD	14	0.2	<LOD	13	< 0.1	<LOD	14
Th	12.6	19	5	13.1	28	5	14.7	38	5	5.95	<LOD	17
U	3.23	<LOD	5.1	2.95	<LOD	4.9	3.01	<LOD	4.5	1.88	<LOD	5.6
LE	-	-	-	-	-	-	-	-	-	-	-	-
Cl	-	990	126	-	1053	121	-	719	109	-	13066	266
Se	-	<LOD	1.5	-	<LOD	1.4	-	<LOD	1.4	-	<LOD	1.5
Hg	-	6.2	1.7	-	5.8	1.6	-	4.8	1.5	-	<LOD	4.5

Table A2- continued.

Sample	B-90 2268.07			B-90 2281.68		
Lithology	Sandstone			Sandstone		
Type	ICPMS	pXRF	SD	ICPMS	pXRF	SD
Si	405603	-	-	324202	-	-
Al	18696	-	-	11172	-	-
Fe	19864	14493	64	20354	13914	74
Mn	101	98	5	1820	1241	17
Mg	2774	-	-	2352	-	-
Ca	1287	731	38	75840	108602	991
Na	3338	-	-	4080	-	-
K	7305	6693	111	4649	3873	106
Ti	3626	3624	41	4010	3163	44
P	87	<LOD	1675	131	<LOD	4583
Sc	6	-	-	5	-	-
Be	< 1	-	-	< 1	-	-
V	43	70	4	62	20	4
Cr	80	46	4	110	58	5
Co	6	6.7	0.4	< 1	6.6	0.5
Ni	29	<LOD	16	15	<LOD	18
Cu	23	23	3	7	13	3
Zn	44	22.8	1.5	35	8.7	1.7
Cd	< 0.5	<LOD	17	< 0.5	<LOD	21
S	0.012	705	181	0.057	<LOD	1038
Ga	7	-	-	5	-	-
Ge	1.5	-	-	1.2	-	-
As	< 5	3.2	0.8	< 5	4.3	0.9
Rb	30	30.9	0.7	18	19.3	0.8
Sr	49	52.1	0.8	326	383	3
Y	17.4	-	-	19	-	-
Zr	308	453	3	791	762	5
Nb	12	-	-	15.4	-	-
Mo	< 2	<LOD	3.4	< 2	7	1.5
Ag	< 0.3	<LOD	15	< 0.3	<LOD	19
In	< 0.1	-	-	< 0.1	-	-
Sn	2	<LOD	26	< 1	<LOD	32
Sb	0.4	<LOD	28	0.4	<LOD	34
Cs	1.2	-	-	0.5	-	-
Ba	377	-	-	132	-	-
La	18.7	-	-	22.5	-	-
Ce	40.6	-	-	53.9	-	-
Pr	4.58	-	-	5.67	-	-
Nd	17.2	-	-	20.8	-	-
Sm	3.44	-	-	4.04	-	-
Eu	0.718	-	-	0.706	-	-
Gd	3.04	-	-	3.24	-	-
Tb	0.52	-	-	0.54	-	-
Dy	3.13	-	-	3.28	-	-
Ho	0.64	-	-	0.67	-	-
Er	1.97	-	-	2.09	-	-
Tm	0.317	-	-	0.344	-	-
Yb	2.11	-	-	2.36	-	-
Lu	0.317	-	-	0.367	-	-
Hf	7.7	-	-	19.3	-	-
Ta	0.77	-	-	0.96	-	-
W	< 0.5	<LOD	9	< 0.5	<LOD	11
Tl	0.13	-	-	0.06	-	-
Pb	10	11.3	1.2	9	8.4	1.4
Bi	< 0.1	<LOD	12	< 0.1	<LOD	15
Th	5.19	<LOD	14	7.32	34	6
U	1.51	<LOD	3.7	1.94	<LOD	5.4
LE	-	-	-	-	-	-
Cl	-	1366	94	-	23008	393
Se	-	<LOD	1.2	-	<LOD	1.6
Hg	-	<LOD	3.8	-	<LOD	4.6

Appendix 3: Spectrophotometer on types of samples (A, B, C and D) on powdered samples from Panuke B-90 and Cohasset A-52.

Well		Cohasset A-52						
Depth (m)		2072.90	2074.72	2123.52	2138.22	2159.63	2418.75	2597.05
Type of Sample[1]		A	A	A	A	A	A	A
Illuminant setting	**L*(D65)**	58.2	52.0	52.2	47.4	70.4	40.8	66.0
	a*(D65)	0.6	0.5	0.7	1.7	-3.1	2.5	-0.3
	b*(D65)	6.5	6.6	6.5	8.0	8.3	7.6	6.8
Relative intensity at 10 nm wavelength increments starting at specified wavelength	**360nm**	15.6	11.3	11.9	8.7	20.9	6.9	20.0
	370nm	16.6	12.1	12.6	9.3	22.5	7.2	21.5
	380nm	17.6	12.9	13.4	9.9	24.5	7.5	23.0
	390nm	18.4	13.6	14.0	10.4	26.2	7.8	24.4
	400nm	19.2	14.2	14.7	10.8	27.7	8.0	25.7
	410nm	19.9	14.8	15.1	11.2	29.1	8.3	26.7
	420nm	20.5	15.3	15.7	11.7	30.5	8.5	27.7
	430nm	21.1	15.8	16.1	12.1	31.9	8.7	28.6
	440nm	21.7	16.3	16.6	12.5	33.3	8.9	29.4
	450nm	22.3	16.8	17.0	12.9	34.4	9.1	30.2
	460nm	22.7	17.1	17.3	13.2	35.4	9.3	30.8
	470nm	23.1	17.5	17.7	13.4	36.5	9.5	31.4
	480nm	23.5	17.9	18.0	13.7	37.5	9.7	32.0
	490nm	23.8	18.2	18.4	14.0	38.4	9.9	32.6
	500nm	24.2	18.5	18.7	14.3	39.3	10.2	33.1
	510nm	24.6	18.8	19.0	14.7	40.0	10.4	33.6
	520nm	25.1	19.2	19.4	15.1	40.9	10.7	34.2
	530nm	25.4	19.5	19.6	15.4	41.4	11.0	34.6
	540nm	25.7	19.8	19.9	15.7	41.8	11.3	34.9
	550nm	26.0	20.1	20.2	16.1	42.2	11.5	35.3
	560nm	26.3	20.3	20.5	16.4	42.3	11.8	35.7
	570nm	26.7	20.6	20.8	16.8	42.4	12.1	36.0
	580nm	27.0	20.8	21.0	17.1	42.2	12.4	36.2
	590nm	27.2	20.9	21.2	17.4	42.0	12.7	36.3
	600nm	27.5	21.2	21.5	17.7	42.0	13.0	36.6
	610nm	27.7	21.4	21.7	18.0	41.7	13.3	36.8
	620nm	28.0	21.6	21.9	18.3	41.4	13.6	37.0
	630nm	28.3	21.8	22.2	18.5	41.3	13.9	37.3
	640nm	28.3	21.9	22.3	18.8	40.9	14.1	37.2
	650nm	28.6	22.2	22.5	19.0	40.8	14.5	37.5
	660nm	28.8	22.3	22.8	19.3	40.5	14.8	37.6
	670nm	29.0	22.5	23.0	19.5	40.0	15.1	37.7
	680nm	29.3	22.6	23.0	19.8	40.0	15.3	38.0
	690nm	29.5	22.9	23.4	20.0	39.8	15.5	38.1
	700nm	29.7	23.1	23.5	20.3	39.2	15.9	38.2
	710nm	30.0	23.2	23.7	20.5	39.3	16.2	38.4
	720nm	30.1	23.4	24.1	20.8	38.9	16.4	38.6
	730nm	30.5	23.6	24.2	21.0	38.9	16.7	38.8
	740nm	30.7	23.8	24.4	21.3	39.0	17.0	39.1

Note: 1. Type A= Powdered core samples with ICPMS, pXRF and spectrophotometer analyses; Type B= Powdered core samples with pXRF and spectrophotometer analyses; Type D= Powdered samples from cuttings with pXRF and spectrophotometer analyses.

Appendix 3: continued.

Well		Panuke B-90										
Depth (m)		2097.27	2110	2115	2120	2125	2130	2135	2140	2145	2150	2155
Type of Sample[1]		A	D	D	D	D	D	D	D	D	D	D
Illuminant setting	L*(D65)	43.1	48.8	36.0	51.5	52.0	50.9	37.0	52.0	48.1	49.3	49.5
	a*(D65)	2.4	1.4	1.7	1.2	1.4	1.0	2.3	2.1	2.3	1.5	1.2
	b*(D65)	8.1	9.1	8.1	9.3	8.6	8.8	10.1	10.7	11.5	9.6	8.1
Relative intensity at 10 nm wavelength increments starting at specified wavelength	360nm	7.8	12.4	18.0	16.5	15.5	17.3	17.3	17.5	18.8	11.8	12.9
	370nm	8.1	13.1	19.5	17.7	16.4	18.4	18.5	18.7	20.3	12.6	13.7
	380nm	8.4	14.0	21.2	19.0	17.4	19.6	19.8	20.1	22.0	13.3	14.5
	390nm	8.6	14.9	22.5	20.2	18.2	20.8	20.9	21.4	23.5	13.9	15.1
	400nm	8.9	15.6	23.7	21.2	19.0	21.8	21.8	22.5	24.7	14.5	15.7
	410nm	9.1	16.3	24.7	22.0	19.6	22.6	22.7	23.4	25.6	15.1	16.1
	420nm	9.4	17.2	25.7	22.9	20.2	23.5	23.5	24.4	26.7	15.6	16.7
	430nm	9.6	17.9	26.7	23.7	20.8	24.3	24.3	25.2	27.5	16.0	17.0
	440nm	9.9	18.7	27.6	24.5	21.4	25.0	25.1	26.1	28.3	16.5	17.5
	450nm	10.2	19.5	28.5	25.2	21.9	25.8	25.8	26.9	29.1	17.0	17.9
	460nm	10.4	20.1	29.1	25.8	22.4	26.4	26.5	27.5	29.7	17.3	18.2
	470nm	10.6	20.7	29.8	26.4	23.0	27.0	27.0	28.2	30.3	17.7	18.5
	480nm	10.9	21.3	30.5	27.0	23.4	27.6	27.6	28.9	31.0	18.0	18.8
	490nm	11.1	21.9	31.2	27.6	23.8	28.1	28.1	29.4	31.5	18.3	19.2
	500nm	11.4	22.5	31.7	28.0	24.2	28.6	28.6	30.0	32.1	18.6	19.5
	510nm	11.7	23.2	32.2	28.5	24.6	29.2	29.2	30.6	32.5	19.0	19.8
	520nm	12.0	23.9	32.8	29.1	25.1	29.7	29.8	31.1	33.1	19.4	20.2
	530nm	12.3	24.6	33.3	29.4	25.4	30.1	30.1	31.5	33.5	19.7	20.5
	540nm	12.6	25.2	33.6	29.8	26.0	30.6	30.6	31.9	33.9	19.9	20.8
	550nm	12.9	25.8	34.0	30.1	26.6	31.0	31.1	32.3	34.2	20.3	21.0
	560nm	13.3	26.4	34.3	30.4	27.4	31.4	31.6	32.7	34.5	20.6	21.3
	570nm	13.6	27.0	34.6	30.6	28.2	31.9	32.0	33.1	34.9	20.8	21.6
	580nm	13.9	27.4	34.8	30.8	28.9	32.2	32.5	33.3	35.1	21.1	21.9
	590nm	14.2	27.9	34.9	30.8	29.3	32.5	32.7	33.5	35.2	21.3	22.1
	600nm	14.6	28.4	35.1	31.0	29.7	32.7	33.1	33.7	35.5	21.6	22.4
	610nm	14.9	28.8	35.2	31.1	30.0	32.9	33.3	33.8	35.6	21.8	22.7
	620nm	15.2	29.1	35.2	31.1	30.1	33.0	33.4	33.8	35.7	22.0	23.0
	630nm	15.6	29.6	35.5	31.3	30.4	33.3	33.7	34.1	36.0	22.3	23.3
	640nm	15.8	29.7	35.4	31.2	30.4	33.2	33.6	34.0	35.9	22.5	23.5
	650nm	16.2	30.1	35.5	31.4	30.7	33.5	33.8	34.2	36.2	22.8	23.8
	660nm	16.5	30.4	35.6	31.4	30.8	33.5	33.9	34.1	36.2	23.0	24.0
	670nm	16.8	30.6	35.6	31.4	30.9	33.6	34.0	34.2	36.4	23.0	24.3
	680nm	17.0	31.0	35.8	31.6	31.1	33.8	34.0	34.3	36.4	23.3	24.5
	690nm	17.3	31.3	35.9	31.7	31.3	33.9	34.3	34.5	36.6	23.7	24.8
	700nm	17.7	31.5	35.8	31.8	31.4	33.9	34.3	34.4	36.7	23.8	25.1
	710nm	18.0	31.8	36.1	31.8	31.6	34.3	34.5	34.6	36.9	24.0	25.4
	720nm	18.2	32.1	36.2	32.0	31.9	34.4	34.7	34.8	37.1	24.3	25.6
	730nm	18.6	32.3	36.4	32.1	32.2	34.7	35.0	35.0	37.3	24.4	25.9
	740nm	18.8	32.7	36.6	32.3	32.4	35.0	35.1	35.2	37.5	24.7	26.2

Appendix 3: continued.

Well		Panuke B-90											
Depth (m)		2160	2165	2170	2175	2180	2185	2190	2195	2200	2205	2210	2215
Type of Sample[1]		D	D	D	D	D	D	D	D	D	D	D	D
Illuminant setting	L*(D65)	44.6	46.0	49.3	47.4	47.0	50.2	45.9	44.7	44.7	44.8	44.2	47.6
	a*(D65)	1.4	1.4	1.2	1.1	1.3	1.2	1.4	1.2	1.1	1.1	1.3	1.0
	b*(D65)	7.8	7.9	7.5	7.3	7.9	7.3	7.5	7.0	7.0	7.0	7.2	7.0
Relative intensity at 10 nm wavelength increments starting at specified wavelength	360nm	13.9	10.4	11.4	11.2	11.6	9.9	11.2	11.3	11.2	9.0	9.9	9.3
	370nm	14.6	11.1	11.7	11.9	12.2	10.6	11.9	11.9	11.9	9.6	10.4	9.9
	380nm	15.3	11.7	12.0	12.6	12.9	11.2	12.6	12.5	12.6	10.3	11.0	10.5
	390nm	15.8	12.2	12.2	13.1	13.3	11.8	13.1	13.1	13.1	10.7	11.4	10.9
	400nm	16.2	12.7	12.4	13.6	13.7	12.2	13.5	13.6	13.6	11.1	11.7	11.3
	410nm	16.7	13.2	12.7	14.1	14.1	12.7	14.0	14.1	14.0	11.6	12.1	11.7
	420nm	17.0	13.7	13.0	14.4	14.5	13.2	14.4	14.6	14.5	12.0	12.5	12.1
	430nm	17.3	14.1	13.3	14.8	14.8	13.6	14.8	14.9	14.9	12.4	12.8	12.5
	440nm	17.7	14.5	13.8	15.2	15.2	14.0	15.2	15.4	15.3	12.8	13.1	12.8
	450nm	18.1	15.0	14.3	15.5	15.5	14.4	15.5	15.7	15.7	13.2	13.4	13.2
	460nm	18.3	15.3	14.7	15.8	15.7	14.7	15.8	16.0	15.9	13.5	13.6	13.4
	470nm	18.7	15.6	15.2	16.1	15.9	15.1	16.1	16.3	16.2	13.8	13.9	13.7
	480nm	19.0	16.0	15.5	16.3	16.2	15.4	16.3	16.6	16.5	14.1	14.2	14.1
	490nm	19.2	16.3	15.9	16.6	16.5	15.7	16.6	16.9	16.8	14.3	14.4	14.4
	500nm	19.5	16.8	16.2	16.9	16.7	16.0	16.9	17.2	17.1	14.7	14.7	14.6
	510nm	19.8	17.2	16.6	17.2	17.0	16.3	17.2	17.4	17.3	15.0	15.0	14.9
	520nm	20.1	17.5	17.1	17.5	17.2	16.7	17.5	17.8	17.6	15.4	15.2	15.3
	530nm	20.4	17.9	17.7	17.8	17.5	17.0	17.7	18.0	17.9	15.7	15.4	15.5
	540nm	20.7	18.2	18.4	18.0	17.7	17.3	17.9	18.3	18.2	15.9	15.7	15.8
	550nm	21.0	18.6	19.5	18.2	17.9	17.6	18.2	18.6	18.4	16.2	16.0	16.0
	560nm	21.3	19.0	20.9	18.5	18.2	17.8	18.4	18.8	18.6	16.5	16.2	16.3
	570nm	21.6	19.3	22.5	18.7	18.4	18.1	18.6	19.1	18.8	16.8	16.5	16.6
	580nm	21.9	19.6	23.8	18.9	18.6	18.4	18.9	19.3	19.0	17.0	16.7	16.8
	590nm	22.0	19.9	24.9	19.1	18.8	18.6	19.0	19.5	19.2	17.2	16.9	17.0
	600nm	22.4	20.3	25.8	19.4	19.0	18.9	19.3	19.7	19.5	17.6	17.1	17.3
	610nm	22.7	20.6	26.4	19.6	19.2	19.0	19.4	19.9	19.7	17.8	17.4	17.6
	620nm	22.9	20.8	26.9	19.8	19.4	19.3	19.6	20.1	19.9	18.0	17.6	17.7
	630nm	23.2	21.2	27.4	20.1	19.7	19.6	19.9	20.4	20.1	18.3	17.9	18.0
	640nm	23.3	21.4	27.6	20.2	19.7	19.7	20.0	20.5	20.2	18.5	18.0	18.1
	650nm	23.6	21.8	28.1	20.4	20.0	20.0	20.2	20.7	20.4	18.8	18.4	18.4
	660nm	23.8	22.1	28.4	20.6	20.2	20.1	20.4	21.0	20.6	19.0	18.5	18.7
	670nm	24.1	22.3	28.7	20.9	20.4	20.3	20.5	21.2	20.9	19.2	18.7	18.8
	680nm	24.3	22.6	29.1	21.0	20.5	20.6	20.8	21.4	21.1	19.6	18.9	19.1
	690nm	24.6	23.0	29.6	21.2	20.8	20.8	21.0	21.6	21.2	19.8	19.2	19.2
	700nm	24.8	23.3	29.8	21.5	21.0	20.9	21.2	21.8	21.4	19.9	19.4	19.5
	710nm	25.1	23.4	30.3	21.7	21.2	21.2	21.4	22.0	21.7	20.3	19.7	19.7
	720nm	25.3	23.9	30.6	21.9	21.4	21.4	21.5	22.1	21.8	20.5	19.8	19.9
	730nm	25.5	24.0	30.9	22.2	21.6	21.6	21.8	22.4	22.2	20.7	20.2	20.1
	740nm	25.7	24.3	31.3	22.4	21.7	21.8	22.0	22.6	22.3	21.0	20.4	20.3

Appendix 3: continued.

Well		Panuke B-90								
Depth (m)		2215.15	2215.59	2216.17	2216.88	2217.78	2218.08	2219.36	2219.63	2220
Type of Sample[1]		B	B	B	B	B	B	B	B	D
Illuminant setting	**L*(D65)**	49.5	49.1	49.8	50.2	50.0	49.9	47.4	47.1	51.1
	a*(D65)	0.8	0.9	0.7	0.8	0.7	0.9	1.2	1.1	1.0
	b*(D65)	5.5	7.1	5.8	6.1	5.9	5.9	7.3	6.2	7.9
Relative intensity at 10 nm wavelength increments starting at specified wavelength	**360nm**	10.2	10.2	13.6	12.1	15.0	12.6	11.1	12.2	10.9
	370nm	10.8	10.8	14.3	12.8	16.0	13.3	11.8	12.9	11.4
	380nm	11.4	11.3	15.1	13.4	16.9	14.0	12.5	13.6	12.1
	390nm	11.9	11.7	15.6	13.9	17.7	14.5	13.0	14.1	12.5
	400nm	12.2	12.1	16.1	14.4	18.4	15.0	13.4	14.6	12.8
	410nm	12.6	12.5	16.6	14.9	19.1	15.5	13.9	15.1	13.3
	420nm	13.0	12.8	17.0	15.4	19.7	15.9	14.2	15.6	13.7
	430nm	13.4	13.1	17.4	15.8	20.4	16.4	14.6	16.1	14.0
	440nm	13.8	13.5	17.9	16.2	21.0	16.8	15.0	16.6	14.4
	450nm	14.1	13.8	18.3	16.7	21.6	17.3	15.3	17.1	14.8
	460nm	14.4	14.0	18.5	17.0	22.0	17.6	15.5	17.4	15.1
	470nm	14.6	14.3	18.9	17.3	22.5	17.9	15.8	17.8	15.4
	480nm	15.0	14.6	19.2	17.7	23.0	18.3	16.0	18.1	15.7
	490nm	15.2	14.9	19.6	18.0	23.5	18.6	16.2	18.4	16.1
	500nm	15.5	15.1	19.9	18.4	23.9	19.0	16.4	18.8	16.4
	510nm	15.8	15.3	20.2	18.7	24.3	19.4	16.7	19.2	16.7
	520nm	16.1	15.6	20.5	19.1	24.9	19.8	17.0	19.6	17.1
	530nm	16.3	15.8	20.8	19.4	25.2	20.1	17.3	19.9	17.5
	540nm	16.6	16.1	21.1	19.7	25.7	20.5	17.5	20.3	17.8
	550nm	16.8	16.3	21.3	20.0	26.1	20.9	17.7	20.7	18.1
	560nm	17.0	16.5	21.5	20.3	26.5	21.2	18.0	21.0	18.5
	570nm	17.3	16.8	21.8	20.6	26.9	21.6	18.2	21.3	18.8
	580nm	17.6	17.0	22.1	20.9	27.2	21.9	18.4	21.7	19.2
	590nm	17.7	17.1	22.3	21.1	27.5	22.2	18.5	21.9	19.4
	600nm	18.0	17.4	22.5	21.4	27.8	22.6	18.7	22.2	19.8
	610nm	18.2	17.6	22.7	21.6	28.1	22.9	18.9	22.5	20.1
	620nm	18.4	17.8	22.9	21.9	28.4	23.2	19.0	22.7	20.4
	630nm	18.7	18.1	23.1	22.1	28.7	23.5	19.2	23.1	20.8
	640nm	18.8	18.2	23.2	22.2	28.8	23.7	19.3	23.2	21.1
	650nm	19.1	18.4	23.4	22.5	29.2	24.1	19.5	23.4	21.4
	660nm	19.3	18.6	23.6	22.7	29.3	24.4	19.6	23.6	21.7
	670nm	19.5	18.8	23.7	22.9	29.6	24.6	19.7	23.8	21.9
	680nm	19.7	19.2	24.0	23.1	29.8	24.9	19.8	24.2	22.4
	690nm	19.9	19.2	24.1	23.3	30.0	25.1	20.0	24.3	22.7
	700nm	20.1	19.4	24.1	23.6	30.3	25.5	20.0	24.5	22.9
	710nm	20.3	19.6	24.4	23.6	30.6	25.7	20.2	24.7	23.2
	720nm	20.5	19.7	24.5	23.9	30.7	26.0	20.2	24.8	23.5
	730nm	20.8	20.0	24.6	24.0	31.0	26.3	20.4	25.0	23.8
	740nm	20.9	20.2	24.8	24.1	31.2	26.5	20.5	25.2	24.1

Appendix 3: continued.

Well		Panuke B-90							
Depth (m)		2220.22	2220.46	2220.64	2221.41	2222.60	2223.14	2225.62	2226.53
Type of Sample[1]		B	B	B	B	B	B	B	B
Illuminant setting	**L*(D65)**	47.2	48.2	47.5	53.4	52.0	58.2	53.0	49.3
	a*(D65)	1.1	1.0	0.9	0.6	0.9	0.8	1.4	0.7
	b*(D65)	6.9	6.3	6.0	5.9	6.8	7.7	7.4	5.5
Relative intensity at 10 nm wavelength increments starting at specified wavelength	**360nm**	13.3	13.4	13.5	14.3	15.2	15.1	16.4	14.6
	370nm	14.1	14.1	14.4	15.2	16.2	16.0	17.4	15.8
	380nm	14.9	14.8	15.4	16.2	17.2	17.0	18.4	16.9
	390nm	15.5	15.4	16.3	17.0	18.0	17.8	19.3	17.9
	400nm	16.1	15.9	16.9	17.8	18.8	18.4	19.9	18.6
	410nm	16.6	16.4	17.7	18.5	19.5	19.1	20.6	19.4
	420nm	17.2	16.8	18.3	19.3	20.2	19.7	21.4	20.1
	430nm	17.7	17.3	19.0	20.0	20.9	20.3	22.0	20.9
	440nm	18.2	17.8	19.7	20.7	21.6	20.9	22.7	21.6
	450nm	18.7	18.2	20.4	21.3	22.1	21.4	23.3	22.2
	460nm	19.0	18.6	20.8	21.8	22.6	21.8	23.8	22.7
	470nm	19.4	18.9	21.3	22.4	23.1	22.2	24.3	23.2
	480nm	19.8	19.3	21.9	22.9	23.6	22.7	24.8	23.7
	490nm	20.2	19.6	22.4	23.4	24.1	23.1	25.3	24.2
	500nm	20.6	19.9	22.9	23.9	24.6	23.5	25.8	24.7
	510nm	21.0	20.3	23.4	24.4	25.1	23.9	26.3	25.1
	520nm	21.4	20.7	23.9	25.0	25.5	24.3	26.8	25.7
	530nm	21.8	21.1	24.4	25.4	26.0	24.7	27.3	26.1
	540nm	22.2	21.4	24.9	25.9	26.4	25.0	27.6	26.4
	550nm	22.5	21.7	25.3	26.4	26.8	25.4	28.1	26.8
	560nm	22.9	22.0	25.7	26.7	27.1	25.7	28.5	27.1
	570nm	23.3	22.4	26.2	27.2	27.5	26.0	28.9	27.4
	580nm	23.6	22.7	26.5	27.5	27.8	26.3	29.2	27.8
	590nm	23.9	23.0	26.8	27.8	28.0	26.5	29.5	27.9
	600nm	24.3	23.3	27.2	28.1	28.4	26.8	29.8	28.2
	610nm	24.5	23.7	27.5	28.4	28.6	27.0	30.1	28.5
	620nm	24.8	23.9	27.8	28.7	28.8	27.2	30.3	28.6
	630nm	25.2	24.3	28.1	28.9	29.1	27.5	30.7	28.9
	640nm	25.3	24.4	28.3	29.1	29.3	27.5	30.8	29.0
	650nm	25.6	24.8	28.6	29.4	29.5	27.8	31.0	29.2
	660nm	25.9	25.1	28.8	29.5	29.7	27.9	31.3	29.3
	670nm	26.1	25.3	29.0	29.7	29.8	28.1	31.5	29.5
	680nm	26.4	25.6	29.3	30.0	30.0	28.3	31.8	29.7
	690nm	26.6	25.9	29.6	30.1	30.4	28.5	32.0	29.8
	700nm	26.9	26.2	29.7	30.3	30.2	28.6	32.1	30.0
	710nm	27.1	26.4	30.0	30.6	30.6	28.8	32.3	30.2
	720nm	27.3	26.6	30.2	30.6	30.8	29.0	32.6	30.3
	730nm	27.5	27.0	30.5	30.9	30.7	29.2	32.7	30.5
	740nm	27.8	27.2	30.7	31.1	31.1	29.3	33.0	30.6

Appendix 3: continued.

Well		Panuke B-90							
Depth (m)		2227.00	2227.55	2228.98	2229.62	2230	2234.99	2235.37	2235.68
Type of Sample[1]		B	B	B	B	D	B	A	B
Illuminant setting	**L*(D65)**	52.7	49.9	54.8	53.9	54.3	57.5	58.0	58.4
	a*(D65)	1.1	1.7	1.1	1.2	1.1	0.8	1.4	0.6
	b*(D65)	7.3	7.5	7.5	7.0	9.2	8.7	11.1	8.5
Relative intensity at 10 nm wavelength increments starting at specified wavelength	**360nm**	17.0	18.1	18.8	18.9	17.6	18.9	15.6	14.9
	370nm	18.1	19.3	20.2	20.3	18.7	20.1	16.8	15.9
	380nm	19.4	20.7	21.7	21.8	19.8	21.4	18.2	17.0
	390nm	20.5	21.8	23.0	22.9	20.8	22.4	19.5	17.9
	400nm	21.4	22.8	24.0	23.9	21.6	23.2	20.5	18.6
	410nm	22.2	23.6	24.9	24.8	22.2	24.0	21.4	19.3
	420nm	23.0	24.5	25.9	25.7	22.9	24.8	22.4	20.0
	430nm	23.8	25.2	26.7	26.5	23.5	25.4	23.3	20.7
	440nm	24.5	26.0	27.5	27.3	24.0	26.0	24.1	21.3
	450nm	25.2	26.7	28.2	28.0	24.5	26.6	25.0	21.9
	460nm	25.7	27.2	28.8	28.5	24.8	27.0	25.6	22.4
	470nm	26.3	27.8	29.4	29.1	25.2	27.4	26.4	23.0
	480nm	26.8	28.3	29.9	29.7	25.6	27.8	27.0	23.4
	490nm	27.3	28.7	30.5	30.2	25.9	28.2	27.6	23.9
	500nm	27.8	29.3	31.0	30.7	26.2	28.5	28.2	24.3
	510nm	28.3	29.7	31.5	31.2	26.4	28.9	28.7	24.7
	520nm	28.8	30.3	31.9	31.7	26.8	29.2	29.2	25.2
	530nm	29.1	30.6	32.3	32.0	27.0	29.4	29.8	25.6
	540nm	29.6	31.0	32.7	32.3	27.1	29.7	30.2	26.0
	550nm	30.0	31.3	32.9	32.7	27.3	29.9	30.5	26.5
	560nm	30.2	31.6	33.2	32.9	27.5	30.0	30.8	27.1
	570nm	30.5	32.0	33.5	33.2	27.6	30.2	31.1	27.8
	580nm	30.8	32.1	33.6	33.4	27.8	30.3	31.4	28.3
	590nm	30.9	32.3	33.7	33.4	27.8	30.4	31.4	28.6
	600nm	31.1	32.5	33.8	33.6	27.9	30.4	31.7	28.9
	610nm	31.3	32.6	34.0	33.8	28.0	30.5	31.8	29.2
	620nm	31.4	32.8	34.0	33.8	28.0	30.6	31.8	29.3
	630nm	31.7	33.0	34.2	34.0	28.2	30.7	32.0	29.4
	640nm	31.6	33.0	34.1	34.0	28.1	30.6	32.0	29.5
	650nm	31.9	33.1	34.3	34.1	28.3	30.8	32.1	29.6
	660nm	32.0	33.2	34.4	34.2	28.2	30.7	32.2	29.7
	670nm	32.0	33.2	34.3	34.2	28.3	30.6	32.2	29.8
	680nm	32.1	33.5	34.5	34.4	28.4	31.0	32.4	30.0
	690nm	32.3	33.5	34.5	34.6	28.4	30.8	32.5	30.1
	700nm	32.4	33.5	34.6	34.5	28.4	30.7	32.6	30.2
	710nm	32.6	33.8	34.7	34.7	28.5	31.1	32.7	30.3
	720nm	32.6	33.9	34.8	34.8	28.6	30.8	32.9	30.5
	730nm	32.8	34.0	35.0	34.9	28.7	31.2	33.1	30.7
	740nm	33.0	34.1	35.1	35.1	28.7	31.1	33.2	30.9

Appendix 3: continued.

Well		Panuke B-90							
Depth (m)		2236.14	2237.64	2238.19	2239.27	2239.67	2240	2240.33	2241.05
Type of Sample[1]		B	B	B	B	B	D	B	B
Illuminant setting	**L*(D65)**	58.8	57.5	60.0	58.8	61.5	56.1	62.7	64.0
	a*(D65)	0.4	0.4	0.6	0.1	-0.2	0.9	-0.3	-0.7
	b*(D65)	7.7	6.9	7.7	7.6	7.0	10.8	6.8	6.5
Relative intensity at 10 nm wavelength increments starting at specified wavelength	**360nm**	16.3	17.8	13.3	20.6	13.6	18.6	14.1	14.1
	370nm	17.4	19.1	14.2	21.9	14.5	19.9	15.4	14.9
	380nm	18.7	20.4	15.3	23.3	15.4	21.3	16.7	15.9
	390nm	19.8	21.5	16.3	24.5	16.0	22.4	17.8	16.7
	400nm	20.7	22.5	17.1	25.4	16.6	23.4	18.8	17.4
	410nm	21.5	23.4	17.8	26.2	17.2	24.3	19.7	18.1
	420nm	22.3	24.3	18.5	27.1	17.8	25.1	20.6	18.8
	430nm	23.0	25.0	19.2	27.8	18.3	25.9	21.3	19.4
	440nm	23.8	25.8	19.9	28.5	18.8	26.6	22.1	19.9
	450nm	24.4	26.5	20.4	29.2	19.4	27.2	22.8	20.4
	460nm	25.0	27.1	20.9	29.6	19.7	27.7	23.4	20.8
	470nm	25.4	27.6	21.6	30.2	20.0	28.2	24.1	21.2
	480nm	26.0	28.2	22.0	30.7	20.4	28.8	24.6	21.6
	490nm	26.5	28.7	22.5	31.2	20.8	29.2	25.2	22.1
	500nm	26.9	29.2	22.9	31.5	21.2	29.6	25.6	22.4
	510nm	27.3	29.7	23.4	31.9	21.5	30.1	26.2	22.8
	520nm	27.8	30.2	23.8	32.4	21.9	30.5	26.7	23.3
	530nm	28.1	30.4	24.2	32.7	22.2	30.9	27.1	23.6
	540nm	28.4	30.8	24.6	33.0	22.5	31.1	27.6	23.9
	550nm	28.8	31.1	25.1	33.2	22.8	31.4	27.9	24.3
	560nm	29.0	31.3	25.7	33.4	23.0	31.7	28.2	24.5
	570nm	29.2	31.6	26.2	33.7	23.3	31.9	28.6	24.9
	580nm	29.4	31.7	26.6	33.8	23.6	32.1	28.8	25.1
	590nm	29.4	31.7	26.9	34.0	23.7	32.2	29.0	25.3
	600nm	29.6	31.9	27.2	34.1	23.9	32.4	29.2	25.6
	610nm	29.7	32.0	27.4	34.3	24.1	32.6	29.4	25.7
	620nm	29.7	32.0	27.5	34.3	24.3	32.7	29.5	25.9
	630nm	29.9	32.1	27.7	34.5	24.6	32.9	29.8	26.1
	640nm	29.7	32.1	27.8	34.5	24.6	32.9	29.8	26.1
	650nm	29.9	32.1	28.0	34.6	24.8	33.1	30.0	26.4
	660nm	30.0	32.2	28.1	34.7	25.0	33.2	30.2	26.5
	670nm	30.0	32.2	28.1	34.7	25.0	33.2	30.3	26.7
	680nm	30.1	32.3	28.5	34.9	25.3	33.5	30.5	26.9
	690nm	30.1	32.4	28.6	35.0	25.5	33.6	30.7	27.0
	700nm	30.2	32.4	28.6	35.0	25.5	33.5	30.8	27.1
	710nm	30.3	32.5	28.9	35.2	25.7	33.9	31.1	27.4
	720nm	30.3	32.6	29.0	35.3	25.9	33.9	31.2	27.6
	730nm	30.5	32.8	29.2	35.5	26.0	34.1	31.6	27.9
	740nm	30.7	33.0	29.5	35.5	26.2	34.4	31.8	28.0

Appendix 3: continued.

Well		Panuke B-90							
Depth (m)		2241.57	2241.68	2242.40	2243.67	2244.04	2244.57	2245.47	2245.78
Type of Sample[1]		A	B	B	B	B	B	B	A
Illuminant setting	**L*(D65)**	64.8	63.8	59.2	61.4	62.0	58.8	60.4	61.6
	a*(D65)	-0.9	-0.6	-0.5	-0.7	-0.8	1.2	-0.7	-0.8
	b*(D65)	7.5	6.5	4.4	4.8	8.1	8.1	6.5	7.1
Relative intensity at 10 nm wavelength increments starting at specified wavelength	**360nm**	17.4	14.8	12.4	13.5	20.2	16.8	17.8	17.0
	370nm	18.4	15.7	13.2	14.3	21.5	17.9	19.0	18.2
	380nm	19.5	16.8	14.1	15.2	23.0	19.0	20.3	19.4
	390nm	20.3	17.6	14.7	15.9	24.3	19.9	21.4	20.5
	400nm	21.1	18.3	15.3	16.6	25.3	20.8	22.4	21.4
	410nm	21.8	19.0	15.9	17.1	26.2	21.5	23.3	22.4
	420nm	22.5	19.7	16.5	17.7	27.2	22.2	24.1	23.2
	430nm	23.1	20.3	17.0	18.3	28.0	22.9	24.9	24.0
	440nm	23.7	20.9	17.6	18.9	28.8	23.5	25.7	24.8
	450nm	24.3	21.5	18.0	19.4	29.6	24.1	26.4	25.5
	460nm	24.7	21.9	18.4	19.7	30.1	24.5	27.0	26.2
	470nm	25.1	22.4	18.8	20.1	30.8	25.0	27.5	26.8
	480nm	25.4	22.9	19.2	20.5	31.4	25.4	28.1	27.4
	490nm	25.9	23.3	19.6	20.8	31.9	25.8	28.6	28.0
	500nm	26.3	23.8	20.0	21.2	32.4	26.2	29.2	28.5
	510nm	26.7	24.1	20.4	21.6	32.9	26.6	29.6	29.1
	520nm	27.1	24.6	20.7	21.9	33.5	27.0	30.2	29.7
	530nm	27.4	24.9	21.1	22.2	33.9	27.3	30.6	30.2
	540nm	27.7	25.3	21.4	22.5	34.3	27.7	31.0	30.7
	550nm	28.1	25.6	21.7	22.8	34.6	28.0	31.4	31.1
	560nm	28.3	25.9	21.9	23.0	34.9	28.3	31.9	31.6
	570nm	28.7	26.2	22.2	23.3	35.3	28.6	32.4	32.1
	580nm	28.9	26.5	22.5	23.6	35.5	28.9	32.8	32.4
	590nm	29.1	26.7	22.6	23.7	35.6	29.1	33.0	32.7
	600nm	29.4	27.0	22.9	23.9	35.9	29.4	33.3	33.0
	610nm	29.6	27.2	23.2	24.1	36.0	29.6	33.6	33.3
	620nm	29.7	27.3	23.3	24.2	36.0	29.7	33.7	33.4
	630nm	30.0	27.6	23.6	24.4	36.2	29.9	33.9	33.7
	640nm	30.1	27.7	23.6	24.6	36.2	29.9	33.9	33.7
	650nm	30.3	28.0	23.9	24.7	36.3	30.1	34.0	33.9
	660nm	30.5	28.1	24.0	24.8	36.3	30.2	34.1	34.0
	670nm	30.6	28.3	24.2	24.9	36.4	30.2	34.1	34.1
	680nm	30.8	28.4	24.5	25.2	36.6	30.4	34.3	34.4
	690nm	31.0	28.7	24.5	25.3	36.7	30.5	34.3	34.5
	700nm	31.1	28.9	24.7	25.4	36.7	30.7	34.5	34.5
	710nm	31.3	29.0	25.0	25.6	36.9	30.8	34.7	34.9
	720nm	31.4	29.2	25.0	25.7	37.0	30.9	34.9	34.9
	730nm	31.6	29.5	25.4	25.8	37.3	31.0	35.0	35.3
	740nm	31.7	29.7	25.5	25.9	37.5	31.2	35.2	35.5

Appendix 3: continued.

Well		Panuke B-90							
Depth (m)		2246.22	2247.13	2247.20	2248.10	2248.67	2249.69	2250.64	2251.48
Type of Sample[1]		B	B	A	B	B	B	B	B
Illuminant setting	L*(D65)	62.4	57.4	59.1	64.3	54.9	62.8	59.7	56.4
	a*(D65)	-0.8	0.9	2.1	-0.5	0.3	-0.4	-0.2	0.3
	b*(D65)	6.5	8.4	8.5	5.6	6.4	6.0	8.0	6.7
Relative intensity at 10 nm wavelength increments starting at specified wavelength	360nm	21.1	18.5	17.4	19.7	19.5	17.9	18.7	18.2
	370nm	22.5	19.5	18.4	21.1	20.9	19.3	19.9	19.5
	380nm	24.1	20.7	19.6	22.5	22.4	20.7	21.3	20.9
	390nm	25.4	21.8	20.5	23.7	23.6	22.0	22.3	22.1
	400nm	26.5	22.6	21.3	24.8	24.6	23.0	23.3	23.1
	410nm	27.5	23.4	22.1	25.7	25.6	24.0	24.2	24.0
	420nm	28.4	24.2	22.9	26.6	26.5	25.0	25.0	25.0
	430nm	29.3	24.9	23.6	27.5	27.3	25.8	25.8	25.9
	440nm	30.1	25.6	24.2	28.4	28.1	26.7	26.5	26.8
	450nm	30.8	26.3	24.9	29.2	28.9	27.4	27.3	27.6
	460nm	31.4	26.7	25.3	29.8	29.4	28.1	27.8	28.2
	470nm	32.1	27.3	25.9	30.5	29.9	28.7	28.4	28.8
	480nm	32.7	27.8	26.3	31.2	30.4	29.4	28.9	29.6
	490nm	33.2	28.3	26.9	31.7	31.0	30.0	29.4	30.1
	500nm	33.7	28.8	27.3	32.3	31.4	30.5	29.9	30.7
	510nm	34.2	29.2	27.7	32.8	31.9	31.1	30.4	31.2
	520nm	34.7	29.7	28.2	33.5	32.4	31.6	30.9	31.8
	530nm	35.0	30.1	28.6	33.9	32.7	32.0	31.2	32.2
	540nm	35.3	30.5	29.0	34.4	33.0	32.4	31.5	32.6
	550nm	35.6	30.9	29.5	34.9	33.4	32.8	31.9	33.0
	560nm	35.8	31.4	30.0	35.2	33.6	33.1	32.2	33.4
	570nm	36.1	32.0	30.6	35.6	33.9	33.4	32.5	33.7
	580nm	36.3	32.5	31.0	35.9	34.1	33.6	32.7	34.0
	590nm	36.3	32.8	31.3	36.1	34.3	33.8	32.8	34.1
	600nm	36.5	33.2	31.7	36.3	34.4	34.0	33.0	34.3
	610nm	36.6	33.4	31.9	36.5	34.6	34.1	33.2	34.4
	620nm	36.6	33.5	32.0	36.6	34.7	34.2	33.2	34.5
	630nm	36.8	33.7	32.3	36.8	34.8	34.4	33.5	34.7
	640nm	36.7	33.8	32.3	36.8	34.8	34.4	33.4	34.6
	650nm	36.8	33.8	32.5	36.9	35.0	34.5	33.5	34.8
	660nm	36.9	34.0	32.6	37.0	34.9	34.5	33.6	34.8
	670nm	36.9	33.9	32.6	37.1	34.9	34.6	33.7	34.8
	680nm	37.1	34.1	32.8	37.2	35.2	34.8	33.7	35.0
	690nm	37.1	34.3	33.1	37.3	35.2	34.9	33.8	35.1
	700nm	37.1	34.4	33.0	37.3	35.3	34.9	33.9	35.1
	710nm	37.3	34.5	33.3	37.5	35.4	35.1	34.0	35.2
	720nm	37.4	34.8	33.5	37.7	35.5	35.2	34.2	35.4
	730nm	37.6	34.9	33.6	37.9	35.6	35.5	34.4	35.6
	740nm	37.8	35.2	33.9	38.1	35.8	35.7	34.4	35.8

Appendix 3: continued.

Well		Panuke B-90							
Depth (m)		2251.88	2252.90	2253.73	2254.10	2255	2255.05	2255.49	2255.57
Type of Sample[1]		B	B	B	B	D	B	A	B
Illuminant setting	**L*(D65)**	60.0	57.7	53.7	54.9	57.4	65.4	62.6	59.9
	a*(D65)	0.3	0.3	0.4	0.2	0.6	-0.5	0.1	0.3
	b*(D65)	6.1	7.0	6.9	6.3	9.8	6.8	7.8	6.3
Relative intensity at 10 nm wavelength increments starting at specified wavelength	**360nm**	19.1	19.7	17.9	15.9	20.2	20.4	20.2	20.5
	370nm	20.5	21.1	19.1	17.0	21.7	21.8	21.6	22.0
	380nm	21.9	22.6	20.4	18.2	23.2	23.3	23.2	23.5
	390nm	23.2	23.8	21.7	19.3	24.5	24.5	24.5	24.9
	400nm	24.2	24.9	22.7	20.3	25.6	25.5	25.6	26.0
	410nm	25.2	25.9	23.6	21.1	26.6	26.4	26.6	27.0
	420nm	26.1	26.8	24.5	22.0	27.6	27.2	27.5	27.9
	430nm	27.0	27.7	25.3	22.8	28.4	28.1	28.4	28.7
	440nm	27.8	28.6	26.1	23.5	29.3	28.7	29.3	29.6
	450nm	28.5	29.3	26.8	24.2	30.1	29.4	30.1	30.3
	460nm	29.2	30.0	27.4	24.7	30.7	30.0	30.7	30.9
	470nm	29.8	30.6	28.1	25.3	31.3	30.5	31.3	31.5
	480nm	30.4	31.2	28.7	25.9	32.0	31.0	32.0	32.1
	490nm	31.0	31.8	29.2	26.4	32.6	31.5	32.6	32.6
	500nm	31.5	32.3	29.7	26.9	33.1	31.9	33.1	33.2
	510nm	32.0	32.9	30.2	27.3	33.6	32.4	33.7	33.6
	520nm	32.6	33.4	30.7	27.8	34.2	32.8	34.3	34.2
	530nm	33.0	33.8	30.9	28.1	34.6	33.2	34.7	34.6
	540nm	33.4	34.1	31.2	28.4	35.0	33.5	35.2	34.9
	550nm	33.7	34.5	31.5	28.7	35.4	33.8	35.6	35.3
	560nm	34.0	34.8	31.7	28.9	35.7	34.1	35.9	35.6
	570nm	34.4	35.1	32.0	29.1	36.0	34.4	36.3	36.0
	580nm	34.6	35.3	32.1	29.2	36.3	34.6	36.5	36.2
	590nm	34.6	35.4	32.1	29.3	36.4	34.8	36.7	36.3
	600nm	34.8	35.6	32.3	29.4	36.6	35.0	37.0	36.6
	610nm	35.0	35.7	32.3	29.5	36.8	35.1	37.2	36.8
	620nm	35.0	35.7	32.3	29.5	36.9	35.2	37.4	36.8
	630nm	35.2	35.9	32.4	29.7	37.2	35.4	37.6	37.1
	640nm	35.1	35.8	32.2	29.6	37.2	35.4	37.7	37.2
	650nm	35.2	35.9	32.3	29.7	37.4	35.5	37.8	37.4
	660nm	35.2	36.0	32.3	29.9	37.4	35.7	37.9	37.5
	670nm	35.3	35.9	32.4	29.8	37.5	35.7	38.1	37.5
	680nm	35.4	36.1	32.3	29.9	37.6	35.9	38.2	37.8
	690nm	35.5	36.1	32.4	30.0	37.8	36.0	38.3	37.9
	700nm	35.5	36.3	32.6	30.2	37.8	36.0	38.4	38.0
	710nm	35.6	36.4	32.6	30.2	38.1	36.3	38.7	38.1
	720nm	35.8	36.4	32.7	30.3	38.1	36.3	38.8	38.4
	730nm	36.0	36.7	32.9	30.6	38.4	36.6	39.0	38.6
	740nm	36.2	36.9	32.9	30.7	38.6	36.6	39.2	38.7

Appendix 3: continued.

Well		Panuke B-90							
Depth (m)		2256.43	2256.56	2256.91	2258.03	2258.78	2259.02	2260.00	2260
Type of Sample[1]		B	A	B	B	B	B	B	D
Illuminant setting	**L*(D65)**	63.0	62.7	62.7	66.1	62.6	61.4	65.6	51.9
	a*(D65)	0.3	0.4	0.3	-0.8	0.8	0.9	-0.3	0.4
	b*(D65)	7.5	8.0	8.4	6.1	7.3	7.4	7.7	8.7
Relative intensity at 10 nm wavelength increments starting at specified wavelength	**360nm**	19.9	17.2	20.5	20.8	19.6	16.8	11.9	11.8
	370nm	21.4	18.5	21.7	22.3	20.9	18.0	12.6	12.4
	380nm	22.9	19.9	23.1	23.9	22.4	19.2	13.3	13.1
	390nm	24.1	21.0	24.3	25.2	23.5	20.4	13.9	13.6
	400nm	25.2	22.1	25.4	26.3	24.5	21.3	14.3	14.1
	410nm	26.2	22.9	26.3	27.3	25.3	22.2	14.8	14.5
	420nm	27.1	23.9	27.1	28.3	26.2	23.1	15.2	14.9
	430nm	27.8	24.7	28.0	29.0	26.8	23.8	15.6	15.4
	440nm	28.6	25.5	28.8	29.8	27.5	24.6	16.0	15.8
	450nm	29.2	26.2	29.4	30.6	28.0	25.2	16.4	16.2
	460nm	29.7	26.9	30.0	31.1	28.5	25.8	16.7	16.4
	470nm	30.2	27.4	30.6	31.7	29.0	26.4	17.0	16.7
	480nm	30.7	28.0	31.2	32.3	29.4	27.0	17.3	17.0
	490nm	31.2	28.5	31.7	32.8	29.8	27.5	17.7	17.4
	500nm	31.6	29.0	32.2	33.3	30.2	27.9	18.0	17.6
	510nm	32.1	29.6	32.6	33.8	30.5	28.4	18.3	17.9
	520nm	32.5	30.1	33.1	34.3	31.0	29.0	18.6	18.3
	530nm	32.8	30.5	33.5	34.6	31.2	29.3	18.9	18.5
	540nm	33.1	30.9	33.9	34.9	31.5	29.7	19.2	18.8
	550nm	33.4	31.2	34.2	35.3	31.8	30.1	19.5	19.1
	560nm	33.6	31.5	34.6	35.6	32.0	30.4	19.7	19.4
	570nm	33.9	31.9	34.9	35.9	32.3	30.7	20.0	19.7
	580nm	34.0	32.1	35.1	36.1	32.4	31.0	20.3	19.9
	590nm	34.1	32.2	35.2	36.2	32.6	31.2	20.5	20.1
	600nm	34.4	32.5	35.5	36.5	32.8	31.5	20.8	20.4
	610nm	34.6	32.7	35.7	36.7	32.9	31.7	21.0	20.7
	620nm	34.6	32.8	35.8	36.8	33.0	31.8	21.2	20.9
	630nm	34.9	33.1	36.0	37.1	33.3	32.0	21.5	21.2
	640nm	34.8	33.0	36.0	37.1	33.3	32.0	21.6	21.3
	650nm	35.0	33.2	36.2	37.2	33.5	32.2	21.9	21.5
	660nm	35.1	33.3	36.3	37.4	33.6	32.3	22.0	21.7
	670nm	35.2	33.4	36.4	37.5	33.6	32.4	22.2	22.0
	680nm	35.3	33.6	36.6	37.7	33.9	32.6	22.5	22.3
	690nm	35.5	33.6	36.7	37.8	33.9	32.7	22.7	22.3
	700nm	35.6	33.8	36.8	38.0	34.1	32.9	22.9	22.6
	710nm	35.8	34.0	37.0	38.2	34.2	33.1	23.1	22.8
	720nm	35.9	34.1	37.0	38.3	34.3	33.2	23.3	22.9
	730nm	36.1	34.4	37.3	38.6	34.6	33.5	23.5	23.3
	740nm	36.3	34.6	37.6	38.8	34.7	33.7	23.8	23.3

Appendix 3: continued.

Well		Panuke B-90							
Depth (m)		2260.56	2261.76	2262.52	2263.21	2263.84	2263.94	2264.48	2265.35
Type of Sample[1]		B	B	B	B	B	A	B	B
Illuminant setting	**L*(D65)**	64.4	63.9	63.2	64.1	64.6	63.6	65.3	62.8
	a*(D65)	-0.4	-0.6	-0.4	-0.6	-0.6	-0.6	-0.7	-1.1
	b*(D65)	6.3	7.4	6.6	7.6	7.0	7.7	6.9	6.5
Relative intensity at 10 nm wavelength increments starting at specified wavelength	**360nm**	13.4	13.2	14.7	11.9	13.0	8.8	4.5	10.1
	370nm	14.2	14.0	15.6	12.7	13.7	9.4	4.8	10.6
	380nm	15.2	14.9	16.5	13.5	14.4	10.0	5.1	11.3
	390nm	15.9	15.5	17.1	14.0	15.0	10.5	5.3	11.9
	400nm	16.6	16.0	17.8	14.6	15.5	11.0	5.5	12.5
	410nm	17.2	16.6	18.3	15.1	16.0	11.5	5.8	13.0
	420nm	17.7	17.1	18.8	15.6	16.5	12.0	6.0	13.6
	430nm	18.2	17.6	19.3	16.1	16.9	12.5	6.2	14.1
	440nm	18.8	18.1	19.8	16.5	17.3	13.0	6.5	14.7
	450nm	19.3	18.6	20.3	16.9	17.7	13.4	6.7	15.2
	460nm	19.6	18.9	20.6	17.2	18.0	13.8	6.9	15.6
	470nm	20.1	19.3	20.9	17.6	18.3	14.2	7.1	16.1
	480nm	20.4	19.7	21.3	17.9	18.7	14.5	7.3	16.5
	490nm	20.8	20.0	21.6	18.3	19.0	14.9	7.5	16.9
	500nm	21.2	20.4	21.9	18.6	19.3	15.3	7.7	17.3
	510nm	21.6	20.7	22.2	18.9	19.6	15.7	8.0	17.8
	520nm	22.0	21.2	22.7	19.2	19.9	16.2	8.2	18.3
	530nm	22.3	21.5	22.9	19.5	20.2	16.5	8.5	18.7
	540nm	22.7	21.8	23.2	19.8	20.4	16.9	8.7	19.2
	550nm	23.0	22.2	23.5	20.1	20.7	17.4	8.9	19.6
	560nm	23.4	22.5	23.8	20.3	21.0	17.7	9.1	19.9
	570nm	23.7	22.8	24.1	20.6	21.3	18.1	9.3	20.4
	580nm	24.0	23.1	24.3	20.9	21.5	18.4	9.6	20.7
	590nm	24.2	23.4	24.5	21.1	21.7	18.7	9.7	21.0
	600nm	24.6	23.8	24.8	21.4	22.0	19.1	9.9	21.4
	610nm	24.9	24.0	25.0	21.6	22.2	19.4	10.2	21.7
	620nm	25.1	24.2	25.2	21.8	22.5	19.6	10.3	21.9
	630nm	25.4	24.5	25.4	22.1	22.8	20.0	10.6	22.3
	640nm	25.5	24.7	25.5	22.2	22.8	20.2	10.7	22.5
	650nm	25.7	25.0	25.8	22.5	23.1	20.4	10.9	22.7
	660nm	26.0	25.2	26.0	22.7	23.3	20.7	11.1	23.0
	670nm	26.2	25.4	26.2	23.0	23.5	21.0	11.3	23.2
	680nm	26.4	25.6	26.4	23.2	23.7	21.2	11.4	23.5
	690nm	26.6	25.8	26.4	23.3	23.9	21.4	11.5	23.7
	700nm	26.8	26.0	26.6	23.6	24.1	21.7	11.8	23.9
	710nm	27.0	26.2	26.9	23.9	24.3	22.0	12.0	24.2
	720nm	27.2	26.4	27.0	24.0	24.4	22.1	12.0	24.4
	730nm	27.6	26.6	27.1	24.3	24.7	22.5	12.3	24.5
	740nm	27.7	26.8	27.3	24.5	24.9	22.7	12.4	24.8

Appendix 3: continued.

Well		Panuke B-90							
Depth (m)		2265.95	2268.58	2270.05	2270.74	2271.69	2273.09	2274.42	2275.06
Type of Sample[1]		B	B	B	B	B	B	B	B
Illuminant setting	**L*(D65)**	60.3	66.0	64.8	66.1	66.0	64.4	62.6	65.1
	a*(D65)	-0.9	-0.4	-0.3	-0.2	-0.3	-0.4	-0.3	-0.3
	b*(D65)	6.7	7.0	6.0	7.3	6.7	5.8	7.3	6.5
Relative intensity at 10 nm wavelength increments starting at specified wavelength	**360nm**	10.9	9.9	4.1	9.7	7.5	8.7	9.9	7.7
	370nm	11.5	10.6	4.5	10.4	8.0	9.3	10.5	8.2
	380nm	12.3	11.3	4.8	11.1	8.5	10.0	11.2	8.7
	390nm	12.8	11.8	5.0	11.6	9.0	10.4	11.6	9.1
	400nm	13.2	12.4	5.2	12.2	9.5	10.9	12.1	9.4
	410nm	13.8	12.9	5.5	12.7	10.0	11.5	12.5	9.8
	420nm	14.3	13.4	5.8	13.3	10.5	12.0	13.0	10.2
	430nm	14.9	14.0	6.0	13.9	11.0	12.5	13.4	10.5
	440nm	15.4	14.5	6.4	14.4	11.5	13.0	13.9	10.9
	450nm	15.9	15.0	6.6	15.0	12.0	13.5	14.3	11.2
	460nm	16.2	15.5	6.8	15.4	12.4	13.9	14.6	11.5
	470nm	16.6	15.8	7.1	15.9	12.8	14.3	15.0	11.8
	480nm	17.0	16.2	7.3	16.3	13.2	14.7	15.3	12.1
	490nm	17.4	16.7	7.5	16.8	13.6	15.0	15.7	12.3
	500nm	17.9	17.1	7.8	17.3	14.1	15.4	16.0	12.6
	510nm	18.3	17.5	8.1	17.8	14.6	15.9	16.4	12.9
	520nm	18.8	17.9	8.5	18.3	15.2	16.4	16.9	13.3
	530nm	19.2	18.3	8.8	18.8	15.7	16.8	17.2	13.5
	540nm	19.5	18.7	9.0	19.4	16.2	17.2	17.5	13.8
	550nm	20.0	19.1	9.4	19.9	16.7	17.7	17.9	14.2
	560nm	20.3	19.4	9.7	20.4	17.2	18.1	18.2	14.4
	570nm	20.8	19.8	10.0	21.0	17.7	18.5	18.6	14.7
	580nm	21.1	20.1	10.2	21.5	18.1	18.9	18.9	15.0
	590nm	21.4	20.4	10.5	21.9	18.5	19.2	19.1	15.2
	600nm	21.8	20.7	10.8	22.4	19.0	19.5	19.5	15.5
	610nm	22.1	21.0	11.0	22.8	19.3	19.8	19.7	15.7
	620nm	22.4	21.2	11.3	23.1	19.6	20.1	19.9	16.0
	630nm	22.7	21.5	11.6	23.5	20.0	20.4	20.2	16.3
	640nm	23.0	21.6	11.7	23.7	20.3	20.5	20.4	16.4
	650nm	23.2	21.9	12.0	24.0	20.6	20.8	20.6	16.6
	660nm	23.5	22.1	12.2	24.4	21.0	21.0	20.9	16.9
	670nm	23.8	22.3	12.4	24.6	21.2	21.2	21.1	17.1
	680nm	24.1	22.6	12.5	24.9	21.5	21.5	21.4	17.3
	690nm	24.4	22.8	12.8	25.2	21.8	21.8	21.5	17.5
	700nm	24.5	22.9	13.1	25.5	22.2	21.9	21.7	17.7
	710nm	24.9	23.1	13.1	25.7	22.3	22.1	21.9	18.0
	720nm	25.0	23.2	13.5	26.1	22.6	22.3	22.1	18.1
	730nm	25.3	23.6	13.7	26.2	23.0	22.5	22.4	18.3
	740nm	25.5	23.7	13.8	26.5	23.1	22.7	22.5	18.6

Appendix 3: continued.

Well		Panuke B-90							
Depth (m)		2276.64	2276.96	2278.21	2278.26	2281.10	2283.68	2284.44	2284.58
Type of Sample[1]		B	B	A	B	B	B	B	B
Illuminant setting	**L*(D65)**	65.9	63.1	65.1	61.7	51.4	51.0	55.2	54.3
	a*(D65)	-0.3	-0.2	-0.4	-0.1	0.9	1.0	0.9	1.0
	b*(D65)	6.3	5.4	6.9	7.2	6.4	6.3	7.0	7.0
Relative intensity at 10 nm wavelength increments starting at specified wavelength	**360nm**	8.4	10.2	9.2	8.7	10.8	8.7	8.3	8.1
	370nm	8.9	10.8	9.8	9.3	11.4	9.2	8.8	8.6
	380nm	9.4	11.4	10.4	9.9	12.1	9.7	9.3	9.1
	390nm	9.8	11.9	10.8	10.3	12.5	10.1	9.6	9.5
	400nm	10.1	12.3	11.2	10.7	13.0	10.4	10.0	9.9
	410nm	10.5	12.7	11.7	11.1	13.4	10.8	10.3	10.2
	420nm	10.9	13.2	12.0	11.5	13.8	11.1	10.7	10.6
	430nm	11.2	13.6	12.4	11.9	14.3	11.4	11.0	10.9
	440nm	11.6	14.0	12.8	12.3	14.7	11.8	11.3	11.3
	450nm	12.0	14.4	13.1	12.6	15.1	12.1	11.6	11.6
	460nm	12.2	14.7	13.5	13.0	15.4	12.4	11.8	11.8
	470nm	12.5	15.0	13.8	13.3	15.7	12.7	12.1	12.0
	480nm	12.9	15.4	14.0	13.6	16.1	13.0	12.4	12.3
	490nm	13.2	15.7	14.4	13.9	16.4	13.2	12.7	12.6
	500nm	13.5	16.0	14.7	14.2	16.8	13.5	12.9	12.9
	510nm	13.8	16.4	15.0	14.5	17.0	13.8	13.2	13.1
	520nm	14.2	16.8	15.3	15.0	17.5	14.2	13.5	13.5
	530nm	14.5	17.1	15.6	15.3	17.8	14.5	13.8	13.7
	540nm	14.8	17.4	15.9	15.5	18.1	14.7	14.0	14.0
	550nm	15.1	17.8	16.2	15.9	18.4	15.0	14.3	14.2
	560nm	15.4	18.0	16.5	16.2	18.7	15.3	14.5	14.4
	570nm	15.7	18.4	16.8	16.5	19.1	15.6	14.8	14.7
	580nm	16.0	18.7	17.1	16.8	19.4	15.9	15.0	15.0
	590nm	16.2	18.9	17.2	17.0	19.6	16.1	15.2	15.2
	600nm	16.5	19.2	17.5	17.3	19.9	16.4	15.5	15.4
	610nm	16.8	19.4	17.8	17.6	20.2	16.7	15.7	15.6
	620nm	17.0	19.6	18.0	17.8	20.4	16.9	15.9	15.8
	630nm	17.3	19.9	18.2	18.2	20.7	17.2	16.1	16.1
	640nm	17.4	20.1	18.4	18.3	20.9	17.4	16.3	16.1
	650nm	17.8	20.3	18.6	18.5	21.3	17.6	16.5	16.4
	660nm	18.0	20.5	18.8	18.8	21.4	17.9	16.7	16.6
	670nm	18.2	20.7	19.0	19.1	21.6	18.1	16.9	16.8
	680nm	18.5	21.0	19.3	19.4	21.9	18.3	17.2	17.1
	690nm	18.6	21.2	19.3	19.5	22.2	18.6	17.3	17.2
	700nm	18.9	21.4	19.6	19.7	22.2	18.8	17.5	17.5
	710nm	19.1	21.5	19.8	20.0	22.5	19.1	17.8	17.7
	720nm	19.3	21.7	19.9	20.2	22.7	19.1	17.9	17.8
	730nm	19.6	22.0	20.2	20.5	23.0	19.5	18.1	18.1
	740nm	19.8	22.1	20.4	20.7	23.2	19.7	18.4	18.1

Appendix 3: continued.

Well		Panuke B-90							
Depth (m)		2285.85	2287.88	2288.19	2319.18	2347.50	2402.33	2417.48	2436.35
Type of Sample[1]		B	B	B	A	A	A	A	A
Illuminant setting	**L*(D65)**	55.7	52.1	52.8	52.2	53.1	53.1	50.4	52.9
	a*(D65)	0.6	0.8	0.8	0.7	1.0	1.2	1.5	7.3
	b*(D65)	5.9	6.5	6.1	6.7	6.3	5.9	8.0	13.7
Relative intensity at 10 nm wavelength increments starting at specified wavelength	**360nm**	8.2	7.9	9.5	10.5	11.4	10.9	12.1	10.1
	370nm	8.7	8.3	10.0	11.2	12.3	11.8	13.1	10.8
	380nm	9.2	8.9	10.6	11.9	13.1	12.8	14.1	11.7
	390nm	9.6	9.2	11.1	12.5	13.7	13.6	15.0	12.3
	400nm	9.9	9.6	11.5	13.0	14.4	14.3	15.8	12.9
	410nm	10.3	9.9	11.9	13.5	15.0	15.0	16.6	13.5
	420nm	10.6	10.3	12.3	14.0	15.6	15.9	17.4	14.1
	430nm	10.9	10.6	12.6	14.6	16.2	16.6	18.2	14.7
	440nm	11.3	10.9	13.0	15.0	16.9	17.4	18.9	15.3
	450nm	11.6	11.2	13.4	15.5	17.4	18.1	19.6	15.8
	460nm	11.8	11.5	13.6	15.9	17.9	18.6	20.2	16.2
	470nm	12.1	11.8	14.0	16.3	18.3	19.3	20.9	16.7
	480nm	12.4	12.0	14.2	16.6	18.8	19.9	21.4	17.2
	490nm	12.7	12.3	14.5	17.0	19.3	20.4	21.9	17.6
	500nm	12.9	12.6	14.8	17.4	19.8	21.0	22.6	18.0
	510nm	13.2	12.8	15.2	17.8	20.3	21.7	23.2	18.5
	520nm	13.5	13.1	15.5	18.2	20.8	22.3	23.8	19.0
	530nm	13.8	13.4	15.7	18.6	21.3	22.9	24.3	19.3
	540nm	14.0	13.7	16.0	18.8	21.7	23.4	24.7	19.7
	550nm	14.3	13.9	16.3	19.3	22.1	23.9	25.3	20.1
	560nm	14.5	14.2	16.6	19.6	22.5	24.4	25.7	20.4
	570nm	14.8	14.4	16.8	19.9	23.0	24.9	26.1	20.8
	580nm	15.0	14.7	17.1	20.2	23.3	25.4	26.5	21.0
	590nm	15.2	14.9	17.3	20.4	23.6	25.7	26.8	21.2
	600nm	15.5	15.1	17.6	20.8	24.0	26.1	27.2	21.5
	610nm	15.7	15.3	17.8	21.0	24.4	26.4	27.5	21.7
	620nm	15.9	15.6	18.0	21.3	24.7	26.7	27.7	21.9
	630nm	16.2	15.9	18.3	21.6	25.1	27.1	28.1	22.1
	640nm	16.3	16.0	18.4	21.7	25.2	27.3	28.2	22.2
	650nm	16.5	16.2	18.7	22.0	25.6	27.6	28.4	22.4
	660nm	16.7	16.5	18.8	22.2	25.8	27.9	28.7	22.6
	670nm	16.9	16.6	19.1	22.3	26.0	28.1	28.8	22.6
	680nm	17.2	16.9	19.2	22.7	26.4	28.5	29.1	22.8
	690nm	17.3	17.1	19.5	22.9	26.7	28.6	29.3	23.0
	700nm	17.5	17.3	19.7	23.1	26.9	28.9	29.5	23.1
	710nm	17.8	17.5	19.9	23.4	27.2	29.2	29.8	23.3
	720nm	17.9	17.7	20.0	23.5	27.4	29.3	29.9	23.5
	730nm	18.1	17.8	20.3	23.8	27.6	29.6	30.1	23.7
	740nm	18.4	18.1	20.4	24.0	27.9	29.9	30.3	23.9

Appendix 4: Comparison between in-situ core and nearby powdered rubble samples (Sample type B) from Panuke B-90 well.

In-situ core samples					Powdered samples				
Depth (m)	Illuminant setting			Visual colour	Depth (m)	Illuminant setting			Visual colour
	L*(D65)	a*(D65)	b*(D65)			L*(D65)	a*(D65)	b*(D65)	
2215.14	39.21	-0.22	3.34	black	2215.15	49.51	0.84	5.51	dark brown
2215.61	38.62	0.07	4.69	black	2215.59	49.08	0.88	7.09	brown
2216.18	38.15	-0.17	4.34	black	2216.17	49.80	0.74	5.77	dark brown
2217.81	34.32	-0.1	3.85	black	2217.78	50.02	0.72	5.88	dark brown
2218.09	39.15	0	3.26	black	2218.08	49.86	0.86	5.89	dark brown
2219.37	28.38	0.4	2.88	dark grey	2219.36	47.42	1.21	7.27	dark brown
2220.22	35.84	0.29	4.77	dark grey	2220.22	47.17	1.05	6.88	dark brown
2220.65	40.11	0.22	4.6	black	2220.64	47.53	0.94	5.99	dark brown
2221.42	42.33	0.08	4.1	black	2221.41	53.39	0.57	5.94	dark brown
2222.59	34.87	0.78	5.17	black	2222.60	51.98	0.87	6.8	dark brown
2223.09	42.34	0.46	5.41	dark grey	2223.14	58.21	0.75	7.71	grey
2225.53	44.69	1.02	7.37	dark grey	2225.62	52.99	1.41	7.37	greyish brown
2226.54	38.56	1.04	5.82	dark grey	2226.53	49.26	0.65	5.45	dark brown
2227.03	43.74	1.06	6.04	grey	2227.00	52.70	1.1	7.34	greyish brown
2227.56	41.55	0.87	5.37	dark grey	2227.55	49.89	1.73	7.52	greyish brown
2228.96	45.15	0.93	6.6	greenish grey	2228.98	54.78	1.05	7.45	greyish brown
2229.61	47.41	0.5	6.45	dark grey	2229.62	53.92	1.2	6.95	greyish brown
2235.76	39.2	0.59	8.17	grey	2235.68	58.42	0.62	8.46	greyish brown
2236.09	41.21	0.07	6.16	dark grey	2236.14	58.81	0.42	7.69	greyish brown
2237.51	41.75	0.14	6.68	black	2237.64	57.48	0.37	6.86	greyish brown
2239.75	46.37	0.16	8.21	grey	2239.67	61.50	-0.23	7.04	greyish brown
2240.4	42.46	-0.85	5.73	greenish grey	2240.33	62.72	-0.34	6.75	grey
2242.3	51.93	-1.03	7.62	greenish grey	2242.40	59.19	-0.45	4.39	grey
2243.67	49.42	-1.51	5.75	green	2243.67	61.44	-0.66	4.82	grey
2245.53	45.77	-0.81	5.66	greenish grey	2245.47	60.42	-0.73	6.48	light grey
2246.24	46.03	-1.58	6.29	green	2246.22	62.43	-0.84	6.46	grey
2248.1	51.04	-1.02	5.2	green	2248.10	64.28	-0.52	5.6	light grey
2249.66	43.8	-0.72	3.82	greenish grey	2249.69	62.79	-0.38	6.01	grey
2250.65	38.73	-0.54	3.57	greenish grey	2250.64	59.73	-0.16	7.95	grey
2252.99	40.89	-0.52	4.89	greenish grey	2252.90	57.69	0.27	6.96	light greyish brown
2253.78	37.39	-0.27	3.92	dark grey	2253.73	53.72	0.37	6.94	light brown
2254.14	39.8	-0.07	3.86	black	2254.10	54.87	0.19	6.32	light brown
2255.69	43.03	-0.69	4.28	red	2255.57	59.91	0.26	6.25	light greyish brown
2256.36	42.69	0.11	4.48	greenish grey	2256.43	62.96	0.31	7.54	grey
2256.93	42.65	0.05	5.26	grey	2256.91	62.67	0.25	8.35	grey
2258.07	47.8	-1.48	3.83	greenish grey	2258.03	66.10	-0.8	6.12	light grey
2259.01	38.11	0.82	4.59	red	2259.02	61.39	0.91	7.41	grey
2260.14	39.23	0.73	5.01	greenish grey	2260.00	65.55	-0.28	7.66	light grey